Studies of Laser Guiding and Electron Injection in a High Power Laser Wakefield Accelerator

by

Christopher S. McGuffey

A dissertation submitted in partial fulfillment
of the requirements for the degree of
Doctor of Philosophy
(Nuclear Engineering and Radiological Sciences)
in The University of Michigan
2011

Doctoral Committee:

Professor Karl M. Krushelnick, Co-Chair
Assistant Professor Alexander G. R. Thomas, Co-Chair
Professor Roy Clarke
Professor Ronald M. Gilgenbach
Research Scientist Anatoly M. Maksimchuk

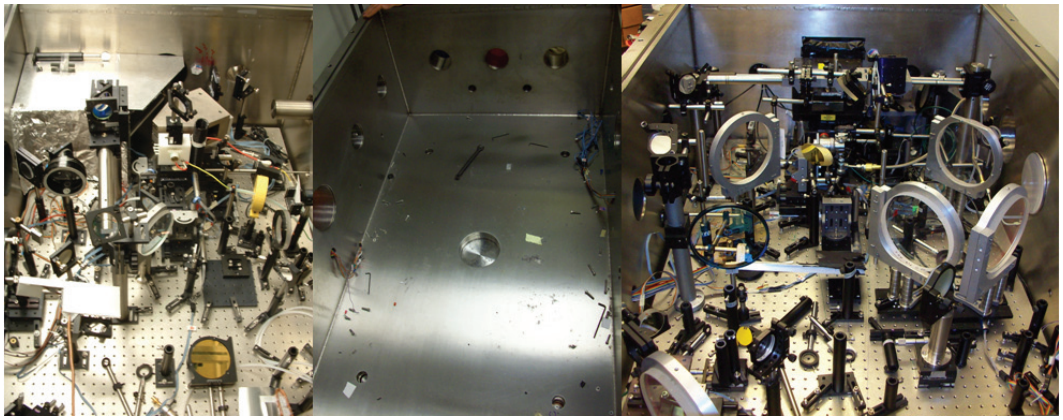

For my mother and father, who taught me to ask questions and find answers.

ACKNOWLEDGEMENTS

I would like to thank my advisor, Professor Karl Krushelnick, for his encouragement, foresight, and positive attitude. Thank you, also Karl, for teaching interesting courses, providing educational resources outside the classroom, and for granting so many opportunities to present within the scientific community. I could not have completed my thesis research without the daily guidance and clever ideas of Dr. Anatoly Maksimchuk. Thank you, Professor Alec Thomas for enouraging us students to think, in theory. I feel very fortunate having had the opportunity to take your computational course and to teach with your guidance.

My favorite part of the graduate experience was the training I received from Drs. Takeshi Matsuoka and Stefan Kneip. Takeshi, thank you for teaching me the way an experiment should be run. Stefan, thank you for teaching me the way an experiment should be planned. I am also thankful for the diligent work from the HERCULES laser staff, Drs. Vladimir Chvykov, Galina Kalinchenko, Victor Yanovsky, and Pascal Rousseau.

Franklin, Takeshi, Will, Peng, and Schtefan, thank you for sharing many things with me: laser time, many late nights, hummous, a haircut...we have made a great team, almost like a brotherhood. To my dear wife, Ashley, thank you for running alongside me while I have chased my dream. Your love and support are just as important in my life as my own convictions.

This research was supported by the National Science Foundation, Department of Homeland Security, and the University of Michigan College of Engineering.

TABLE OF CONTENTS

LIST OF FIGURES

Figure

LIST OF TABLES

Table

LIST OF ABBREVIATIONS & SYMBOLS

ASE Amplified Spontaneous Emission

ADK Ammosov, Delone, Krainov

BSI Barrier Suppression Ionization

CCD Charge Coupled Device

CPA Chirped Pulse Amplified

FDH Frequency Domain Holography

FEL Free Electron Laser

FWHM Full Width at Half Maximum

HERCULES High Energy Repetitive CUOS LasEr System

IP Image Plate

KLM Kerr-Lens Modelocking

LWFA Laser Wakefield Acceleration or Accelerator

Nd:YAG neodymium doped yttrium aluminum garnet

PIC Particle-in-Cell

PWFA Plasma Wakefield Acceleration

RF Radio Frequency

SHO simple harmonic oscillator

Ti:S titanium doped sapphire

XPW Cross-Polarized Wave

a_0	peak normalized vector potential
a	normalized vector potential, a function of $\mathbf{r}$ and t
B	magnetic field strength
c	speed of light in vacuum
e	fundamental charge
ε_0	permittivity of free space
E	energy
$\mathcal{E}$	electric field strength
$\mathcal{E}_{wb}$	cold nonrelativistic wave breaking electric field
f	focal length
$f/\#$	f-number, where # is $f/$ aperture diameter
F_p	ponderomotive force
γ	Lorentz factor associated with electron velocity
γ_p	Lorentz factor associated with laser group and wake phase velocity
η	refractive index
I_e	beam current
I_0	peak intensity
I	intensity, a function of $\mathbf{r}$ and t
$\Delta\lambda$	wavelength shift
λ	wavelength
λ_p	nonrelativistic plasma wavelength
λ_0	initial laser central wavelength
L	length
m_e	electron mass
m_i	ion mass

μ_0	permeability of free space
n_c	classical critical electron plasma density
n_e	electron plasma density
Ω	ionization probability rate
ω_e	electron plasma frequency
ω_p	plasma frequency
ω_{pg}	relativistic electron plasma frequency
P	laser power
P_c	laser critical power for self-focusing
p	momentum
r	radius from laser axis
t	time
u_e	electron fluid element velocity
u_i	ion fluid element velocity
v_e	electron velocity
v_p	laser phase velocity
v_g	laser group velocity
v_{pw}	plasma wake phase velocity
z	laser propagation axis in lab frame
Z	atomic number

ABSTRACT

Studies of Laser Guiding and Electron Injection in a High Power Laser Wakefield Accelerator

by

Christopher S McGuffey

Co-Chairs: Karl M. Krushelnick and Alexander G. R. Thomas

This thesis describes experimental findings related to Laser Wakefield Acceleration (LWFA)- the efficient acceleration of electrons to relativistic energies using an ultraintense laser pulse to drive nonlinear waves in an underdense plasma.

In order to extract the highest possible energy from the accelerating structure, the accelerator should be operated at the lowest possible density. To date the most successful LWFA experiments have relied on self-injected, rather than externally-injected electrons. The mechanism of self-injection mandates a minimum threshold density for injection. These two requirements are conflicting as self-injection requirements limit the achievable acceleration. Additionally, a means must be found to keep the intense laser focused, or guided, over the entire length of the accelerator.

In this thesis, ablative capillaries were used to demonstrate guiding of 35 TW laser pulses. The experiment concluded that ablative capillaries can guide LWFA-relevant laser pulses to a sufficient degree to drive large amplitude relativistic plasma waves throughout 3 cm. However, capillary degradation and photoionization of the ablated material add further complication to the accelerator. No accelerated electrons were

detected in this experiment because the density was found to be too low for injection.

Another potential solution to the guiding requirement is reliance on self-guiding. The nonlinear process of self-focusing, if properly matched, can guide pulses in plasma without requiring external structures. LWFA experiments were conducted using an extended gas cell target. The transmitted laser mode was studied as a function of plasma density and focusing geometry. An appropriate range of P/P_{crit} was found over which the laser can be guided for distances as long as 19 mm.

Because of the impetus for operating at low density, any decrease in the density threshold for self-injection is beneficial. Ionization-induced injection, or injection of electrons born by ionization by the peak of the laser pulse, was found to significantly lower the injection threshold and increase the injected charge by as much as an order of magnitude compared to self-injection in a pre-ionized plasma at the same density.

The research presented here will guide upcoming experiments at Michigan and elsewhere attempting to achieve and control multi-GeV electron acceleration. Some of these experiments will rely on ionization-induced injection and self-guiding in a gas cell.

CHAPTER I

Introduction and Background

1.1 Dissertation Outline

This dissertation describes research conducted in the field of Laser Wakefield Acceleration (LWFA). This chapter discusses motivation for research in this area and provides the theoretical background required to understand research in LWFA. Chapter III describes the facilities, diagnostics, and experimental techniques used for the research in this dissertation. Chapters IV-VI present experimental results obtained in three distinct LWFA configurations. Chapter VII describes a novel injection mechanism for LWFA and discusses the role it can play in various accelerator schemes. Finally, Chapter VIII gives an overview of the electron and photon sources which have been delivered using these methods and conclusions are drawn about their applicability and future potential.

1.2 Established Electron Accelerator Technology

As a physicist, the 1920s must have been one of the most exciting decades to be alive. The discovery of nuclear decays opened a new world, and the great debate of quantum mechanics vs. determinism attracted great minds. In order to test predictions in nuclear and quantum physics, a new tool was needed- the par-

ticle accelerator. The first kind of particle accelerator- the electrostatic generator- was quickly transformed from an entertaining curiosity to an important scientific instrument. The accelerating potential of a single electrostatic accelerator stage is limited by the highest voltage which can be applied without breakdown (for example, a 10 MV Van de Graaff generator). A tandem accelerator can be used to double this maximum, and a stepped device such as a Cockcroft-Walton generator can be used to efficiently synthesize high voltage. It was soon realized however that instead of accelerating entirely in single or modular stages, acceleration to very high energies could be made more practical by applying accelerating fields which are synchronized or cyclical with the accelerating particle. This is achieved in a Radio Frequency (RF) cavity such as a linear accelerator (LINAC) by applying a potential to a series of electrodes and advancing the potential so that it stays in front of the particle. In a cyclotron or betatron, accelerating particles are constrained to spiral orbits by a magnetic field, receiving a synchronized acceleration with each revolution. A synchrotron uses controllable magnetic fields to compensate for the increased difficulty of synchronized acceleration when particles reach relativistic energies. Circular accelerator paths make the geometry of an accelerator more practical, but the bending of particles' trajectories comes with an inherent loss mechanism known as synchrotron radiation. This radiation emitted, in some cases called betatron emission, is not to be confused with the devices, the betatron or the synchrotron. Synchrotron radiation was originally considered an unfortunate loss mechanism in accelerators. However, the important applications of the radiation are now recognized and many of today's facilities generate the radiation intentionally, generally with an insertion device (undulator or wiggler) which is a series of alternating magnetic poles.

Research conducted with high energy accelerators has transformed our understanding of the universe from the subatomic to astronomical scales. Early accelerators investigated nuclear interactions, explored the stability of nuclei, and discovered

synthetic isotopes (which is still an ongoing topic of research). Accelerators have produced 16 of the 17 elementary particles predicted by the standard model and have shed light on the rules of particle interactions that shape the universe. High energy accelerators today strive to achieve $> TeV$ center-of-mass collisional energies to search for exotic particles including that 17th particle, the Higgs boson.

1.2.1 Existing Facilities and Capabilities

The Stanford Linear Accelerator Center (SLAC) (now known as the SLAC National Accelerator Laboratory) was the highest energy lepton accelerator in the world from 1966 until 1989, producing electron or positron beams with up to 50 GeV energy. Due to growing demand for x-ray light sources, SLAC was reconfigured to become the Linac Coherent Light Source (LCLS) [1], shown as a schematic in Fig. 1.1 (left), at which time a portion of the accelerator was replaced with a 132 m magnetic insertion device, see Fig. 1.1 (right). The LCLS is the first x-ray free electron laser in the world, providing x-ray pulses with 100 fs duration at 60 Hz repetition rate with photon energy in the range $0.48 - 10$ keV. A Free Electron Laser (FEL) differs from more common synchrotrons in that the emission is stimulated, producing a monochromatic, temporally coherent radiation source which also has a high degree of spatial coherence. This requires a long undulator and occurs because the electron beam and x-ray beam copropagate, causing the beam to bunch and oscillate with the same periodicity as the initial dominant x-ray wavelength. The LCLS total project baseline cost was $420M.

The strongest undulator at the Soleil facility [2] in France uses 90 undulator periods producing synchrotron light with critical energy between 3-18 keV. The Swiss Light Source [3] spectrum covers 5-40 keV. These sources do not exhibit stimulated emission and the beams have very limited temporal coherence. The Free-Electron Laser in Hamburg (FLASH) [4] at the German Electron-Synchrotron (DESY) has

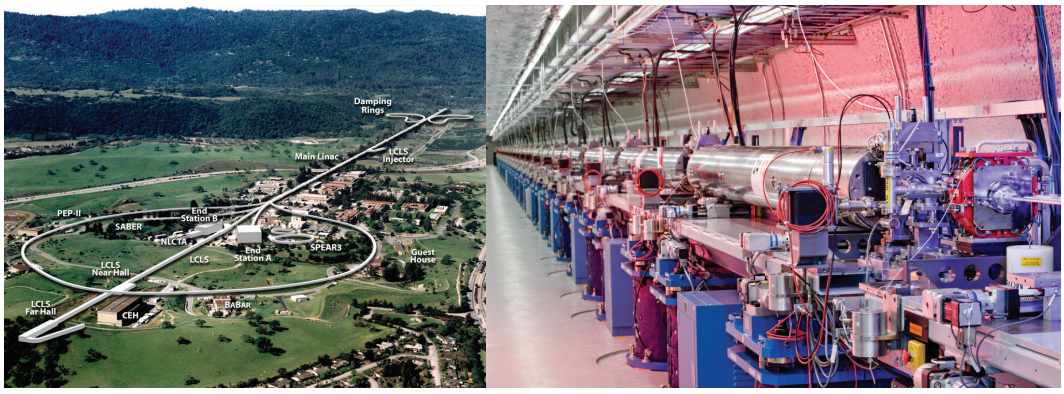

Figure 1.1: The Linac Coherent Light Source upgrade replaced the final kilometer of SLAC with an undulator and additional experimental facilities. The 132 m long LCLS undulator at SLAC. Images courtesy of the SLAC National Accelerator Laboratory.

produced coherent XUV pulses in the water window corresponding to photon energy of $200 - 300\ eV$, an important spectral range in which XUV transmission in water is much higher than in carbon, allowing high contrast imaging of organic materials in water. The European X-ray Free Electron Laser (XFEL) [5] has begun construction and is scheduled to begin operation in 2015. The project will cost an estimated 1.1B Euro. The accelerator will extend 1.7 km and accelerate electrons to 17.5 GeV. The FEL will produce 100 fs pulses with peak brightness of 5x10^{33} $photons/s/mm^2/mrad^2/0.1\%BW$. The International Linear Collider [6] is a proposed lepton collider which may be built to collide 1.6 nC pulses at 500 GeV collision energy at 14 kHz using an acceleration gradient of 31.5 MeV/m. The project would require over 31 km for the accelerator and undulator and cost an estimated $6.65B (USD).

The energy gain from any accelerator is ultimately limited by size and the accelerating gradient that can be sustained, while x-ray beam quality and photon energy are constrained by the strength and minimum practical spacing of undulator magnets and by the beam energy.

1.2.2 Applications

Electron accelerators have made many outstanding contributions to high-energy physics. While a handful of large accelerator facilities catch the headlines, there is a great number of smaller accelerators used for radiotherapy, radioisotope generation, and scientific research. Electron accelerators can be used for electron beam lithography [7] as well as for radiography or radiotherapy either directly or via x-ray generation [8]. The prevalence of smaller scale accelerators has led to their widespread use as light sources, either through bremsstrahlung or synchrotron radiation. For example:

- Probing matter such as active interogation of special nuclear materials [9]
- $\gamma-$induced nuclear transmutations [10–12]
- Free Electron Lasers [13]
- Inelestic scattering from atomic and nuclear processes [14, 15]
- Time resolved pump-probe chemistry experiments [16]
- Metallurgy, surface diffraction and scattering, crystal diffraction [17, 18]
- Protein crystallography [19] (for example, advanced light sources have been used to determine the structure of the avian flu and 1957 H2N2 viruses [20, 21]).

1.2.3 High Gradient Schemes

The maximum accelerating field strength in radiofrequency (RF) cavities used in conventional particle accelerators is fundamentally limited by the onset of electric breakdown. The maximum achievable field has increased due to new materials, the use of superconductivity, and improvements in the surface quality of the cavity. However, this limit will likely still constrain particle physics RF accelerators to the realm of

km-scale devices. The current maximum accelerating gradient is $\sim 100\ MV/m$ and typical operational gradients are $\sim 20\ MV/m$. The Compact Linear Collider, a proposed $3\ TeV, 33\ km$ accelerator has a design gradient of $150\ MV/m$ [22].

Because km-scale devices are very expensive, undeveloped schemes offering very high accelerating gradients have become of interest for future compact accelerators. For example, the electric field at the focus of today's highest power lasers is $> 10\ TV/m$. This field, however, is more difficult to use as an accelerator because it is primarily directed perpendicular to the direction of propagation, it is localized within half a wavelength, and it propagates with a phase velocity of c. For a particle to gain kinetic energy from a wave and copropagate with it (to become trapped) the particle must first be moving at nearly the phase velocity of the wave. These challenges may be overcome using clever focusing geometries and propagating in media such that the phase velocity can be ramped up to c controllably. For these schemes, the accelerating field must not be present in any medium which can be ionized, as plasmas have refractive index, $\eta \leq 1$, causing the accelerating phase fronts to outrun the particles.

Another consequence of laser propagation in a plasma is the ponderomotive force (see Sec. 2.2.4). This force may be useful for acceleration, because it advances at the laser group velocity, which is $\leq c$ and is directed in both the transverse and longitudinal directions. Schemes based on acceleration by the laser field are known as Direct Laser Acceleration (DLA) [23].

Plasma is a state of matter composed of charged particles whereby the collective behavior of the charges is driven by global charge neutrality rather than by collisions with neutral particles. Plasmas can support electrostatic waves with field strength determined by the amount of charge present. The electric field strength within these waves can reach or even exceed the cold nonrelativistic wave breaking limit, which can be estimated as [24] $\mathcal{E}_{\mathbf{WB}} = cm_e\omega_p/e$ where m_e and e are the mass and charge of an

electron respectively, and $\omega_p = \sqrt{4\pi n_e e^2/m_e}$ is the plasma frequency (see Sec. 2.1). This approximate limit can exceed the RF breakdown field by 4 orders of magnitude. These plasma waves are well-suited for particle acceleration because they can have fields along the propagation direction, have spatial scale $\lambda_p = 2\pi c/\omega_p$ in the range of 10s of μm, and propagate with phase velocity approaching c.

1.2.4 Laser Wakefield Accelerators

LWFA is a scheme of plasma acceleration in which a large-amplitude plasma wave is driven by the ponderomotive force of a high intensity laser. In 1979, the scheme was proposed [25] although lasers with appropriate parameters were not available at the time. The lasers available during the earliest LWFA experiments had pulse durations much longer than the relativistic plasma wavelength. Large-amplitude plasma waves could still be driven, however. For example, the plasma beat-wave accelerator scheme [26, 27] used two laser frequencies to form a beat wave in the laser envelope with spacing equal to the relativistic plasma wavelength. Acceleration was observed for externally-injected electrons [28] using beat waves from a carbon dioxide laser. Later LWFA schemes relied on the self-modulation by the wave itself [29–34], which is discussed further in Sec. 2.2.3. These schemes relied on external injection or injection by wavebreaking [35, 36], a process which causes chaotic disruption of electron phase space.

As sub-100 fs lasers became available with higher energy, allowing self-injection at lower density, LWFA moved from the self-modulated regime to the forced wakefield regime [37] to the bubble regime which will be described in Sec. 2.2.4. In 2004, three groups independently reported experimental observation of ~ 100 MeV quasimonoenergetic beams [38–40], which were made possible by self-injection rather than wavebreaking. Later, acceleration in a 3 cm capillary waveguide led to generation of a 1 GeV quasimonoenergetic beam [41]. The recent advance of LWFA research is

documented in over 500 scientific journal publications and review papers [42–44].

While LWFA and other plasma-based accelerator schemes show a great deal of promise for constructing compact economical electron beam sources at moderate energy, it remains to be seen if such accelerators can be scaled to the energy frontier while retaining the cost and size benefits. Research is being conducted at many institutions around the world to assess the scalability, and the BELLA testbed facility at Lawrence Berkeley National Laboratory was recently funded. Designs for multiple-stage TeV-class laser wakefield accelerators have been presented [45]. However, new discoveries are still being made in the field, and some fundamental questions about these accelerators must be answered before a design of a large scale device can be selected. Some of the challenges of scaling to the energy frontier are explored in this thesis. Laser wakefield accelerators could contribute to high energy physics if they can economically scale to the TeV energy range. At lower energies, the applications of their electron beams are primarily for industry and medical treatment, though ion beams are expected to offer benefits in the treatment of tumors [46].

One particularly important application of LWFA outside of high energy physics is radiation generation. LWFA-driven electron beams can be injected into conventional undulator systems which convert some of the electron beam energy into a pulse of collimated synchrotron radiation. Low mass electrons are the preferred beam species for generating synchrotron radiation in these devices. The advantage of using a LWFA beam as opposed to a conventional RF accelerator beam is that LWFA beams likely have pulse durations as short as a few fs. Assuming the synchrotron radiation also exhibits this ultra-short pulse duration, it could be used as a probe to temporally-resolve the evolution of ultrafast phenomena such as material crystalization and chemical synthesis. Synchrotron radiation from LWFA-driven sources has so far been limited to the optical and VUV spectral range, which is limited by the smallest undulator magnet spacing which can be assembled (several mm). It was realized, however, that

undulating structures can be created which are composed of the plasma wakefield itself and having features with μm scale, leading to undulator or wiggler radiation in the x-ray range. The difference between undulator radiation and wiggler radiation will be discussed in Sec. 2.3. In addition to making the applications described in Sec. 1.2.2 available to a wider range of users and with potentially reduced scale and cost, the laser-driven electron and x-ray sources investigated in this dissertation could offer improvements in pulse duration, spectrum, and source size. The research presented here has explored several schemes for laser wakefield accelerators, elucidated subtle processes taking place in these accelerators, and led to the discovery of a new mechanism for self-injection into a LWFA.

CHAPTER II

Theoretical Background

2.1 Plasma Oscillations and Waves

The plasma frequency gives the inverse of the response time for a specific species within a plasma. This timescale gives the shortest observation period over which a system can demonstrate behaviors characteristic of a plasma. In App. A, the fluid equations are linearized in order to determine the response of a cold, unmagnetized plasma to a density perturbation. This analysis reveals that a plasma will exhibit oscillations at the plasma frequency, Eq. 2.1. It is also shown that for a simple electron-ion plasma, the electron plasma frequency is larger than the frequency for other species and therefore the term plasma frequency most often refers to the electron plasma frequency alone.

$$\omega_p \equiv \omega_e = \sqrt{\frac{4\pi e^2 n_e}{m_e}}. \tag{2.1}$$

Plasma electrons in the volume of a high intensity laser experience relativistic quiver motion and increased effective mass. The plasma frequency is therefore altered to be

$$\omega_{pg} = \sqrt{\frac{4\pi e^2 n_e}{\gamma m_e}}. \tag{2.2}$$

By similarly considering the linearized wave equations in a plasma it can be shown

that electromagnetic waves in a cold collisionless plasma experience an index of refraction $\eta = \sqrt{1 - \omega_p^2/\omega^2}$ where the frequency ω and wave number k must obey the plasma dispersion relation $\omega^2 = k^2c^2 + \omega_p^2$. The wave's position on this curve determines the phase velocity ($\omega/k = c/\eta$) and group velocity ($d\omega/dk$). Differentiation of the dispersion relation with respect to k yields $v_p v_g = c^2$, indicating that the electromagnetic wave can propagate in plasma with

$$v_p > c > v_g \tag{2.3}$$

so long as $\omega > \omega_p$.

2.2 Laser Wakefield Accelerators

2.2.1 Relevant Lasers

Advanced LWFA schemes required ultrashort, high intensity laser drivers only made available by the development of Chirped Pulse Amplified (CPA) lasers (described in Ch. III) in the late 1980s. CPA lasers can achieve intensities corresponding to electric fields well in excess of atomic fields, making possible field ionization by quantum tunneling and by barrier suppression ionization. An analytical framework for calculating the ionization rate for complex atoms and ions was developed by Ammosov, Delone, and Krainov [47]. If this rate is greater than the laser frequency, significant tunneling ionization will occur. Ionization will be discussed in the Sec. 2.2.2 and in Ch. VII.

Laser electric fields are even strong enough to drive an electron to relativistic quiver motion. When the momentum associated with the relativistic quiver motion of such an electron is equal to $m_e c$, the normalized vector potential, $a_0 = \frac{e\mathcal{E}}{m_e \omega_0 c}$ is equal to 1. A laser pulse with $a_0 \ll 1$ can propagate in a plasma with density up to the critical density n_c, which is the density at which the plasma frequency is high

enough to screen out the laser wave, while a laser with $a_0 > 1$ can propagate even in density $> n_c$ via relativistic induced transparency.

2.2.2 Laser Field Ionization

In this section, expressions are given in atomic units, whereby energies and potentials are given in units of the Hartree energy, or twice the ionization energy of hydrogen in its ground state, and electric fields are given relative to the electric field present one Bohr radius from a positive charge of magnitude e. The field of a high intensity laser can severely modify the Coulomb potential experienced by an electron bound to an atom or ion. Absolute understanding of the system requires solution of the time-dependent Schrödinger equation (TDSE) using appropriately chosen atomic potential and laser field models. Field ionization can occur by multiphoton absorption [48, 49] or by tunneling, with the dominant mechanism determined by the Keldysh parameter [50]: $\gamma_K = \sqrt{U_s/2U_p}$ where U_s is the ionization potential of the bound state and U_p is the ponderomotive potential associated with the laser field. γ_K also indicates the ratio of the laser frequency to the ionization rate. For $\gamma_K \ll 1$, which is the case for the intensities explored in this thesis, tunneling ionization is the dominant mechanism. A laser field above the barrier suppression ionization field $\mathcal{E}_{BSI} = U_s^2/4$ is strong enough to suppress the atomic binding potential to below an electron's ground state energy, allowing direct ionization without tunneling.

Simplified analytical models allow estimation of ionization rates without explicitly solving the TDSE. For example, the model created by Ammosov, Delone, and Krainov [47] (the ADK model) predicts the ionization rate due to tunneling for atomic species in the presence of an alternating electric field. The ADK model is an extension of the ionization probability rate proposed by Perelemov in 1966 [51] and has since been extended to include electron ionization in molecular systems [52]. Ref. [47] gives formulas for calculating the probability rate of ionization, Ω, for various atomic

configurations. One example (as corrected in Ref. [53]) is

$$\Omega = \left(\frac{3\tilde{e}}{\pi}\right)^{3/2} Z_f^2 n_{eff}^{-9/2} \left(\frac{16\tilde{e}U_s^2}{Z_f\mathcal{E}}\right)^{2n_{eff}-3/2} \exp\left[\frac{-2(2U_s)^{3/2}}{3\mathcal{E}}\right] \tag{2.4}$$

where $\tilde{e}$ is Euler's number, Z_f is the charge state of the ion after ionization, $n_{eff} = Z_f/\sqrt{2U_s}$ is the effective principal quantum number and this formula is valid for atoms with orbital quantum number $l = 1$ and $m = 0$. The number of ions in charge state $S + 1$ then is

$$N_{S+1} = \int\limits_{x,y,z} \int\limits_{t} n_S(x, y, z, t)\Omega(\mathcal{E})dxdydzdt \tag{2.5}$$

where n_S is the density of particles in state S. The number of electrons at $t = \infty$ (assuming no recombination) is

$$N_{e\infty} = \sum_{s=1}^{Z} (SN_S) \tag{2.6}$$

.

The ADK model assumes the laser electric field strength $\mathcal{E}_L \ll \mathcal{E}_{atomic}$. For the intensities relevant to this thesis, however, $\mathcal{E}_L \gg \mathcal{E}_{atomic}$ near the peak of the pulse in most cases. In these cases ionization can be modeled in a barrier suppression picture in which a threshold intensity value is assumed, above which the probability of ionizing a particular charge state is 1. Therefore the ADK model is only applicable in this thesis to the exceptional cases of high charge states where $\mathcal{E}_{atomic} \gg \mathcal{E}_L$. The Barrier Suppression Ionization (BSI) model given in Ref. [54] estimates the intensity thresholds for ionization of a state with ionization potential U_s as $I_s = cU_s^4/128\pi e^6 Z_f^2$.

Fig. 2.1 shows the required laser intensity and corresponding power for field ionization of atomic and ionic species using the BSI model and the ADK model. Power cited on the right vertical axis is the peak intensity multiplied by the area of a 11.3 μm diameter round spot. The plotted intensities for the BSI data points are

the appearance intensities from Ref. [54]; the ADK points give the intensity at which $\Omega(I) \times 30\ fs = 1$. Only one data point is calculated for argon using the ADK model.

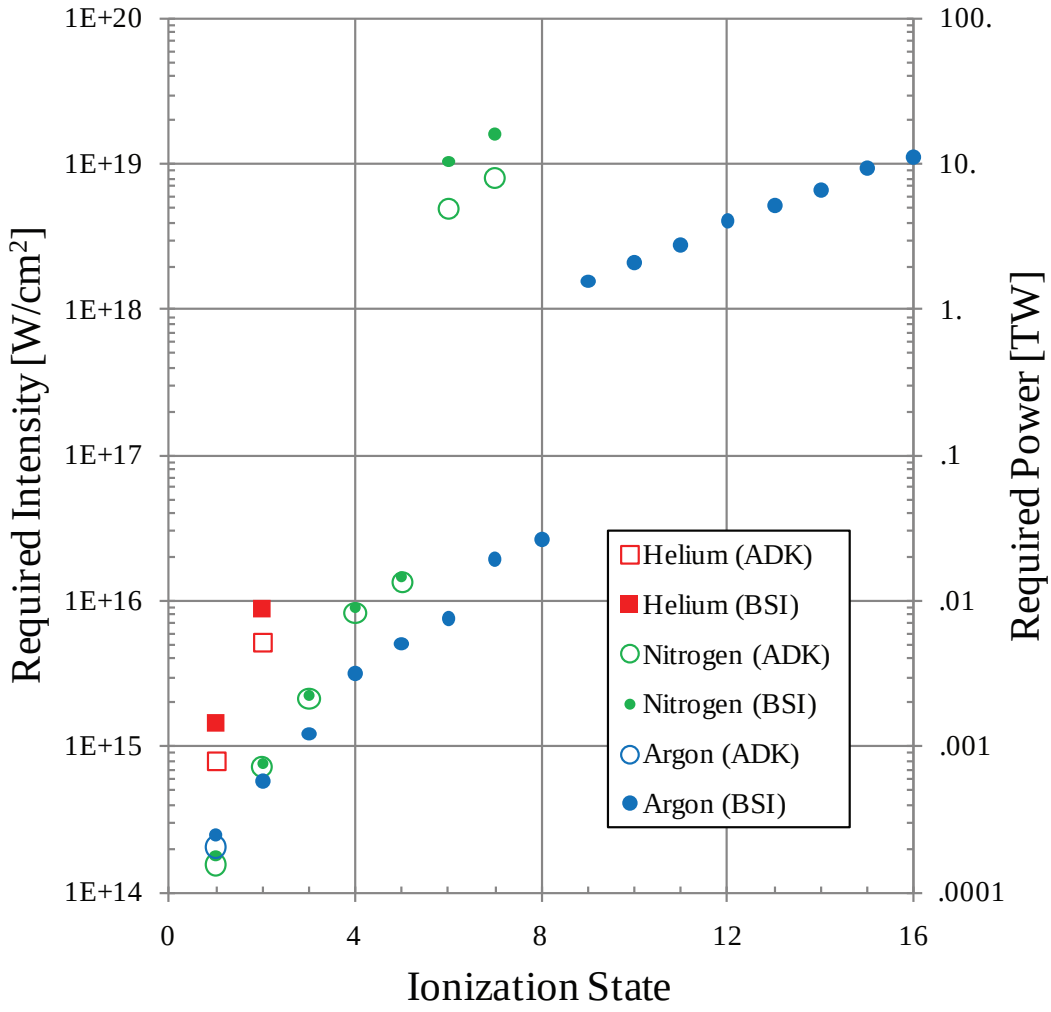

Figure 2.1: Appearance intensity and corresponding power (for an 11.3 μm spot) for field ionization of atomic and ionic species using the BSI model (filled points) and the ADK model (open points). Only one data point is calculated for argon using the ADK model.

Field ionization is responsible for producing the plasmas relevant to this thesis but ionization can also play a role in the dynamics of wakefield acceleration (Chs. V, VII) and affect the laser propagation behavior. As a laser enters and field ionizes a gas, the index of refraction varies spatially and temporally over the laser rise-time.

This temporally varying index leads to an overall shift of frequencies at the front of the laser pulse to higher frequency [55–57].

2.2.3 Laser Propagation in Underdense Plasma

High intensity laser pulses propagating in plasma are dramatically affected by nonlinear optical phenomena. Light in any material experiences some degree of nonlinearity whereby the material exhibits an index of refraction dependent not only on linear material properties but also on the local intensity. The index of refraction for a material with inversion symmetry can be written as $\eta = \eta_0 + \eta_2 I$ where η_2 is the nonlinear index describing the strength of the nonlinearity. This is known as the optical Kerr effect. Because laser pulses have non-uniform (*e.g.* Gaussian) temporal and transverse profiles, nonlinearity causes uniform optical components to behave as if they were non-uniform.

The optical Kerr effect due to the rise and fall of a laser pulse in the temporal domain leads to self-phase modulation and self-steepening. Self-phase modulation causes frequencies present in the laser spectrum to be shifted according to $\Delta\omega \sim \frac{\partial\phi}{\partial t}$ where ϕ is the phase. This shift can lead to new frequency content and even overall spectral broadening. Extra frequency content allows self-steepening. When self-phase modulation is combined with dispersion in a plasma, the laser can be compressed to a pulse duration even shorter than its original bandwidth-limited pulse duration.

The Kerr effect attributable to the transverse laser profile leads to self-focusing because the index of refraction is greatest on axis. Phase fronts at the periphery will advance faster than phase fronts on axis, resulting in inward curvature. Propagation of light in a nonlinear medium can be described by the Helmholtz equation,

$$(\nabla^2 + \eta^2(I)k_0^2)\mathcal{E} = 0 \tag{2.7}$$

where $\eta(I) = \eta_0 + \eta_{NL}(I)$ and $\mathcal{E} = \mathcal{E}_0(r,z)\exp -i\eta_0 k_0 z$, which assumes that $\mathcal{E}_0(r,z)$ varies slowly over the scale of the laser wavelength. Eq. 2.7 can be approximated [58] to

$$\frac{\partial^2 \mathcal{E}_0}{\partial r^2} - 2i\eta_0 k_0 \frac{\partial \mathcal{E}_0}{\partial z} + k_0^2[\eta^2(I) - \eta_0^2]\mathcal{E} = 0 \tag{2.8}$$

For $\eta_2 I \ll \eta_0$, the bracketed terms can simplify to $[\eta_{NL}(I)][2\eta_0]$. For the case of Kerr self-focusing, $\eta_{NL}(I) = \eta_2 I$ which makes the bracketed terms $\frac{\eta_2 \eta_0^2 |\mathcal{E}_0|^2}{Z_0}$ where $I(r,z) = \frac{\eta_0 |\mathcal{E}_0|^2}{2Z_0}$ and Z_0 is the impedance of free space. Replacement into Eq. 2.8 gives the nonlinear Schrödinger equation (NLSE):

$$\frac{\partial^2 \mathcal{E}_0}{\partial r^2} - 2i\eta_0 k_0 \frac{\partial \mathcal{E}_0}{\partial z} + \eta_0^2 k_0^2 \frac{\eta_2}{Z_0} |\mathcal{E}_0|^2 \mathcal{E} = 0 \tag{2.9}$$

One possible solution of this equation is the spatial soliton, or guided pulse, $\mathcal{E}(r,z) = \mathcal{E}(0,0)\text{sech}\,(\frac{r}{w_0})\exp\,(-i\frac{z}{4z_R})$ where $z_R = \pi w_0^2/\lambda$ is the Rayleigh range. This propagation mode has constant transverse profile independent of z. This occurs only for the boundary condition where the laser spot is equal to a particular "matched" spot size. For unmatched cases, the spot size will oscillate as it propagates along z.

Lasers can also be affected by the plasma waves they generate. The wave's density deficit (or excess), δn is the net difference in density relative to the background density $\delta n = n(r,z) - n_p$. For a pulse longer than many plasma wavelengths, the refractive index becomes modulated in space by the wave causing the beam to breakup into a pulse train. The ponderomotive force of the pulses causes stronger driving of the wave. The steep ramps of δn in the longitudinal direction cause spectral phase modification resulting in photon acceleration [59], typically resulting in a redshift of light at the front of the wave (where density is decreasing with ζ) and blueshift of light at the rear if the pulse completely fills the bubble. Additionally, δn has radial dependence which can cause focusing or defocusing.

The index of refraction of a laser in a very underdense plasma will include some

or all of the terms listed in Eqn. 2.10

$$\eta(r,\zeta) \cong 1 - \frac{\omega_{pg}^2}{2\omega_0^2}\left(1 + \frac{\delta n}{n_p}\right) \tag{2.10}$$

which is valid so long as $\frac{\omega_{pg}^2}{\omega_0^2} \ll 1$ and $a_0 \ll 1$ where $\omega_{pg}^2 = \frac{n_p e^2}{\gamma m_e \epsilon_0}$ and γ is the relativistic factor associated with electron quiver velocity within the laser field. Radial dependence comes from γ (the cause of "relativistic self-focusing") and δn, which has contributions from "ponderomotive self-chanelling", displacement by the plasma wave and the amount of electrons introduced by ionization.

The propagation of a laser mode in such a plasma can be determined by replacing $\eta(I)$ in Eq. 2.7 with the terms above, applying the slowly varying envelope approximation, and solving the resulting NLSE. Ionization, for example, adds the term $-\eta_0 k_0^2 \frac{n_e}{n_{crit}}\mathcal{E}$ to the LHS of Eq. 2.9 and $\frac{\partial n_e}{\partial t} = n_{atomic} \times \Omega(I)$ where Ω is the ionization probability rate. This defocusing term can also cause the laser spot to oscillate with propagation as self-focusing leads to increased ionization on axis, which leads to defocusing, which leads to decreased ionization and so on. Ionization defocusing was investigated in Ref. [60]. Ref. [61] analyzes guiding behavior under the influence of ionization and many other conditions.

Because there will always be some portion of the leading edge of the pulse which does not experience self-focusing, short pulses which are self-guided may lose a significant portion of their energy rapidly. Additionally, ultrashort pulses are expected to have diminished efficacy of self-focusing [62]. In spite of this expectation, self-focusing has been observed for pulses with $\tau\omega_p \sim 1$ [63–66]. Multiple-filament self-focusing due to the relativistic and ponderomotive terms has been analyzed in Ref. [67].

2.2.4 Laser-driven Plasma Waves

2.2.4.1 The Ponderomotive Force

Laser-driven plasma waves are waves driven by the ponderomotive force of an intense laser. A particle with charge q within electric and magnetic fields $\mathcal{E}$ and $\mathbf{B}$ will experience the Lorentz force given by

$$\mathbf{F} = \frac{\mathbf{d}}{\mathbf{dt}}\mathbf{p} = \mathbf{q}(\mathcal{E} + \mathbf{v} \times \mathbf{B}) \tag{2.11}$$

For the case of a charge in the electromagnetic field associated with a laser, the motion of the charge is often simplified to that of a harmonic oscillator driven only by the electric field. However, for strong, steeply varying laser fields the effects of the field non-uniformity and the $\mathbf{v} \times \mathbf{B}$ term cannot be ignored. The motion can be separated into oscillations on the timescale of the laser field and a drift over longer timescales. The apparent force responsible for this drift is called the ponderomotive force. This force causes both longitudinal and transverse motion. Written in units convenient for this thesis, the linear ponderomotive force on an electron is [44]

$$\mathbf{F_p} = -m_e c^2 \nabla (a^2/2) \tag{2.12}$$

where $\mathbf{a} = e\mathbf{A}/m_e c^2$ is the normalized vector potential of the laser field, which has peak $a_0^2 = 7.3\text{x}10^{-19}[\lambda(\mu m)]^2[I_0(W/cm^2)]$ and where the linear regime is the case such that $a^2 \ll 1$.

The 3D relativistic ponderomotive force for a charge within a laser pulse with pulse duration $\tau \gg T = 2\pi/\omega_0$ can be derived as follows: The Lorentz force, Eq. 2.11 can be rewritten in terms of the magnetic vector potential $\mathbf{A}$ and electric scalar

potential ϕ which are defined as

$$\mathbf{B} = \nabla \times \mathbf{A} \tag{2.13}$$

$$\mathcal{E} = -\nabla\phi - \frac{\partial \mathbf{A}}{\partial t} \tag{2.14}$$

giving

$$\frac{d}{dt}\mathbf{p} = q\left(-\frac{\partial \mathbf{A}}{\partial t} - \nabla\phi + \mathbf{v} \times \nabla \times \mathbf{A}\right) \tag{2.15}$$

The partial derivative in the first term on the right hand side can be related to the total, or convective derivative

$$\frac{d\mathbf{A}}{dt} = \frac{\partial \mathbf{A}}{\partial t} + \frac{d\mathbf{r}}{dt} \cdot \frac{\partial \mathbf{A}}{\partial r} \tag{2.16}$$

which gives the total rate of change of $\mathbf{A}$ as the particle moves within a region where $\mathbf{A}$ is non-uniform. Eq. 2.15 can now be written

$$\frac{d}{dt}\mathbf{p} + q\mathbf{A} = q\left(\mathbf{v} \cdot \nabla\mathbf{A} - \nabla\phi + \mathbf{v} \times \nabla \times \mathbf{A}\right) \tag{2.17}$$

This equation can be simplified using the vector identity $\mathbf{v}\cdot\nabla\mathbf{A}+\mathbf{v}\times\nabla\times\mathbf{A} = (\nabla\mathbf{A})\cdot\mathbf{v}$ to give

$$\frac{d}{dt}\mathbf{p} + q\mathbf{A} = q(\nabla\mathbf{A}) \cdot \mathbf{v} - q\nabla\phi \tag{2.18}$$

Replacing $\mathbf{v}$ with $\mathbf{p}/m\gamma$ and introducing the canonical momentum $\mathbf{p_0} = \mathbf{p} + q\mathbf{A}$ gives

$$\begin{aligned} \frac{d}{dt}\mathbf{p_0} &= \frac{q}{\gamma}(\nabla\mathbf{A}) \cdot (\mathbf{p_0} - q\mathbf{A}) - q\nabla\phi \\ &= \frac{-q^2}{2m\gamma}(\nabla\mathbf{A}^2) + \frac{q}{m\gamma}\nabla\mathbf{A} \cdot (\mathbf{p_0}) - q\nabla\phi \end{aligned} \tag{2.19}$$

ϕ represents the electrostatic potential due to all charges. Thus for the simple case of a single charge in vacuum the last term will be ignored. The long timescale (for

observation time $\gg T$) drift motion can be isolated by taking the time average of both sides of Eq. 2.19 over one wave period $T = 2\pi/\omega_0$. This gives

$$\left\langle \frac{d}{dt}\mathbf{p_0} \right\rangle = \left\langle \frac{-q^2}{2m\gamma}(\nabla \mathbf{A}^2) \right\rangle + \left\langle \frac{q}{m\gamma}(\nabla \mathbf{A}) \cdot \mathbf{p_0} \right\rangle \tag{2.20}$$

where angle brackets indicate time averaging:

$$\langle \Box \rangle = \frac{1}{T} \int_t^{t+T} dt' \Box \tag{2.21}$$

The last term in Eq. 2.20 must be integrated by parts, yielding two terms each proportional to $\langle A \rangle$. For the case as we are considering the case $\tau \gg T$, the envelope of the field can be assumed to remain nearly constant over one wave period. If we further assume that the spatial extent of the field $w \gg 1/k$ where k is the wavenumber, the value $\langle A \rangle \approx 0$. This leaves

$$\left\langle \frac{d}{dt}\mathbf{p_0} \right\rangle \equiv \mathbf{F_p}(\mathbf{r}, t) = -\left\langle \frac{q^2}{2m\gamma} \nabla \mathbf{A}^2 \right\rangle \propto \left\langle \nabla \frac{\mathcal{E}^2}{\gamma \omega_0^2} \right\rangle \tag{2.22}$$

This equation states that charges will move away from regions of high field pressure with force dependent on the laser frequency and the particle's mass and charge but not on the sign of the charge.

2.2.4.2 Linear Plasma Waves

The linear ponderomotive force given by 2.12 can be inserted into the linearized fluid equations as a driving term. The solution to the resulting partial differential equation describes a linear wakefield.

$$n_1 = n_0(c^2/\omega_p) \int_0^t dt' \sin[\omega_p(t - t')] \nabla^2 a^2(\mathbf{r}, t')/2 \tag{2.23}$$

A cold nonrelativistic sinusoidal plasma wave can have peak electric field up to $\mathcal{E}_{wb} = cm_e\omega_p/e$. For a linear wave driven by a near infrared laser in a plasma of 1/100th critical density, this value is 400 GV/m. A linear plasma wave was visualized using optical probing with interferometric [68] and Frequency Domain Holography (FDH) [69] techniques.

2.2.4.3 Nonlinear Plasma Waves

When the driver is capable of driving a wave such that $\delta n \ll n$ is no longer valid, the linear perturbation treatment of the fluid equations is also no longer valid. Instead of a sinusoidal variation, the density perturbations become sharply peaked. The electrostatic field which can be present in such a plasma can greatly exceed the value $\mathcal{E}_{wb}$ by a factor of $a_0^2/(1 + a_0^2)^{1/2}$ for a plane wave driver with FWHM pulse length $c\tau = \lambda_p/2$.

In the highly nonlinear "bubble regime", electrons are fully expelled by the laser [70], leaving an approximately spherical "bubble" [71]. The electric field present within this bubble varies approximately linearly in all three spatial dimensions of the reference frame traveling with the laser [72, 73]. In other words, electrons see the bubble as a parabolic potential well. This shape is well suited for electron acceleration because it provides both a longitudinal accelerating and a radial focusing field. Ref. [71] suggests this can be achieved most efficiently with a few-cycle pulse, which is being investigated at the Max Planck Institute [74, 75]. The FDH technique was extended for application to wakefields in the bubble regime in an experiment carried out in part by this author in Refs. [76, 77].

Driving a plasma wave in the bubble regime requires expulsion of electrons to a blowout radius $r_{blow} > r_b$, where r_b is the bubble radius, as well as a strong enough bubble electrostatic field to pull the electrons back to the laser axis at the back of

the bubble. Additionally the pulse duration obeying

$$c\tau < \lambda_p. \tag{2.24}$$

The blowout radius is determined by the laser spotsize. Balance of the bubble electrostatic field with the ponderomotive force leads to the matched spot condition indicative of operation within the bubble regime [78]:

$$k_p r_b \approx 2\sqrt{a_0}. \tag{2.25}$$

The shape of the bubble is determined by the trajectories of the expelled electrons as they return to the bubble, forming a thin sheath. The bubble was computationally found to be spherical for the case $r_b = 4c/\omega_p$, which combined with the matched spot condition requires a laser power of $8P_{crit}$. Further evaluation and scaling laws for the bubble regime are discussed in Refs. [79–81].

2.2.4.4 Raman Scattering

An electromagnetic wave with frequency ω_0 and wave number $\mathbf{k_0}$ propagating in a plasma can undergo a number of parametric instabilities whereby the wave excites new electrostatic or electromagnetic waves. One example of this is Raman scattering, in which the new waves are a plasma wave with frequency ω_p and wave number $\mathbf{k_p}$ and a scattered electromagnetic wave with properties ω_s and wave number $\mathbf{k_s}$. The two waves must obey the phase matching conditions:

$$\omega_0 = \omega_{pw} + \omega_s, \mathbf{k_0} = \mathbf{k_{pw}} + \mathbf{k_s} \tag{2.26}$$

which can lead to scattered light with frequency $\omega_0 \pm \omega_p$. Scattered light with frequency $\omega_0 - \omega_p$ is known as the Stokes line and light with frequency $\omega_0 + \omega_p$ is known

as the anti-Stokes line. For the case of a large amplitude electromagnetic wave coupling with a low amplitude density perturbation with frequency ω and wave number $\mathbf{k}$, "stimulated" Raman scattering can generate a scattered light wave and a plasma wave seeded by the density perturbation. This occurs for light pulses with pulse length greater than the plasma wavelength, as the plasma wave modulates the pulse envelope. The plasma wave must obey the dispersion relation [82, 83]:

$$\omega^2 - \omega_{pw}^2 = \frac{\omega_p^2 k^2 c^2 a_0^2}{2}\left(\frac{1}{D_+} + \frac{1}{D_-}\right) \tag{2.27}$$

where $D_\pm \equiv \omega_\pm^2 - k_\pm^2 c^2 - \omega_{pw}^2 = \omega^2 - k^2 c^2 \pm 2(\omega\omega_0 - c^2 \mathbf{k}\cdot\mathbf{k_0})$ and ω_+, k_+ correspond to the anti-Stokes case (where motion is driven at the sideband $\omega + \omega_0$) and ω_-, k_- correspond to the Stokes case. The cases of Raman back-scatter (where the k-vector of the scattered light is oppositely directed from that of the initial light) and Raman side-scatter (where the k-vector of the scattered light is perpendicular to that of the initial light) can exhibit resonance in Eq. 2.27 only for the Stokes case, which leads to resonant coupling of the initial electromagnetic wave into the scattered wave and plasma wave. Stimulated Raman back-scatter can be an important loss mechanism in some laser-plasma interaction and also plays an important role in wakefield acceleration in the self-modulated regime discussed in Secs. 1.2.4 & 2.2.3. Raman side-scatter is used as a diagnostic of the plasma and of the laser pulse as discussed in Sec. 4.3.1.

2.2.5 Injection into the Wakefield

One of the obstacles for producing high energy electron beams using a single stage LWFA is the necessity for extending the acceleration length, which is accomplished by lowering the plasma density. Counter to that attempt, it has been found that for a given plasma density, there is a minimum laser power for which self-injection will occur, or alternatively for a given power there is a density threshold.

Injection by wavebreaking was observed in 1995 [36] and evaluated analytically and computationally in 1998 [84]. However, the details of the self-injection mechanism for electrons interacting with a short-pulse laser and preformed bubble structure are still debated. Analytical formulations of self-injection have to date only modeled cases with a non-evolving driver. Self-injection is not deeply understood, even through computational modeling. Refs. [81, 85] specifically investigated injection conditions using Particle-in-Cell (PIC) codes and Ref. [86] developed an analytical model, though they each came to slightly different conclusions. Ref. [81] and [86] suggest density (or bubble size) thresholds for injection and [85] suggests that the evolution of the bubble size, rather than the size itself, is most important. Many experiments in the bubble regime have indicated a density threshold for injection [87]. What is certain is that the majority of electrons are perturbed by the ponderomotive force, pass the bubble without becoming trapped, and continue plasma oscillations without extracting significant energy from the wave. However, some subset of electrons can have appropriate initial conditions to end up in a trapped trajectory. These are the electrons which gain longitudinal momentum quickly enough to become trapped within one crossing at the rear sheath of the bubble. They must reach nearly the wake phase velocity.

A single electron analytical model may be more instructive for understanding the injection process than PIC modeling even though it includes less physics. The Hamiltonian for an electron experiencing the potential of a wake $\Psi = \Phi - \frac{v_g}{c}A_z$ is $H = \gamma m_e c^2 - v_g \gamma m_e v_z - e\Psi$ along that electron's trajectory where Φ and A are the scalar and vector potentials of the wake and the value of H is determined by the electron's initial conditions. A subset of the electron population- those with H less than a threshold (separatrix) value- can become trapped. An approximate trapping requirement is that $v_z(r = 0) = v_g$. As density is increased, v_g decreases, easing the trapping condition. This results in higher trapped charge and trapping of electrons

with a wider range of trapping positions and momenta.

Refs. [85, 86] analytically investigate single electron trajectories in the vicinity of a two-dimensional circular bubble with radius R and nearly linear internal potentials and surrounded by a "sheath" region with thickness $\ll R$ and opposing potential. In a frame comoving with the bubble structure at a speed v_g relative to the lab frame, the coordinate $\zeta = z - v_g t$ is introduced and y is the coordinate transverse to propagation. The bubble is centered at $\zeta, y = 0$. For a quiescent electron initially located at $\zeta > R, y_0 \sim \ r$ for which the laser field is ignored, Ref. [86] reports a range of initial transverse position which will result in trapping: $y_{crit} \lesssim y_0 \lesssim R$ where y_{crit} is a threshold value. This acceptance shell exists and trapping occurs so long as $R\omega_p/c \gtrsim \sqrt{2}\gamma_p$. where γ_p is the relativistic factor associated with bubble propagation, $\gamma_p \simeq \omega_0/\omega_p\sqrt{3}$. Ref. [85] used a similar model but allowed the bubble size to change in time. In that model, trapping does not occur regardless of initial position unless the bubble expands, resulting in a time-dependent Hamiltonian. The trapping condition for this model is that $\Delta H < -m_e c^2$. Ref. [88] similarly models a bubble and sheath, and finds that for a fixed bubble size, trapping trajectories exist so long as $R\omega_p/c \gtrsim 2\sqrt{\ln 2\gamma_p^2 - 1}$.

Methods have been found to aid injection by altering the dynamics including creation of a steep standing wave using a second "colliding" pulse [89–93], manipulating the density profile [94], and allowing ionization in the proximity of the main pulse (Ch. VII).

A related topic of discussion is beam loading of the plasma structure by trapped charge. As trapped charge in the bubble accumulates, the electric field at the rear of the bubble is diminished, limiting injection to a brief instant and preventing wave-breaking. Beam loading limits the trapped charge but also allows the trapped bunch to be accelerated en masse, producing a monoenergetic beam. These issues are discussed in Refs. [95, 96].

2.2.6 Acceleration

The peak electron energy from LWFAs scales as the inverse of the plasma density; however since the accelerating electric fields within the plasma also decrease with decreasing density ($E \propto n_e^{1/2}$). This means that the acceleration distances required to achieve energies of several GeV need to be many centimeters. In fact the acceleration distance increases like $n_e^{-3/2}$, which is due to dephasing considerations. This dephasing length is the distance over which fast electrons outrun the accelerating part of the relativistic plasma wave generated in these interactions.

The acceleration distance in experiments can also be limited due to laser pump depletion as energy is lost in the generation of the large amplitude wakefields in the plasma. As described in Ref. [97], the leading edge of a laser pulse loses energy by driving a nonlinear wake. The front of the pulse erodes away with a velocity $v_{etch} = -c\frac{\omega_p^2}{\omega_0^2}$ relative to the group velocity of the laser. This means the laser will be completely depleted after traveling a distance $L_{depl} = v_g \frac{c\tau\omega_0^2}{\omega_p^2} \propto \frac{1}{n_e}$.

For efficiently generating a spherical plasma bubble, the spot size of the laser pulse should be about the relativistic plasma wavelength which scales inversely as the square root of the plasma density. This means that as the plasma density decreases the natural laser diffraction distance (Rayleigh range) increases much more slowly than the dephasing and depletion distances, implying that extending the interaction distance beyond a Rayleigh range is critical for the generation of multi-GeV electron beams. Consequently there have been many previous experiments to demonstrate techniques to guide high intensity lasers in a plasma over distances longer than the diffraction distance, which will be discussed further in Chs. V & VI.

The scalings of these lengths are shown in Fig. 2.2(left). Constrained to the bubble regime requirements, both the dephasing length and depletion length scale as $n_e^{-3/2}$ and the energy gain scales as n_e^{-1}. This means the energy gain scales less than linearly with accelerator length whereas an RF accelerator has gain that scales

linearly with length. Based on the currently achievable accelerating fields for these two technologies, single stage LWFAs in the bubble regime should be more compact than RF accelerators for accelerator length up to $10,000\ km$ ($E = 1000\ TeV$). However, a single-stage LWFA has practical limitations which diminish this advantage such as the scale and number of non-compact lasers that would be necessary. In Fig. 2.2(right) are shown the scalings of the focal length of the focusing optic (assuming a 10 cm beam diameter), and the laser pulse energy. The parameters for these scalings are chosen such that the bubble criteria Eqs. 2.24 and 2.25 are satisfied. The final curve (right, red) is plotted with the additional constraint that laser power $P = 10 \times P_{crit}$, which, we will see in Sec. 6.3.2, is a rough requirement for self-guiding of ultrashort pulses.

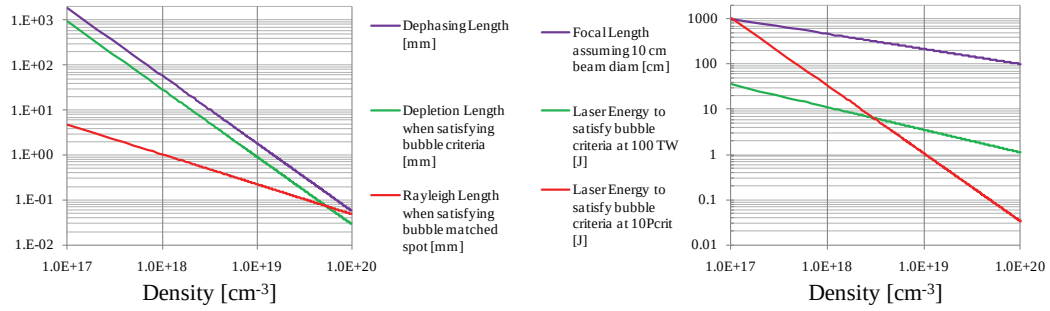

Figure 2.2: Scaling of relevant acceleration-limiting lengths and required parameters for operation in the bubble regime.

Refs. [41, 98] have demonstrated acceleration with energy gain in accordance with the maximum achievable values predicted by scalings in the bubble regime. Ref. [99] experimentally investigated the acceleration process by adjusting acceleration length *in-situ*.

In practice, a high energy LWFA design is likely to incorporate an injector stage operating in the bubble regime followed by many stages operating in the linear wake-field regime. This design would produce high charge monoenergetic beams in the first stage and the majority of energy gain would be achieved in the more controllable

linear stages.

2.3 Radiation Generation

Electron accelerators have been used extensively for generation of radiation using bending magnets or magnetic insertion devices. As an example magnetic insertion device consider the APPLE-II undulators [2] at the SOLEIL light source which have $N = 21$ permanent magnetic periods of length $\lambda_u = 80\ mm$ and field strength $0.8\ T$. Undulators of the same design are used at the Helmholtz Centre Berlin for Materials and Energy. A diagram is shown in Fig. 2.3 [100]. This is an advanced undulator design allowing control of the magnetic field in two transverse dimensions allowing for controllable polarization.

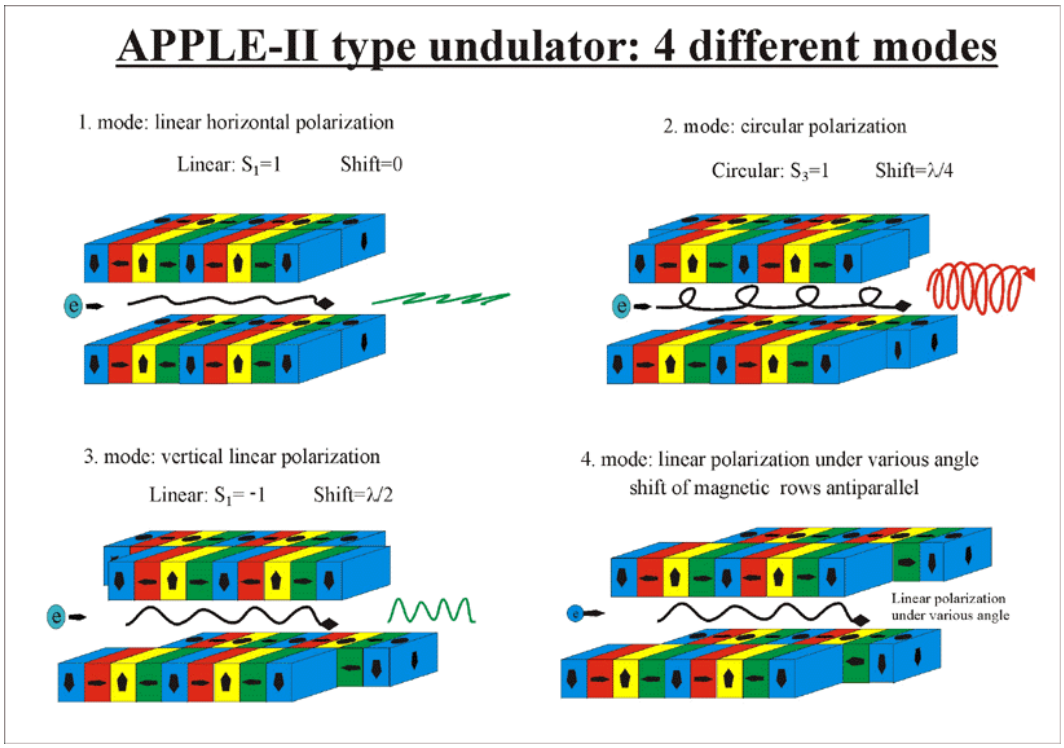

Figure 2.3: The APPLE II undulator. Arrangement of the rows of magnets for different polarizations (period length of the UE46: 46 mm) Helmholtz Centre Berlin for Materials and Energy

An electron entering such a device with velocity v will see the device as Lorentz contracted with contraction factor $\gamma = 1/\sqrt{(1 - v^2/c^2)}$ and will oscillate in the magnetic field, generating electromagnetic dipole radiation with characteristic wavelength λ_u/γ and higher harmonics in its own frame of reference. In the laboratory frame, a detector in front of the radiating electron will see the radiation as Doppler shifted to higher frequency with maximum shift detected exactly in the forward direction of the electron. As the electron oscillates transversely to its propagation direction, the relativistic factor in the direction of propagation is effectively diminished, resulting in an additional correction to the detected radiation wavelength which depends on the strength parameter K which indicates the maximum transverse velocity and maximum off-axis angle of the electron along its oscillatory trajectory. The detected fundamental wavelength is

$$\lambda \approx \frac{\lambda_u}{2\gamma^2}\left(1 + \frac{K^2}{2} + \gamma^2\theta^2\right) \tag{2.28}$$

where $K = \frac{eB_0\lambda_u}{2\pi m_e c}$ for a magnetic insertion device with field $B_\perp = B_0 \cos 2\pi z/\lambda_u$ and θ is the small angle between observation and the electron's undeflected propagation direction. For $K \gg 1$, the radiation source is said to be in the wiggler regime, in which case the harmonics form a quasi-continuous "synchrotron" spectrum. However, for the case $K \ll 1$, the radiation source is said to be in the undulator regime, in which case the harmonics remain discrete. For the APPLE II undulator, $K = 6$ and $\lambda_0 = 26\ nm\ (47eV)$ with a spectrum up to $\sim 2\ keV$.

A derivation of this formula can be found in Ref. [101], which further derives the radiated power within a cone of half-angle $\theta = \sqrt{1 + K^2/2}/\gamma\sqrt{N}$ from an electron beam current I_e to be

$$P_{cone} \approx \frac{\pi e\gamma^2 I_e}{\varepsilon_0 \lambda_u} \frac{K^2}{(1 + K^2/2)^2} \tag{2.29}$$

which is valid for $K \leq 1$.

LWFA beams have been injected into an insertion device [102, 103], generating infrared and soft x-ray radiation, effectively replacing a small Linac in a conventional synchrotron facility. However, synchrotron radiation can be generated by the motion of a LWFA beam in the accelerator structure itself. The strong radial fields in plasma waves, particularly in the bubble regime, can cause strong betatron motion of trapped particles. Betatron radiation in a wakefield bubble is more complicated than in a conventional undulator because the electrons are continuing to gain longitudinal momentum while they are emitting betatron radiation. Additionally, the electrons may catch up to the laser and experience betatron motion induced by the laser itself. Betatron motion has been studied theoretically in an ion channel or bubble [104–110], has been inferred experimentally [111–113], and the betatron radiation itself has been measured experimentally [114–117]. This radiation source is exciting because the relevant spatial scale is the betatron length $\lambda_{betatron} \approx \lambda_p\sqrt{2\gamma}$ rather than the spacing of a physical undulator magnet which is limited by manufacturing capabilities to several millimeters. γ in these equations is the relativistic Lorentz factor of wakefield accelerated electrons. The wavelength of betatron radiation in the lab frame is

$$\lambda_{LWFA\beta} \approx \frac{\sqrt{2}\pi c}{\gamma^{3/2}\omega_p} \tag{2.30}$$

and the strength parameter $K_\beta = \sqrt{2\gamma}\pi r_0/\lambda_p$ where r_0 is the spatial amplitude of the betatron motion. The spectrum in this case is expected to be synchrotron-like, including photon energies between the fundamental up to the critical energy:

$$\hbar\frac{2\pi c}{\lambda_{LWFA\beta}} \leq E_{LWFA\beta} \leq E_c = \frac{6\pi^2\hbar\gamma^3 c r_0}{\lambda_\beta^2} \tag{2.31}$$

The electron energy required for $\lambda_{LWFA\beta} = 26\ nm$ (same fundamental wavelength as the APPLE II undulator example above) operated at $n_e = 5 \times 10^{18}\ cm^{-3}$ is 27 MeV, which is easily achieved in a LWFA and compares with the 2.75 GeV beam used at

Soleil. A LWFA betatron wiggler with $K = 6$ operated at $n_e = 5 \times 10^{18}\ cm^{-3}$ and electron beam energy 270 MeV would have critical energy $E_c = 6.2\ keV$.

CHAPTER III

Methods

3.1 Experimental Facilities, Setup, and Procedures

All experiments discussed in this dissertation were conducted using the gas target facilities of the High Field Science research group at the University of Michigan Center for Ultrafast Optical Science [118]. This research group has exclusive use of the HERCULES laser, various pulsed and continuous wave lasers, a wide range of optics, stages, and manipulators, a stainless steel vacuum experiment chamber with all necessary roughing and turbomolecular pumps, and radiation shielding walls.

3.1.1 Laser Design and Delivery

The HERCULES laser system [119–121] began construction in 2002. The laser was upgraded to its current operating conditions during the fall of 2007 with the addition of the 100 TW stage amplifier and new compressor chamber. HERCULES is a CPA laser [122] which uses titanium doped sapphire (Ti:S) as the laser medium. CPA is the leading technology for generating sub-picosecond, high peak power laser pulses. The large gain bandwidth of Ti:S is employed. Large bandwidth is a requirement for short pulse generation (the product of Full Width at Half Maximum (FWHM) pulse duration and FWHM pulse bandwidth, or time-bandwidth product, has a minimum achievable value, 0.44 for a pulse with Gaussian temporal shape) but also allows the

pulse to be stretched greatly in time ("chirped") with the intentional introduction of dispersive optical elements, allowing for more energy to be added during amplification without exceeding the power for catastrophic self-focusing.

The HERCULES Ti:S pulse begins from a commercial Kerr-Lens Modelocking (KLM) laser (Femtolasers, GmbH) which is pumped by a Spectra-Physics Millenia neodymium doped yttrium aluminum garnet (Nd:YAG) laser. The KLM oscillator generates 12 fs pulses with 0.5 nJ pulse energy and 75 MHz repetition rate. Individual pulses are selected at 10 Hz. The pulses are then amplified 100-fold in a two-pass amplifier. The Amplified Spontaneous Emission (ASE) introduced by this amplification can be removed from the pulse using the Cross-Polarized Wave (XPW) technique [123], which is a 3rd-order nonlinear process. The XPW consists of two BaF_2 crystals and a Glan polarizer. Nonlinear processes in the crystals lead to polarization rotation and induced polarization ellipticity, and the Glan polarizer selects only the component which is cross-polarized to the original polarization. The process theoretically cleans the laser pulse according to the third power of the temporal shape. However, the actual cleaning capability is limited by the extinction ratio of the polarizer, and the transmission is of order 10%. Use of the XPW setup is optional, and it was not used for data in this thesis except when noted. The pulse is stretched to $\sim$ 500 ps by adding chirp, or wavelength dependent delay, with 4 diffraction grating reflections using two gratings and a rooftop mirror [124]. The pulse then enters a regenerative amplifier loop where it circulates many tens of times, achieving gain with each pass. The pulse is ejected from the cavity using a Pockels cell then sent to a 4-pass amplifier (10 TW), then 2-pass amplifier (30 TW), and the final 2-pass amplifier (300 TW). These last two amplifiers share a Neodymium:Glass pump laser which is split into 6 total pump beams which are each individually amplified and frequency-doubled. Each stage of the laser is protected with one or more of the following: spatial filter, Faraday isolator, and/or Pockels' cell. After the final amplification stage, the beam

Central wavelength	800 nm
Bandwidth	45 nm
Repetition rate	0.1 Hz
Minimum pulse duration	30 fs
Total pump energy (green)	50 J
Total IR energy (post-compressor)	9 J
Maximum IR power	300 TW
ASE contrast without XPW	10^{-8}
ASE contrast with XPW	10^{-11}
Picosecond-scale contrast	10^{-6}

Table 3.1: HERCULES laser specifications

is expanded from 5 cm to 15 cm before entering the compressor. The compressor consists of four reflective holographic gratings sized between 20 and 40 cm and a final reflective telescope bringing the beam down to 10 cm. The entire system is designed to compensate for the accumulated phase up to fifth order.

A schematic of HERCULES is shown in Fig. 3.1. The laser capabilities are summarized in Table 3.1

The laser is delivered to one of two experimental chambers- the one discussed in this dissertation, which is optimal for conducting high $f/\#$ experiments (Gas Target Chamber), or a more compact chamber used for ultrahigh intensity, enhanced contrast experiments (Solid Target Chamber). The laser is polarized in the horizontal plane, but can be flipped to the vertical plane using an *in-situ*-insertable $\lambda/2$ waveplate. A mirror on a 150 mm motorized stage allows switching between the chambers while under vacuum. Additionally, a portion of the uncompressed pulse from the 30 TW stage can be directed to a second compressor which can deliver a second high power short pulse to the gas target chamber if desired. The beam is transported primarily using 7″ dielectric-coated mirrors. For some experiments discussed, a deformable mirror was used (Xinetics). This special mirror consists of 177 piezoelectrically actuated regions behind a thin flexible mirror. The regions can be individually moved along the laser propagation axis using piezoelectric actuators. This is used to correct for the

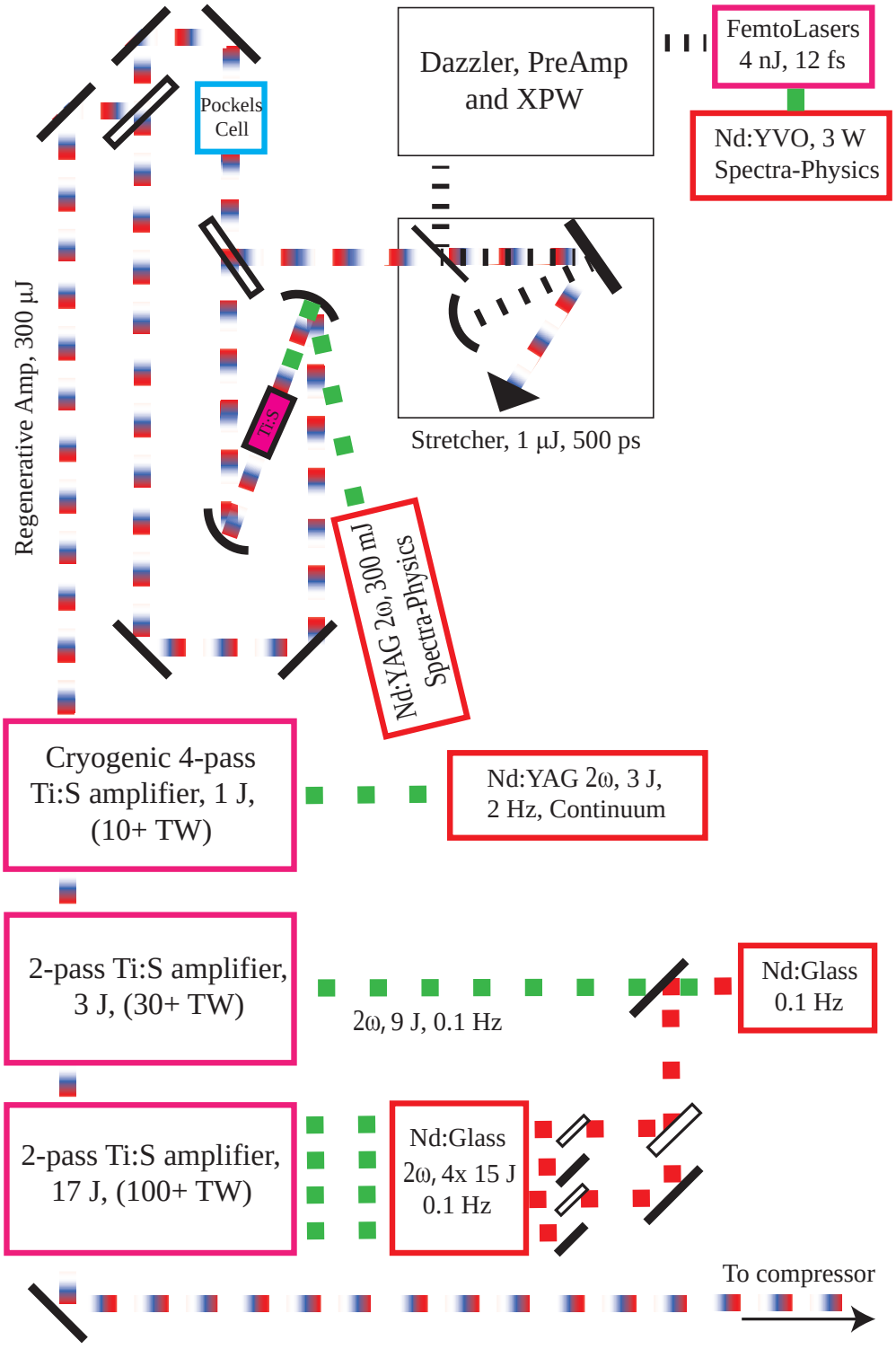

Figure 3.1: Schematic of the 300 *TW* HERCULES laser including FemtoLaser oscillator, regenerative amplifier, and three multipass amplifiers.

differing amount of phase accumulation at different regions of the beam profile and allows for a high-quality nearly diffraction-limited focal spot. An algorithm is used to optimize the flatness of the wavefronts as they are incident on the final focusing optic, allowing for a nearly ideal focal spot. The focusing optic for most experiments discussed was a $4''$ diameter $f = 1\ m, 5.5^{\circ}$ off-axis paraboloidal mirror.

3.1.2 Laser Diagnostics

On each shot, images of the pump beam or amplified beam spatial profile (near-field) can be captured after the 30 TW and 300 TW stages. The fluence of these images can be integrated for use as a relative measurement of the single-shot energies. Before each experimental series, an absolute energy measurement is made by placing a large area calorimeter in the near-field of the beam after the final telescope before the compressor. A large area diode measures the transmitted light through the last mirror before this position as a redundant energy diagnostic. The transmission of all optics between the measurement position and the final focused beam was measured. Additionally, the near-field beam profile of the amplified beam has been studied by placing burn paper in the beam near the experimental chamber entrance.

A third-order autocorrelator was used to diagnose and optimize the laser upon installation of the new compressor. This measurement requires substantial setup as well as removal of a window on the compressor. For simplicity the laser spectrum, rather than the autocorrelation, is checked daily to look for any bandwidth losses or spatial variation across the beam. In the event of replacement or upgrade of any optics in HERCULES, the pulse duration is checked using a single-shot second-order autocorrelator. The autocorrelator allows an objective determination of optimum grating separation in the compressor. A grating separation scan is demonstrated in Fig. 3.2, where red squares plot the measured pulse duration in air (open squares) and vacuum (closed), taking into account the dispersion introduced by a 7 mm BK7

lens. A single shot autocorrelation trace is shown inset. Additionally, the autocorrelator has been used to evaluate the sub-ps pulse risetime and search for possible prepulses. The autocorrelator was setup to take pulse duration measurements after transmission through the entire experimental setup at full power. This is a very difficult measurement to take since the fluence on the crystal must be kept below the damage threshold at full power without the use of material filters while the autocorrelator alignment must be performed with 4 orders of magnitude less power. The best method which could practically be achieved still required propagation through 6 mm of fused silica and 11 mm of glass. The measured pulse durations in vacuum at alignment level and at 71 TW are shown in Fig. 3.3. The measured durations are 66 and 63 fs, respectively before taking into account stretching by the glass. An unchirped 30 fs pulse propagating through 11 mm of BK7 glass would stretch to 60 fs. Although this glass obfuscates the measurement, the similarity between the two curves suggests gain narrowing in the amplifiers is insubstantial.

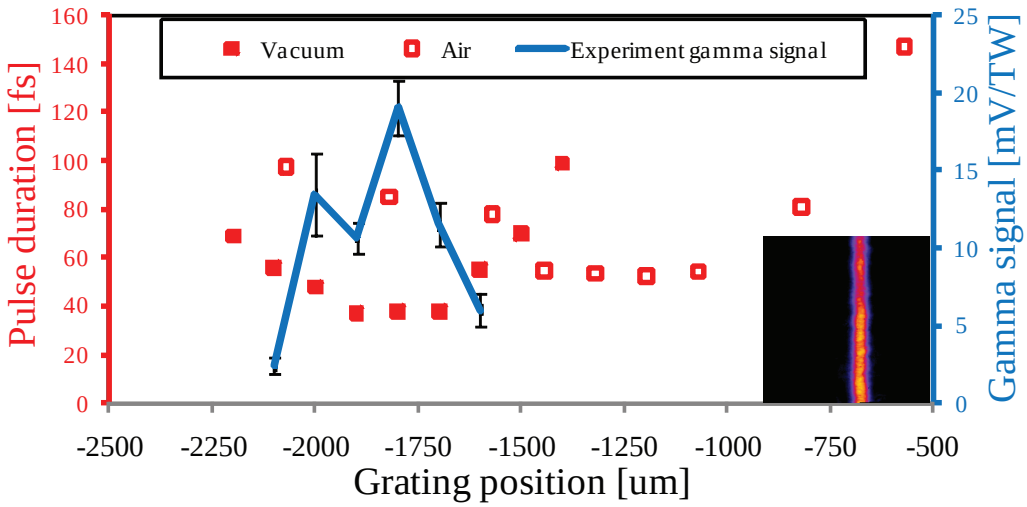

Figure 3.2: Grating scan conducted with the 2nd-order autocorrelator at alignment laser power. Also shown (blue line) are experimental data demonstrating optimization of grating postion using the measured gamma signal generated from high energy electrons. A single trace is shown inset with temporal x-axis and spatial y-axis.

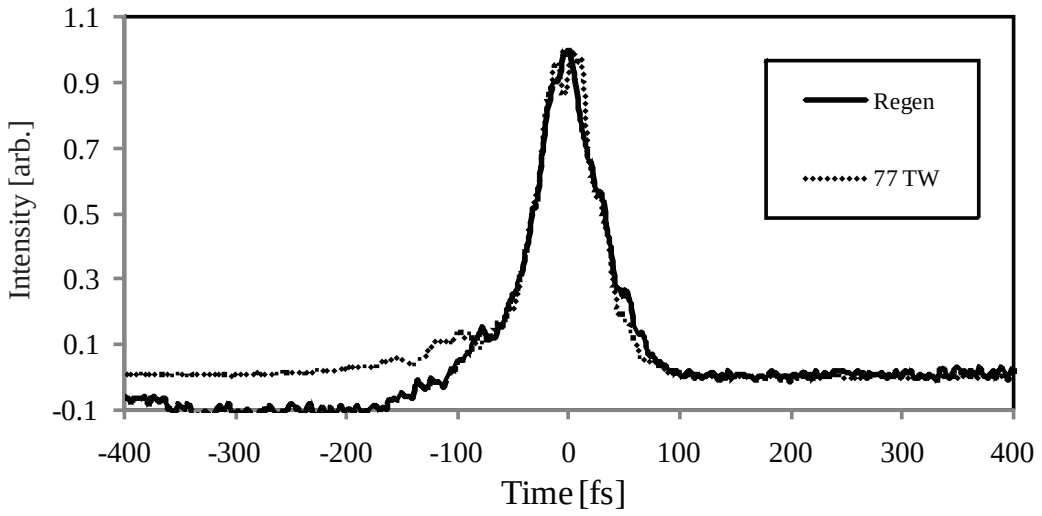

Figure 3.3: 2nd-order autocorrelator traces at regenerative amplifier level and at 71 TW. Stretching introduced by 15 mm of glass is not taken into account. The difference on the left-side wing of the curves is due to background from a single arm of the autocorrelator.

The focal spot of the laser in $f/10$ focusing geometry is shown in Fig. 3.4. This image was taken using a 10x microscope objective and a 10-bit CCD, which cannot be used in vacuum. The focal spot has diameter $11.9 \times 11.9 \pm 0.5$ μm FWHM with 23% of the energy contained within the FWHM. The beam waist w_0, or radius at which intensity has dropped off by a factor of $1/e^2$, is 11.4 μm. The "M-squared (M^2)" value is a measure of the ability to focus a given laser beam. M^2 is defined as the ratio of the beam parameter product (BPP) of a focusing system to the ideal BPP where BPP is the product of the beam waist and the half angle of the beam divergence. The ideal BPP for a Gaussian beam profile is λ_0/π. All real laser setups have $M^2 > 1$. For this focusing setup $M^2 = 2.24$. In $f/20$ focusing geometry, $w_0 = 24 \times 24 \pm 1$ μm and $M^2 = 2.4$. A vacuum-compatible 8-bit CCD is used instead to compare the spot under vacuum. An 8-bit image is observed daily to ensure the focal spot is not perturbed and that the full power is reaching the target.

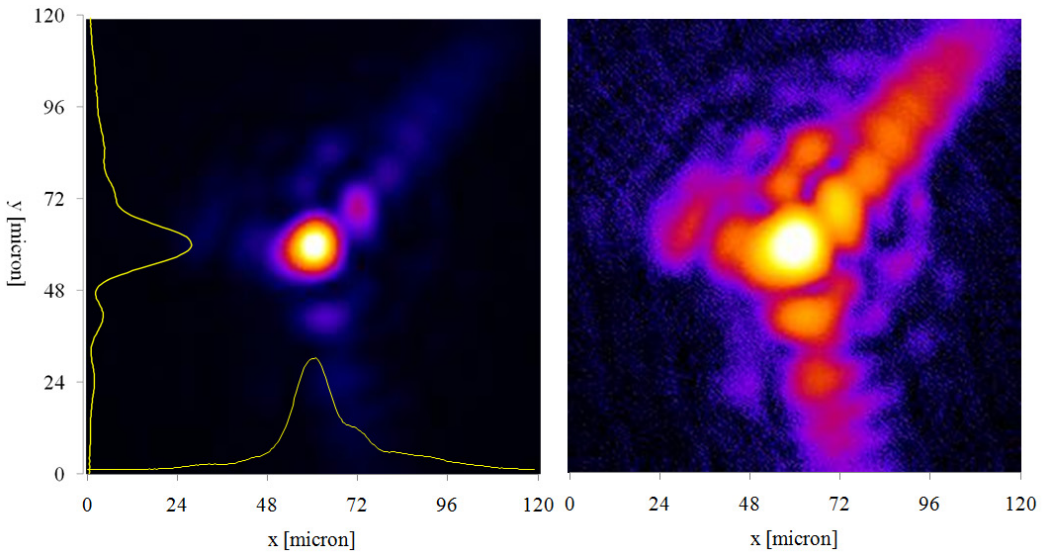

Figure 3.4: Focal spot on linear (left) and logarithmic scales (right) taken with 10-bit CCD

3.1.3 Interaction Diagnostics

The diagnostics fielded on nearly all these gas target experiments include a transverse optical probe line with delay stage for illuminating the interaction, scattered light imaging systems for collecting light emanating from the interaction in the transverse directions, organic or inorganic scintillators + photomultiplier tubes for detecting radiation indicative of the laser/plasma interaction, and Fujifilm Image Plate (IP) and Kodak LANEX phosphorescent screens (terbium activated gadolinium oxysulfide) for detection of electrons. The sensitivities of these two detector types have been documented in Refs. [125] and [126], respectively.

The transverse probe originates from a $\sim$ 1 % reflection of the main pulse using a 2 μm thick 6" diameter pellicle (stretched nitrocellulose, National Photocolor, Inc.). The probe optical path includes several 2" diameter silver coated mirrors, including two on a delay stage which is motorized with temporal range of 333 ps with 30 fs repeatability and manually controllable with 1 ns range and 1 ps repeatability. The limiting aperture is one of these 2" mirrors at 45° incidence, with the remainder of

the beam being dumped. The probe has pulse duration 30 fs- shorter than typical time scales for plasma ion hydrodynamic evolution. The probe was made transverse to the main pulse axis with 250 μrad precision using a right angle prism. The probe arrives at the main pulse axis as a plane wave, meaning that the delay between main pulse transit and probe time is a function of position along the main pulse axis.

The vertical plane located at the main pulse axis with normal in the probe axis is imaged using a two lens system with magnification chosen depending on the length of interaction under investigation. The system is sketched in Fig. 3.5. The light is sent into a two arm shearing interferometer. Because the probe beam is much larger than the interaction region, the beam can be split with a beamsplitter and a region of the beam which traversed the plasma can be overlapped with a region which did not. When the pulses of the two arms are overlapped temporally and spatially on a CCD, interference fringes are generated. Light that traverses the plasma accumulates a phase shift relative to light that did not traverse the plasma of

$$\Delta\phi(y,z) = \frac{2\pi}{\lambda}\int_{-x_p}^{x_p}[1-\eta(x,y,z)]dx \tag{3.1}$$

where the full extent of the plasma is bound within $-x_p < x < x_p$. This causes displacement of the interference fringes on the detector plane (Fig. 3.6. This projection of phase can be used to determine the plasma density in three dimensions, with the assumption that the plasma is cylindrically symmetrical, through the Abel inversion function,

$$\Delta\phi(r,z) = -\frac{1}{\pi}\int_{r=0}^{\infty}\frac{\Delta\phi(y,z)}{dy}\frac{dy}{\sqrt{y^2-r^2}} \tag{3.2}$$

where $r^2 = x^2 + y^2$. Abel inversion and the calculation of electron densities were conducted using a program written by Nicholas Matlis using Labview software [127].

Alternatively, the reference arm of the interferometer can be blocked, providing

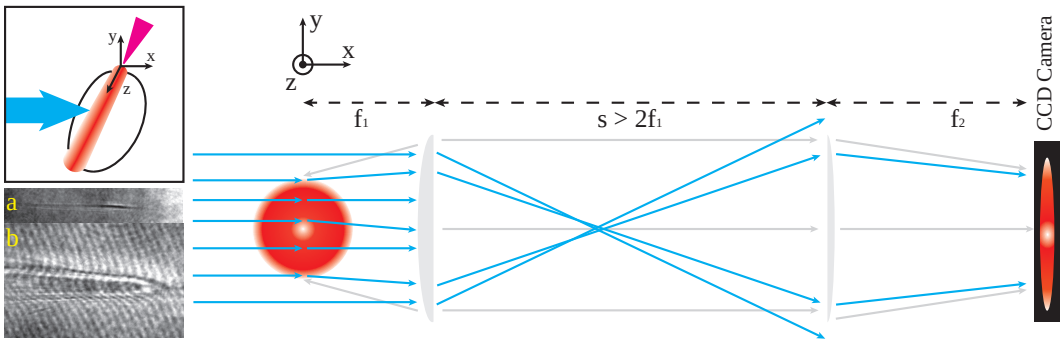

Figure 3.5: Sketch of the imaging system used for interferometry or shadowgraphy. The collection lens is $2''$ in diameter with focal length $f_1 = 20, 30,$ or $50\ cm$. The imaging lens is separated from the collection lens by $s \sim 120 - 150\ cm$ and has $\geq 3''$ diameter and $f_2 = 30$ or $50\ cm$. Scales are exagerated in this sketch. The probe beam illuminates a semi-elliptical region wider than $2\ cm$ (much larger than the plasma region shown in red). However, the separation between the collection and imaging lenses results in lost field of view and spatial resolution.

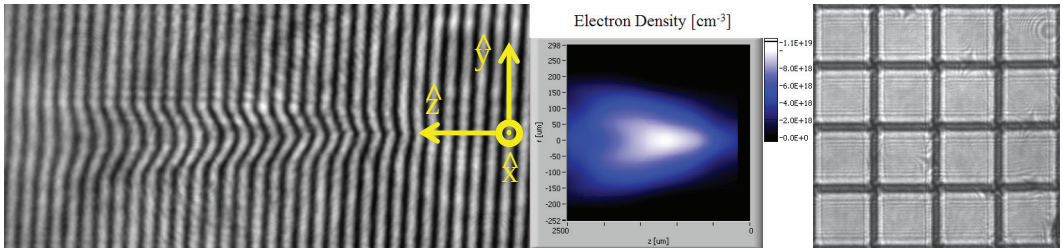

Figure 3.6: Raw interferogram (left), electron density profile inferred by Abel inversion (middle), and shadowgram with a 90 span-per-inch metal mesh in the plane $x = 0$ (right).

a clear shadowgram of the interaction. An example shadowgram is shown in 3.6, exhibiting a resolution finer than 20 μm. The term shadowgram in this thesis is used liberally. A pure shadowgram is a recording of the near-field of the direct shadow of an object with refractive index inhomogeneities. Using the same coordinate system as the previous section, probe rays propagating in the $\hat{x}$ direction are deflected by gradients of the refractive index according to [128]:

$$\frac{\partial^2 \perp}{\partial x^2} = \frac{1}{\eta}\frac{\partial \eta}{\partial \perp} \tag{3.3}$$

where $\perp$ represents a coordinate transverse to the probe propagation direction. In the experiments in this thesis, the object being probed is a conical plasma aligned along the z axis, corresponding to the volume over which the laser intensity is high enough to fully ionize the gas. An idealized plasma is sharp-walled and has constant density within the cone. In reality, ionization is not a threshold phenomenon so the walls have finite ramp width, resulting in very weak refractive index gradients in the z axis and stronger gradients in the x and y axes. This leads to probe ray deflection primarily in the y direction. Rays propagating through the plasma are deflected by an angle

$$\delta\theta_y = \frac{1}{\eta}\int \frac{\partial \eta}{\partial y} dx \tag{3.4}$$

where the integral is taken over the width of the plasma volume. The deflection is toward the region of higher refractive index. For a conical, constant density plasma, gradients at the edge of the plasma cause probe rays to deflect away from the plasma. This effect is observed in Fig. 3.5a, which is the shadowgram of a simple, high density plasma produced with laser intensity $\sim 10^{16}\ Wcm^{-2}$. Probe light is displaced in the shadow of the plasma and a faint halo is observed outside the plasma. The imaging system used typically is chosen to have spatial magnification $M_s > 1$. The object plane is set to the laser axis by shadowgraphy of a simple plasma generated

in air using HERCULES operating at alignment power. This procedure is crucial, as improper focusing leads to observation of a diffraction pattern at the cone edge. Using higher laser intensity and a high density helium target, the cone from each of the two ionization states is visible in Fig. 3.5b, where two layers of the shadow and halo feature are visible. The vertical ionization front is also visible in many shots at the exit of the plume or at the position of the main pulse within the plume. These features are typically not visible at the densities of interest for optimized wakefield acceleration.

Another effect observed in some shadowgrams taken at full power is a bright streak on-axis. This streak is caused by plasma channeling by the high intensity pulse. As discussed in Sec. 2.2.3, the main pulse can experience self-focusing and beam filamentation when the power is greater than the critical power. High intensity laser filaments can produce channels of decreased electron density which may persist for many plasma periods and may even cause significant ion motion on a longer timescale. In the case of ion motion, electrons will adjust to match the ion distribution on the timescale of $1/\omega_e$. Therefore the index of refraction distribution will be determined by the ion distribution. These structures cause probe ray deflection in the opposite direction from the simple conical plasma case- probe light is focused. Interpretation of shadowgrams exhibiting these features is complicated, as mild focusing will lead to observation of a bright streak, whereas severe focusing could lead to observation of a depleted region. Additionally, filamented channels have been observed to exit the original plasma cone and cause a streak of ionization. Focusing of the image system is also crucial for observation of these fine structures in the plasma.

As an estimate of the expected deflection angle from a plasma relevant to this thesis, consider the refractive index gradient from the edge of a full plasma cone. Supposing the electron density falls from 5×10^{18} to 0 cm^{-3} over a distance of 100 μm, the deflection angle for a ray passing through the edge of a plasma cone where the cone

radius is 150 μm predicted from Eq. 3.4 is ~ 3 $mrad$. For the lenses typically used for the shadowgraphy setup, this corresponds to a displacement of rays of ~ 1 mm on the CCD chip- a sizeable portion of the field of view. The deflection is much less severe for rays that traverse the cone close to the cone axis, which see a much shallower gradient in the y axis. Further, for the case of ray deflection by a partially depleted filamentation channel, the ray displacement on the CCD will be smaller than the value calculated above (1 mm) by approximately a factor $\delta n/n_0$. As this would suggest, on-axis streaks tend to be observed with low density, high intensity experimental conditions, whereas the on-axis feature becomes more complicated at high density as gradients become stronger.

Another diagnostic fielded on most experiments is topscatter imaging. The scattered light is collected from above with a 2", $f = 30$ cm lens, sent out of the chamber via periscope and divided with a broad band 50 % beamsplitter. One arm is reimaged with a $f = 50$ cm lens onto a CCD which is exposed for 100 ms, collecting all scattered laser light and plasma emission. The other arm is reimaged with a $f = 100$ cm lens onto a slit of an imaging spectrometer, such that the main pulse axis is imaged to be parallel to the slit length. Side-scattered light can be used to confirm alignment and when spectrally resolved can be used to diagnose the density (Sec. 4.3.1), laser evolution [129], and injection [130].

IP is chosen for electron or x-ray measurements for which sensitivity and high contrast (16-bit Fujifilm BAS-1000 II reader) are required. In all cases, the IP is first erased by illuminating it with ultraviolet light for 30 minutes and is then placed inside the vacuum chamber for exposure and must be removed to be read. Exposure by x-rays or energetic electrons excites electrons within the IP lattice (a BaFBr:Eu^{2+} crystal) into the conduction band, and some such electrons become trapped in a metastable state with a lifetime of several hours at room temperature. The exposed IP must be fully light-shielded to prevent erasure before being read. The Fujifilm

reader scans a red laser over the entire surface of the IP in 5 μm steps, again exciting electrons in the metastable state and leading to Photostimulated luminescence (PSL), which is detected with a photomultiplier tube and the signal is digitized.

LANEX is used instead when electron information is needed instantly on each single shot. The LANEX screens are protected on the exposure side by 500 μm thick aluminum or brass to prevent overexposure from low energy electrons and soft x-rays and are also carefully light-shielded to prevent laser light transmission. The screen is imaged from the rear side using a telephoto lens and filtered with BG39 glass. The emission is centered on a narrow line at 550 nm. Two grades have been used in these experiments- LANEX regular and LANEX fine.

The electron spectrum is measured by dispersion in a transverse magnetic field whereby electrons obey a bent trajectory with curvature according to the relativistic Larmor radius, $r_L = p_\gamma / eB$ where $p_\gamma = \gamma m_e v$. The most dispersive magnet used in these experiments is 15 cm in the beam forward direction and 10 cm wide with a field strength of 8.0 ± 0.5 kG sustained over 11 cm and falling off over 3 cm. After leaving the magnetic field, the electrons propagate freely to the detector.

All images for LANEX measurements, transverse probe, and scattered light are acquired with Photometrics Coolsnap cf monochrome CCDs, which have specifications listed in Table 3.2. For several of the experimental setups described in this thesis, an absolute charge calibration of the electron spectrometer diagnostic was conducted. This was achieved by placing an image plate between the LANEX screen and its usual shielding, and correlating the measured LANEX screen to IP signal, which is absolutely calibrated to electron charge as a function of energy as described in Ref. [125].

Additional diagnostics are available, as needed, for certain experiments including two Jobin Yvon motorized spectrometers for measurement of the transmitted or scattered light, neutron time-of-flight detectors, CR39 particle track detectors, and

Pixels	1392×1040
Pixel size	$4.95 \times 4.95\ \mu m$
Chip size	$6.5 \times 4.8\ mm$
Readout	$11 frames/s$
A/D	$12 - bit$
readout noise	4.3 *counts* (Standard Deviation)
Quantum efficiency	$> 5\%$ $(400 - 800\ nm)$

Table 3.2: Coolsnap cf monochrome CCD specifications

integrating current transformers.

3.2 Computational Modeling

Many aspects of LWFA-relevant systems can be modeled using PIC codes. PIC codes represent plasma as a collection of N charged quasiparticles, each quasiparticle representing one or many charges in a real plasma. The computational advantage of a PIC code comes from realizing that the acceleration on any particle in a plasma is dominated by the macroscopic electromagnetic fields. Thus the total acceleration on a particle can be calculated using an estimate of the local macroscopic fields rather than by calculating the net Coulombic acceleration from all other $N - 1$ particles. A PIC algorithm must include a particle pusher which time-integrates the Lorentz force equation and a field solver which finds the electric and magnetic fields for the entire spatial domain. An artificial spatial grid is established to numerically calculate the electric and magnetic fields at any point in the spatial domain. Any PIC model should choose a grid which resolves the Debye length of the system in order to minimize artificial particle heating, though for PIC modeling of LWFA, the more constraining spatial scale is the laser wavelength. Finite differences are used for the particle pusher and field solvers. To accomplish stability, these two steps are performed iteratively with both steps performed at each time step.

The PIC code OSIRIS [131, 132] was used to guide choices of experimental pa-

rameters and PICNIC [133], which includes an ADK ionization model, was used in support of the experimental results discussed in Sec. 7.5.

CHAPTER IV

Acceleration in Gas Jets

This chapter will incorporate data from several experiments, giving an overview of my findings in laser wakefield acceleration using gas jets as the accelerator medium.

4.1 Introduction

The most commonly used accelerator device for LWFA is the gas jet, whereby the gas from a reservoir is released in a brief pulse and caused to expand supersonically using a conical nozzle. Conical nozzles are typically used as opposed to the ideal *de Laval* nozzles used in rocketry due to ease of manufacturing. The suitability of conical nozzles for LWFA was studied in Ref. [134].

For the laser parameters considered here, the main laser pulse intensity is 4-5 orders of magnitude greater than the ionization threshold for hydrogen or helium. Diatomic hydrogen and atomic helium will become fully ionized at least 2 pulse lengths in advance of the HERCULES pulse, assuming a Gaussian with 30 fs FWHM, and could even be ionized much earlier in the presence of a high intensity prepulse. Therefore, these two gases are the most common species used in LWFA due to a desire to produce well-understood plasmas, with helium being the most common due to the flammability of hydrogen.

4.2 Experimental Setup and Calculations

A typical experimental setup is shown in Fig. 4.1. The inner chamber dimensions outlined in the figure are 155 $\times$ 94 cm. All experiments were conducted at vacuum pressure $< 5 \times 10^{-4}$ $Torr$ which is achieved using turbomolecular pumps. The system can be aligned under vacuum using two motorized mirrors, correcting for small displacements of optical components during pumping.

Supersonic expansion of the gas sets up a sharp vacuum/gas interface and can produce a flat density profile. Driving supersonic gas expansion from the nozzle requires high backing pressure (as much as 1500 PSI), which is pulsed using an industrial solenoid valve (Peter Paul EH22H7DCCMG). A custom voltage pulser allowed control of the amplitude and duration of the > 100 V pulse required to drive the valve. The valve opening time was 5 ms and the gas flow was stable throughout a 20 ms window. The laser arrived 15 ms after a trigger pulse which simultaneously triggered the voltage pulser and opened all diagnostic shutters. All nozzles used were machined from aluminum which can withstand the high pressure requirements, is easily machined and has relatively low Z which is important for reducing signal from bremsstrahlung radiation. Nozzles with larger exit diameter were used when long acceleration lengths were anticipated. However, the gas pressure required to produce a particular density increases with increasing nozzle diameter. The pressure required depends not only on the diameter, but also on the Mach number of the nozzle, which is sensitive to the geometry of the nozzle. The experimental repetition rate is generally limited by the time required to pump out the chamber (as much as 3 min) rather than the laser repetition rate. The open duration of the solenoid valve can be shortened to reduce the pumping time. The nozzle was placed 1 mm below the laser axis for all experiments. The gas plume is still sharply defined at this height above the nozzle, but the interface and density profile become smoothed out several mm above the nozzle. If the nozzle were raised closer to the laser axis, bright laser

scatter became a concern for some diagnostics and the nozzle could potentially be damaged.

Unless it was deemed unnecessary, each experimental run began with a scan of the nozzle position followed by a grating scan, where either the electron signal or gamma ray signal was optimized. The high energy electron signal was found to disappear completely if the nozzle longitudinal position is off from optimum by two Rayleigh ranges, $2z_R$, where $z_R = \frac{\pi w_0^2}{M^2 \lambda_0} = (228, 960)\ \mu m$ for $(f/10, f/20)$ geometries or if the grating position is off by more than 200 μm ($\tau > 50\ fs$).

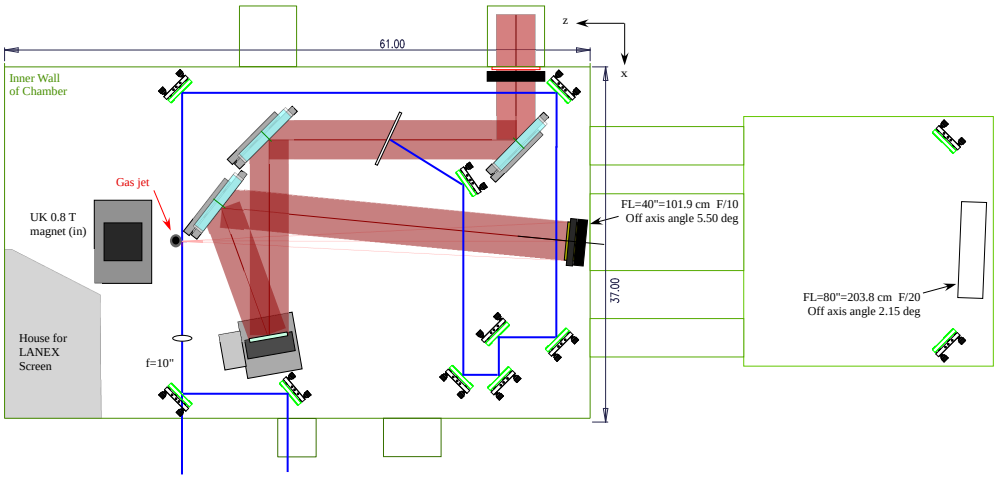

Figure 4.1: Gas jet experimental chamber setup.

Based on the laser parameters $P = 100\ TW, \tau = 30\ fs$, the "bubble" criteria (Eqs. 2.24,2.25) are exactly satisfied for a density $3.4 \times 10^{18}\ cm^{-3}$ and matched spotsize radius of 11 μm. This spotsize could be achieved exactly with $f/20$ focusing geometry. However, injection cannot be achieved at the density $3.4 \times 10^{18}\ cm^{-3}$ with this setup. Using $f/10$ focusing geometry increases the intensity, allowing injection at a lower density than $f/20$ geometry. The maximum energy gain for these parameters according to the bubble scaling by Lu $\Delta E[GeV] \cong 1.7 \left(\frac{P[TW]}{100}\right)^{1/3} \left(\frac{10^{18}}{n_p[cm^{-3}]}\right) \left(\frac{0.8}{\lambda_0[\mu m]}\right)^{4/3}$ [81] is 580 MeV. At 200 TW, injection at exactly matched conditions should be

achievable.

4.3 Experimental Results

4.3.1 Top and Side Scattering

The signal of scattered light detected in the top-scatter imaging system is very sensitive to laser intensity and plasma density. For these reasons it is used to confirm that each experiment is properly setup. The scattered light originates from the front of the plasma as shown in Fig. 4.2(a). To further investigate this scatter, a half-wave plate was installed, rotating the polarization axis to be inline with the observation direction which resulted in a decrease in the signal by more than 4 orders of magnitude. This strong directional dependence is consistent with both incoherent Thomson scattering by free electrons [135] and Raman scattering by plasma waves [136–138]. However, the Thomson scattering cross section is too low to explain the observed bright scatter (Equation 56 in [139] predicts scattered power $\sim 10^{-8}P$ where P is the laser power, whereas the detected signal suggests the value is $\sim 10^{-4}P$). When the scattered light was spectrally resolved, as shown in Fig. 4.2(b, c), it became clear that the light was Raman side-scattering [129], as the light was shifted from the initial laser wavelength to longer wavelength where the maximum shift $\Delta\lambda = 2\pi c/\omega_r$. This diagnostic is well-suited for plasma density measurement as the Raman shift records the relativistic plasma frequency precisely within the spot of the main pulse, which can be difficult to resolve with interferometry.

Additionally, sharp increase in the amount of measured light was found to indicate failure to inject. Fig. 4.3 shows the integrated Charge Coupled Device (CCD) counts from the top-scatter diagnostic as a function of beam charge as detected by the electron spectrometer. The data are 70 shots with experimental parameters held fixed and laser power ranging from $62 - 73\ TW$ where the range comes from shot-to-shot

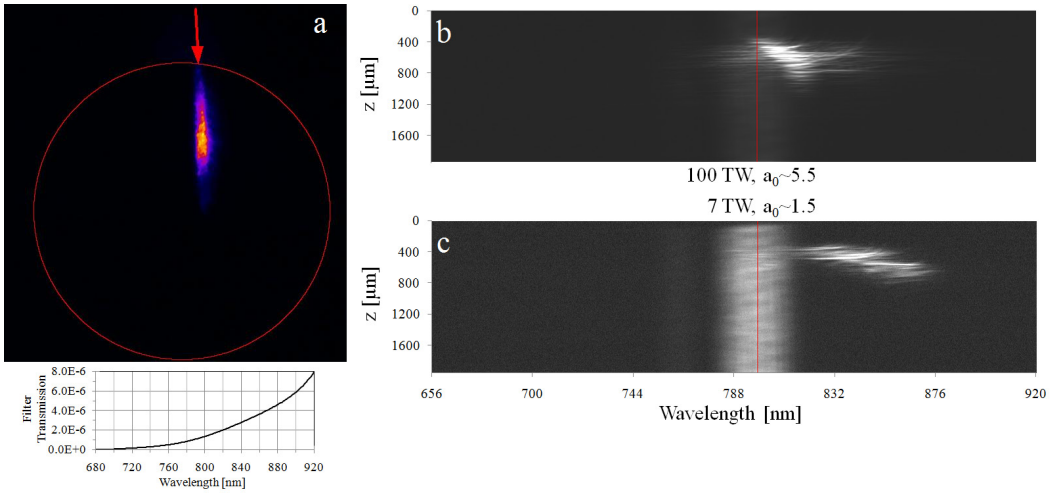

Figure 4.2: Raman-scattered light imaged (a) and spectrally resolved (b, c) as observed in the direction perpendicular to the laser polarization direction which is in the horizontal plane in (a) and vertical plane in (b, c). The laser propagates from top to bottom in each case. In (a), the 3 mm nozzle orifice, which is 1 mm below the laser plane, is shown as a red circle. In (b, c) the laser initial central wavelength 800 nm is indicated by the red line. The center band is from probe light, showing the laser spectrum. The bright streak is Raman-scattered to longer wavelength with shift dependent on $n_e(z)$ and $I(z)$.

fluctuation. The shots were placed in bins according to the detected charge (shown as horizontal bars) and the integrated top-scatter signal is averaged within each bin. Vertical error bars enclose one standard deviation for each bin. The transmission for the filters used in the top-scatter diagnostic (Fig. 4.2, bottom left) increases steeply as wavelength increases. Therefore, it cannot be determined whether the increased signal associated with low charge is due to a true increase in scattered light or a shift of the light to longer wavelength. Such a shift could be caused by a high stimulated Raman instability growth rate which might simultaneously explain the decrease in charge. Alternatively, if the increase in detected scattered light is not due to a wavelength shift, the amount of scattered light is truly greater which could indicate that the main laser becomes depleted more rapidly on the low charge shots.

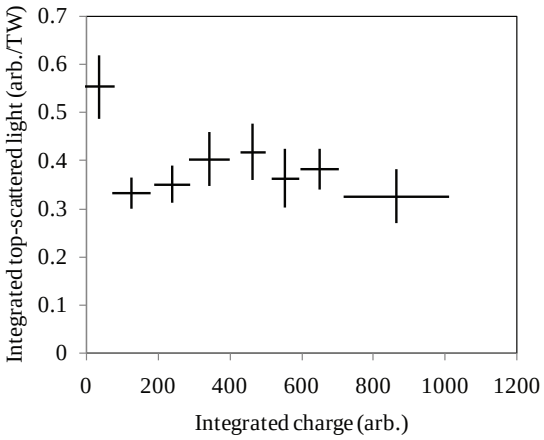

Figure 4.3: Comparison of collected top-scattered light vs. measured charge.

4.3.2 Electron Spectra and Profiles

Density is the most important experimental parameter with regard to electron spectrum, charge, maximum energy, and divergence. The general dependence of beam parameters on density is as follows:

- A density threshold, below which no high energy electrons are detected, though there may be lower energy electrons indicated by an increase in gamma ray signal

- Monoenergetic, single beam with stable, undeflected pointing, present for density just above threshold (bubble regime)

- As density is increased, the monoenergetic beam energy decreases and energy spread increases (dephasing, and forced LWFA regime)

- As density is further increased, beam charge increases, as does divergence. There may be multiple beams, accompanied with highly deflected and structured beams (wavebreaking)

- Onset of laser and/or beam instabilities at high density results in diminished beam energy and eventual failure to accelerate.

This behavior is demonstrated in Fig. 4.4, which plots the maximum detected energy for 318 shots where shots at identical pressures have been averaged. These data were taken with power 96 $TW \leq P \leq 136\ TW$ and a 10 mm nozzle. In this case, the acceleration length was most likely limited by the guiding length.

Fig. 4.5 shows the injection threshold density as a function of laser power on target. The threshold scales as $n_{inj} \propto P^{-0.8}$. The plotted injection threshold data points indicate the lowest density at which electrons were observed on the electron spectrometer. Densities are found using experimental fittings of density versus pressure.

Selected high energy and high charge shots are shown in Fig. 4.6, in which the electrons have been dispersed according to their energy in the horizontal axis. Energy increases to the left of the image with black vertical bars indicating 100, 200, 300, 400, and 500 MeV. The right edge corresponds to $58.7 \pm 0.8\ MeV$ and the left

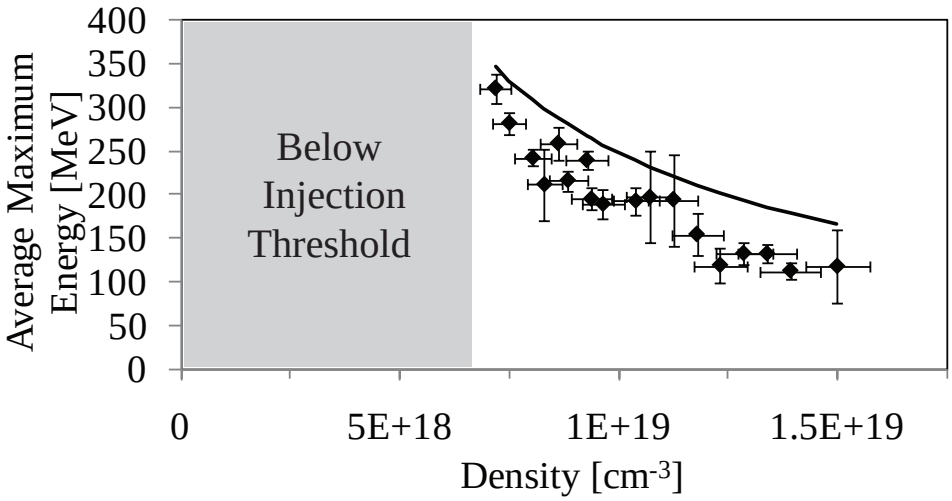

Figure 4.4: Maximum electron energy dependence on electron density. Data include 194 shots with a 10 mm nozzle and power $78 \leq P \leq 126\ TW$. Each data point plots the maximum electron energy averaged over shots taken at identical pressure and vertical error bars span one standard deviation of those shots. Also plotted as a solid line is the theoretical scaling $\Delta E \simeq \frac{2}{3} m_e c^2 \left(\frac{\omega_0}{\omega_p}\right)^2 a_0$ by W. Lu, see Sec. 8.1 for $a_0 = 4.2$.

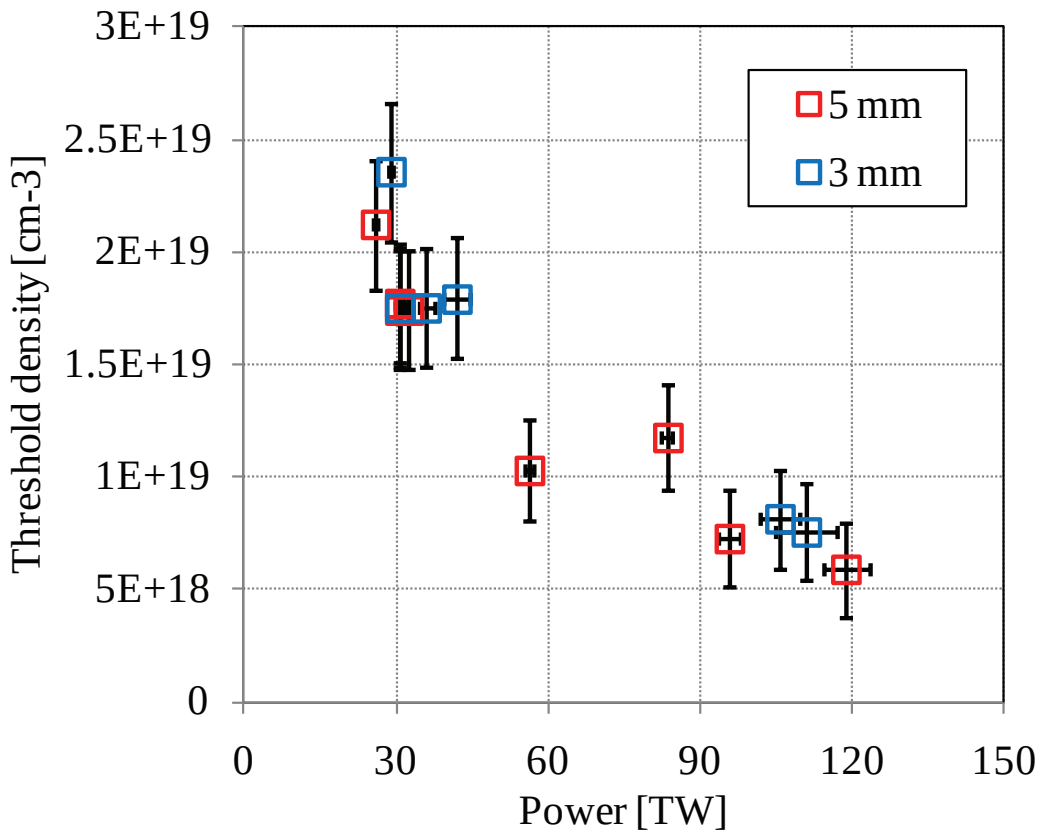

Figure 4.5: Injection threshold density dependence on power. The data come from 14 experimental runs in which the injection threshold was found to 10% accuracy or better including runs using 3 *mm* and 5 *mm* nozzles.

corresponds to 918 $\pm$ 155 MeV where the uncertainty is due to the beam divergence and pointing fluctuation which affects the entrance position and angle of the electron beam as it enters the spectrometer.

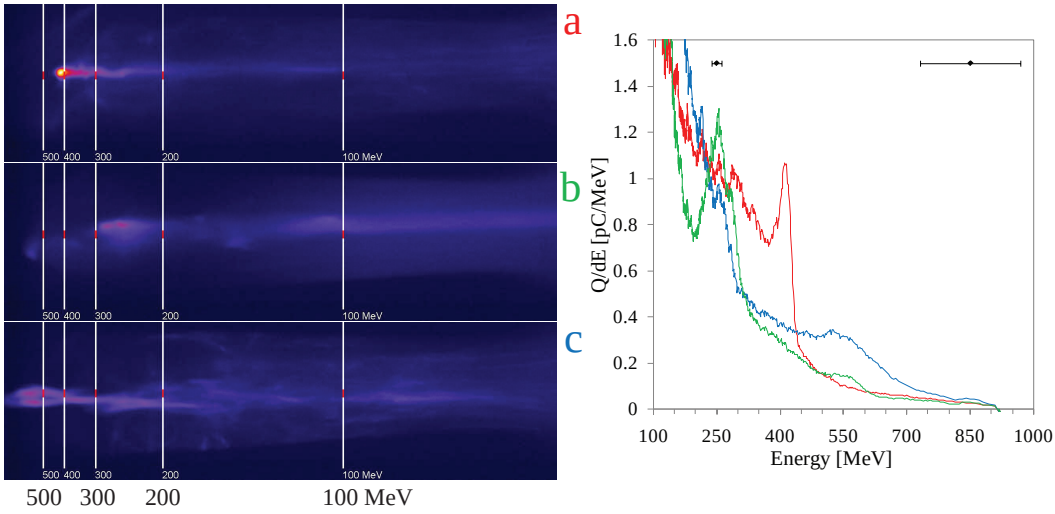

Figure 4.6: Three of the highest energy electron shots from an experiment using a 10 mm nozzle and 100 TW. Images of the lanex scintillator screen are shown (left) with energy increasing from right to left. White bars are marked at 100, 200, 300, 400, and 500 MeV and the red bar in the middle indicates 10 $mrad$ divergence at that location on the screen. Calibrated spectra for these shots are shown (right) with the uncertainty in energy shown as black error bars for energy of 250 and 850 MeV

Beams have been produced with as little as 1% energy spread ($\Delta E/E$) where ΔE is the FWHM of the peak in charge per unit energy. Some example beam spectra are shown in Fig. 4.7. The beam is not apertured before being dispersed by the magnet. Therefore beams detected as monoenergetic also necessarily have low divergence whereas lower energy features, such as beams injected in trailing buckets or a low energy tail, tend to have higher divergence.

It has been found through grating scans that an increase in pulse duration from just 30 to 50 fs entirely prevents the monoenergetic, high energy electrons associated with LWFA in the bubble regime. However, the behavior is only weakly dependent upon laser power. An increase in power allows injection at lower density, resulting in

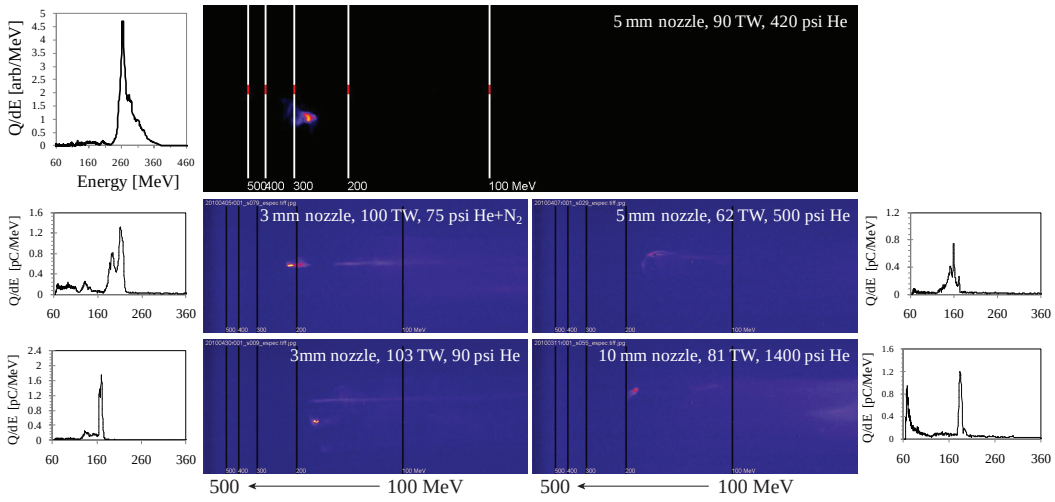

Figure 4.7: Five example spectra of monoenergetic electron shots produced at various experimental conditions.

higher maximum energy, though the overall beam behavior as a function of density is unchanged. The maximum beam charge also increases with power, though the increase given a doubling of laser power is not as large as the variation in beam charge for a scan of density over a factor of two at fixed power.

The beam parameters are also weakly dependent on focal spot quality. For this reason, it was decided that the deformable mirror, which was used for nearly a year, could be replaced with a flat gold mirror without detriment to the LWFA experiments.

4.3.3 Beam Filamentation and Channeling

The shadowgrams from the transverse probe show structures in the interaction region. For example, Fig. 4.8a features a bright strip on the laser axis surrounded by dark strips. This occurrence is due to displacement of plasma ions, producing a nonuniform but cylindrically symmetric ion channel with a matching electron distribution. This cylinder focuses probe light toward the axis of the main pulse. A single filament has been observed uniformly along the entire length of the main pulse interaction, indicative of a uniform ion channel. This channel existed at densities

appropriate for monoenergetic LWFA. As discussed in Ch. V, channels have been created intentionally with an additional laser for the purpose of laser guiding. At 100 TW and higher densities, multiple filaments have been observed. The fanned out filaments (Fig. 4.8c and d) were produced by laser light which was scattered by laser/plasma interactions. While these structures are driven by the laser pulse, the high-charge electron beam pulse can also supply an impulse to the plasma ions, producing an ion filament [140] which may be the structure seen in Fig. 4.8d.

4.3.4 Betatron Radiation

The use of LWFA as a betatron radiation source was investigated in detail [117] in collaboration with Stefan Kneip. The radiation generated in a 10 mm gas jet was measured using an Andor CCD camera (DX434-BN) [141] and found to be similar to radiation from an undulator with strength parameter $K = 1.5$, source size as small as 1 μm, and peak brightness $10^{22} photons/s/\ mm^2/mrad^2/0.1\%BW$. The source size was measured from the x-ray shadow first of standard radiography targets as shown in Fig. 4.12 and then using a cleaved edge of an InSb crystal.

In a second experimental campaign, x-ray flux measurements were taken using the Andor deep depletion CCD camera, which is less sensitive to photons with energy $< 2\ keV$ and more sensitive over the range $4 - 20\ keV$ as compared to the DX434-BN model. All data shown in this section were taken with a 360 nm Al filter as well as Mylar filters of differing thickness. The detector subtended a solid angle of $4.77 \times 4.77 \pm 0.01\ mrad^2$ as measured from the front of the nozzle. This solid angle is smaller than the FWHM beam divergence (found previously to be $4 \times 13\ mrad^2$) and comparable to the shot-to-shot pointing stability. The measured signal can vary by an order of magnitude shot-to-shot. This is likely due to the fact that the detector angle is smaller than the pointing stability and therefore the peak of the x-ray beam often misses the detector. Because of the linearity of the detector (1% maximum

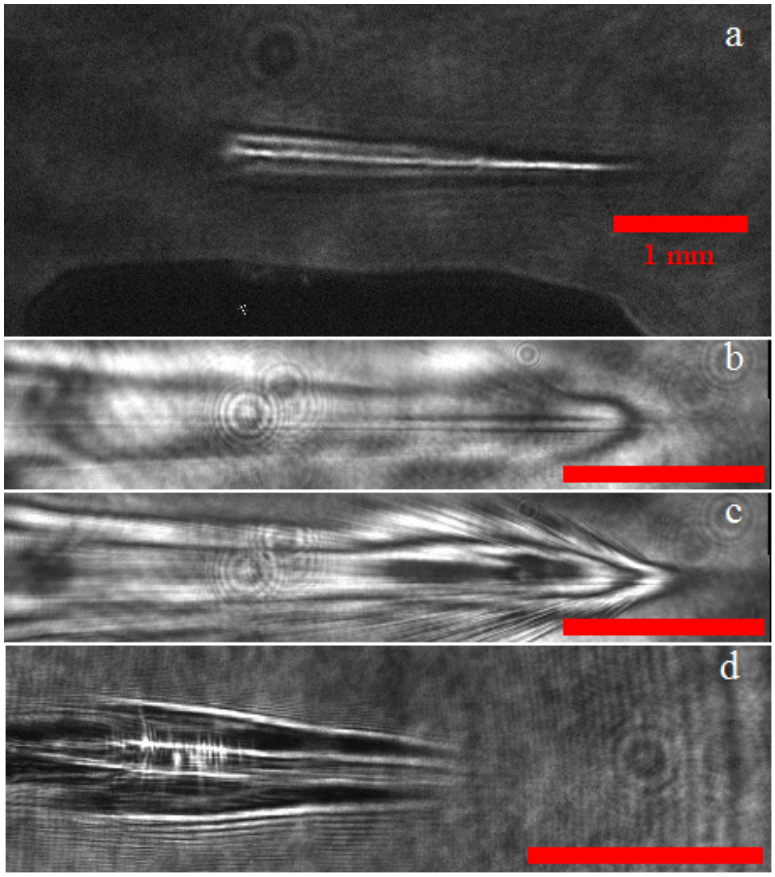

Figure 4.8: Transverse shadowgrams demonstrating features of the interaction plasma, each illuminated less than 20 *ps* after laser arrival (laser moves from right to left) at the front of the vacuum/plasma interface. In (a), the plasma is visible as a cone 1 *mm* above the gas jet orifice. A single central channel is observed, possibly indicating a self-guided laser spot. As density is increased, laser/plasma instability can cause severe laser scatter and filamentation (c) and (d). High charge electron beams may also produce an ion filament (d). In each shadowgram, 1 *mm* is indicated by a red bar.

deviation), the number of counts above readout noise integrated over the detector is a good indicator of the total energy in x-rays within the response window of the detector+filter system (roughly $4-20\ keV$) though the number of photons cannot be calculated from this data without making assumptions about the photon energy spectrum. If the x-ray spectra change significantly shot-to-shot, particularly if the spectra have critical energy around $4-5\ keV$ (below which the transmission of Mylar drops), this would also contribute to the observed shot-to-shot variation. Additionally, the x-ray beam divergence is likely very sensitive to the electron beam divergence, energy, and source size which all vary shot-to-shot and depend on experimental parameters such as density.

Fig. 4.9 demonstrates the x-ray total energy flux F as a function of density for three laser power settings. Each data point gives the flux averaged over several shots (at least 4 and as many as 16) at identical experimental conditions and error bars span one standard deviation of those shots. Shots with $< 20\ pC$ electron beam charge were excluded. As laser power is increased, x-rays can be generated at lower density and the total x-ray energy increases approximately as P^2 (see inset plot). These effects can be explained by considering the effect of laser power on the LWFA process. As shown earlier in this chapter, the threshold injection density scales as $P^{-0.8}$. The beam charge has also been observed to increase with power and the maximum energy gain is expected to scale linearly with charge. Considering that $\lambda_{LWFA\beta} \propto \gamma^{-3/2}$ and $E_{crit} \propto \gamma^2 r_0$, it is not surprising that the betatron flux increases more than linearly with power.

The rise and fall in flux with increasing density within each curve is due in part to the trend in trapped electron beam charge discussed earlier in this chapter. As shown in Fig. 4.10 (top), both the betatron flux (blue) and charge (green) are plotted for 17 shots with notable correlation between betatron flux and beam charge. These data were taken with a 5 mm nozzle and laser power $58.4 \pm 2.5\ TW$.

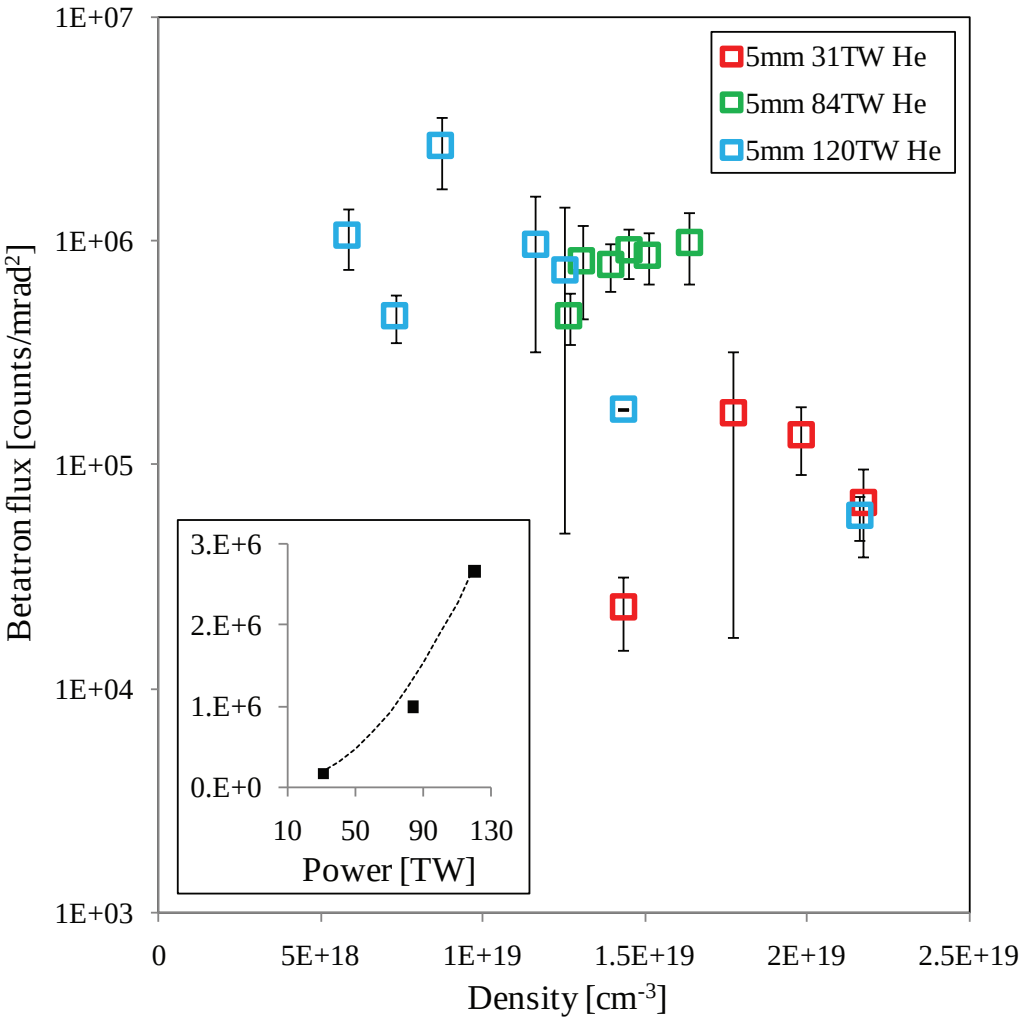

Figure 4.9: Scans of betatron flux as a function of density for three laser power settings. The rise and fall of each curve with increasing density is characteristic of the trend in trapped electron beam charge. The inset plot shows the maximum flux at each power level with a black dotted line showing the curve fitting $F \propto P^2$.

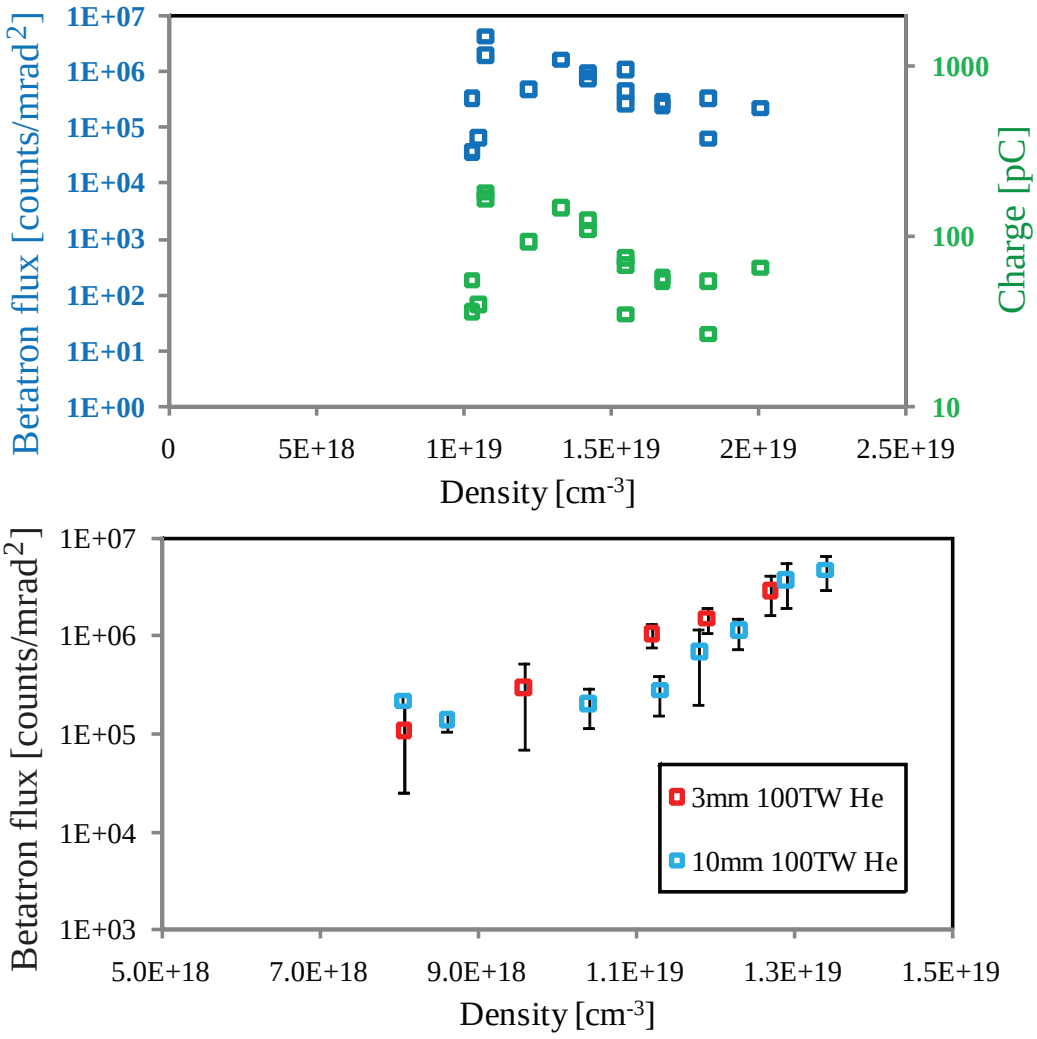

Figure 4.10: (top) Correlation is shown between beam flux (blue) and charge (green) for 17 shots. (bottom) The flux as a function of length is unclear. No data is available at the same filter level for the densities of most interest (below 8×10^{18} cm^{-3}). For densities above 1×10^{19} cm^{-3}, the dephasing length is less than 3 mm. Therefore above this density the flux is expected to be identical for the two curves, but below this density, the 10 mm nozzle would be expected to give a higher flux.

The spectrum of the radiation was first measured using Ross filter pairs [142]. A single Ross filter pair consists of two x-ray filters with similar transmission curves, but differing transmission over a certain energy window. A piecewise picture of the spectral shape of a source can be constructed by using multiple Ross filter pairs in the same exposure. As described in Ref. [143], the spectral data taken using the Ross filter pair technique were fit to synchrotron spectra characterized by the parameter E_{crit}, the critical energy, and found to fit best to a critical energy up to 8 keV.

Additionally, the spectrum was measured using the Andor CCD where the x-ray flux was controlled such that each pixel of the CCD on average was hit by $\ll 1$ photon. This was achieved primarily by extending the source-detector distance and also using Mylar and/or metal filters. The extended separation also helps evenly illuminate the detector but makes pointing fluctations more problematic. In this "single-hit" case the signal from a single pixel could be attributed to a single photon, with signal proportional to the photon energy. The detector energy scale was calibrated using both Fe-55 and Am-241 radioactive sources and exhibited excellent linearity over the range $5.9 - 21$ keV. The histograms taken from the single-hit data indicate as many as 10^{11} photons per steradian within the range $3 - 25$ keV averaged over the detector, which was 4.77 $mrad \times 4.77$ $mrad$.

The radiation was also found to exhibit spatial coherence, allowing for phase contrast imaging as demonstrated in Figs. 4.13 & 4.14. The parameters of the beam are summarized and compared to existing and planned facilities in Table 8.2 in Ch. VIII.

4.4 Conclusions

An extensive collection of LWFA data has been taken with nozzle lengths between 500 μm and 10 mm and laser power up to 136 TW on target. The nozzle lengths studied were in most cases much longer than the diffraction length. For studies

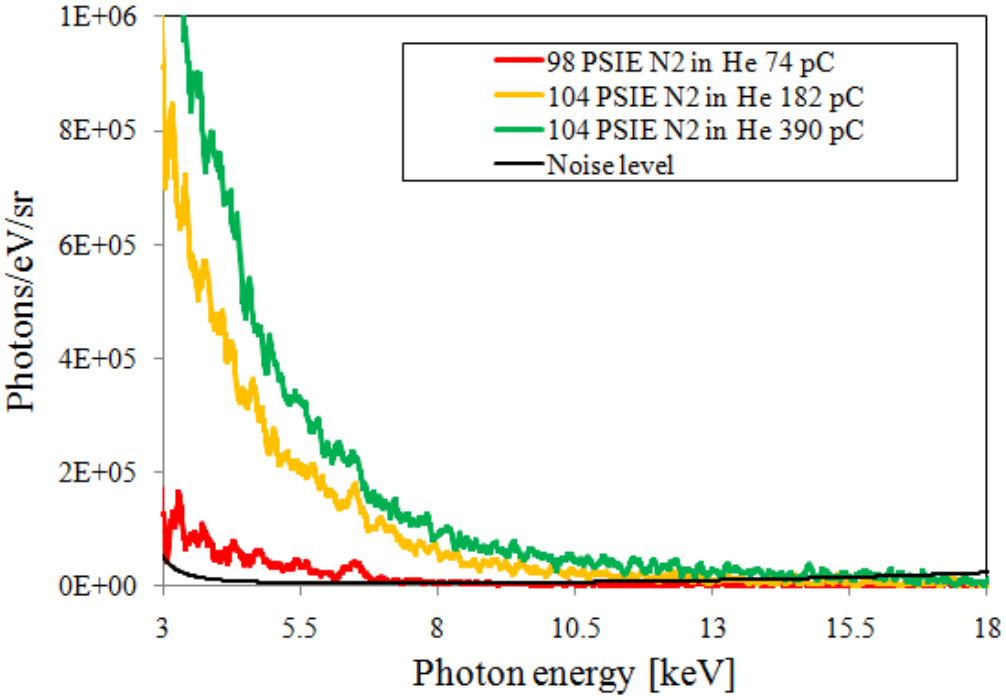

Figure 4.11: X-ray spectra acquired using the Andor CCD camera in single-hit operation.

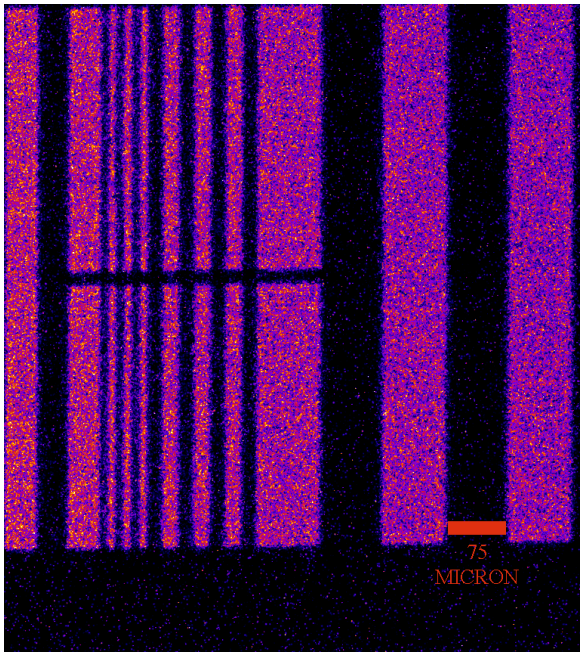

Figure 4.12: Betatron radiogram of a resolution test target

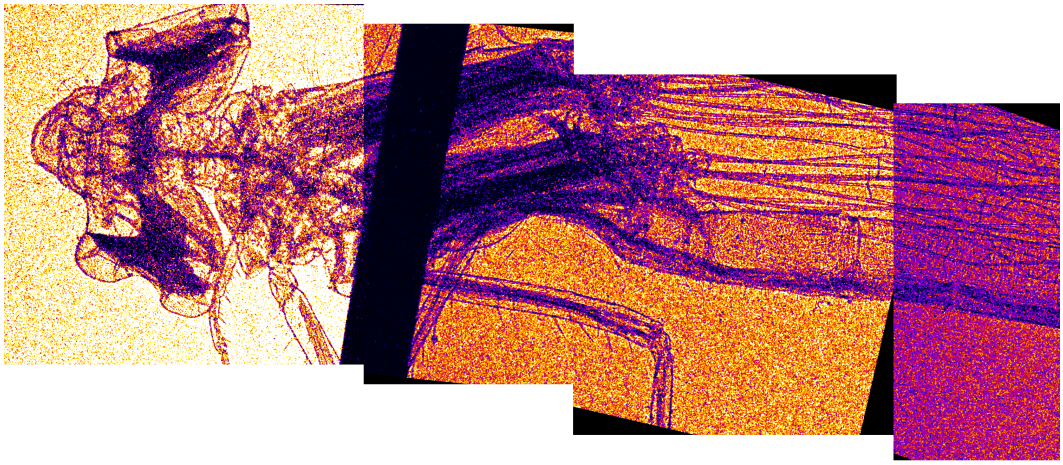

Figure 4.13: Betatron radiogram of a damselfly taken with betatron x-rays from a 3 mm LWFA. Magnification is 4.1 ± 0.1. Four single-shot images are stitched together. Spectral measurement in the single hit flux range under similar conditions found the photons to range in energy from $3 - 14$ keV. Note that useful information can be retrieved from absorption by internal structures as well as phase contrast imaging at sharp interfaces.

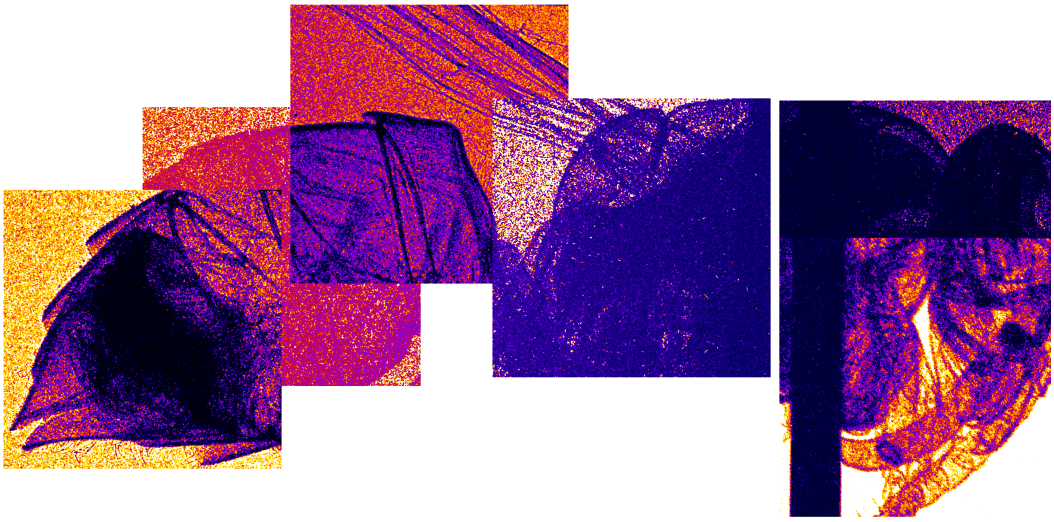

Figure 4.14: Betatron radiogram of a yellowjacket taken with betatron x-rays from a 3 mm LWFA. Magnification is 4.1 ± 0.1. The bottom right image presents the accumulation of 8 shots while the 5 remaining stitched images are single shots. Note that shot-to-shot angular jitter only mildly degrades the image resolution as shown in the 8 shot accumulation.

conducted well above the injection density threshold, the dephasing and depletion lengths were shorter than the nozzle length. However, the most interesting parameter space was the regime of density slightly above the injection density threshold. For this reason, nozzles were chosen to be equal to or shorter than the dephasing and depletion lengths at the density threshold for the anticipated laser power. In these experiments, plasma density was the most important parameter in controlling electron beam parameters as both the injection and acceleration dynamics depend critically on density. The density parameter space investigated in these experiments included regimes where $\lambda_p > 2c\tau$ as well as $\lambda_p < c\tau$. The wakefield accelerator is operated at nearly matched conditions such that the laser pulse will evolve by self-guiding to a waist of λ_p and by self-compression to a pulse duration $\lambda_p/2c$. This is especially true for the threshold studies presented here. As described in Ref. [144], in this nearly matched bubble regime, the injection threshold vector potential predicted in theoretical work [145] can be converted to a threshold value for the product of laser energy and plasma density. The formulation therefore predicts an injection threshold density which scales as P^{-1}. In this work, the injection threshold density was found to scale as $P^{-0.8}$ and for 100 TW laser power, the injection density threshold was found to be $5.1 \pm 1.0 \times 10^{18}\ cm^{-3}$ for which $\lambda_p/c = 49\ fs$. Ref. [144] predicts the threshold density to be $3.8 \times 10^{18}\ cm^{-3}$ for these conditions. The discrepency in this case is likely due to the fact that theoretically scalings assume a fixed density while our measured density profiles are not uniform longitudinally and the values quoted in this thesis are maximum densities. This also explains why the energy gains observed in Fig.4.4 were slightly below the values predicted by theoretical scaling. The experimental conditions and electron beam parameters found during the experiments within this chapter are summarized in Table 8.1.

CHAPTER V

Guiding in Capillary Waveguides

5.1 Introduction

In the presence of a plasma waveguide where the background plasma density is diminished by $\Delta n_{ch}(r)$ on axis and where the initial radial density profile is described by $n = n_p + \frac{\Delta n_{ch}}{n_p}\frac{r^2}{w_0^2}$, Eqn. 2.10 must be modified to:

$$\eta(r,\zeta) \cong 1 - \frac{\omega_{pg}^2}{2\omega_0^2}\left(1 + \frac{\Delta n_{ch}}{n_p}\frac{r^2}{w_o^2} + \frac{\delta n}{n_p}\right) \tag{5.1}$$

For a laser spot with waist radius w_0 in a parabolic density trough of width r_{ch} such that $w_0 = w_M \equiv (r_{ch}^2/\pi r_e \Delta n_{ch})^{1/4}$, the laser spot will remain focused with the matched spot radius w_M. For an unmatched spot, diffraction and guiding will alternately cause overshoot and undershoot of the matched spot size set by the channel.

Perhaps the most technologically straightforward method for creating such a plasma waveguide is the ablative wall capillary discharge, which establishes a guiding structure by ablating and heating material from the inner walls of a plastic capillary via low current discharges of $200 - 400$ A. Plastic (carbon and hydrogen) is used as the material in order to keep the average Z of the plasma as low as possible. These were the first capillary discharge devices to demonstrate guiding [146–149] and such capillaries are much easier and cheaper to construct than gas-filled capillaries

[150, 151, 41, 152, 153], which are typically made of sapphire. However, as will be discussed in this chapter, the ablative capillary has some additional challenges that gas-filled capillaries avoid such as shorter lifetime and less control over the ionization state and total density of the plasma.

A significant recent result was the demonstration of extended laser acceleration distances using a hydrogen filled capillary discharge plasma waveguide, which was shown in 2006, to be able to generate accelerated electron beams to 1 GeV over a distance of only 3 cm using a laser power of 40 TW [41]. This was the first measurement of laser produced electron beams in the GeV range and demonstrated guiding at relativistic intensity using a hydrogen filled-capillary waveguide. In another experiment [154] a 0.56 GeV electron beam with 10 fC charge was observed using a 4 cm ablative capillary similar to this experiment. There has subsequently been research to improve the understanding of the details of plasma wave production and electron acceleration in such plasma waveguides, and subsequent experiments using hydrogen filled capillary waveguides have shown similar acceleration [152]. However another recent experiment showed that the mechanism for generating these beams with hydrogen filled capillaries was more complex than previously thought [153], and that electron injection was intimately related to the process of ionization of the target plasma by the intense laser pulse. In such experiments good guiding and an extended propagation distance of the high power laser pulse were a necessary but not sufficient condition for the production of relativistic electron beams from the capillary discharge plasma waveguides. In that work it was found that only when ionization was attributed to the main laser pulse (15 TW) could accelerated electron beams be measured. Other types of plasma waveguides have also been explored and have been the subject of a significant amount of recent research including the use of gas filled hollow glass capillary waveguides [155, 156]. There are also for all-optical waveguide production [157–159] by using a second laser pulse to form a plasma waveguide for

a subsequent interaction pulse. The method in reference [157] is likely ineffective for guiding pulses with intensity $> 10^{15} W/cm^2$ and the latter two references require a $> TW$ laser to be used as a self-guided channeling beam.

Portions of this chapter, including Figs. 5.1, 5.3, 5.4, 5.5, 5.6, 5.7, and 5.8 and their descriptions have been reprinted with permission from [160]. Copyright 2009, American Institute of Physics.

5.2 Experimental Setup and Calculations

For these experiments the HERCULES laser system was operational up to 35 TW and was focused by an $f/10$ off-axis parabolic mirror to a 20 μm spot diameter (FWHM) without wavefront correction and without XPW. 3 cm polyethylene capillaries were used which had a 400 μm diameter bore. The bores were machined as small as a 250 μm into a 1" diameter cylindrically shaped polyethylene. This can be done with a standard drill press. Laser machining bores with such a high aspect ratio is challenging. Also, commercial extruded plastic microtubing may be able to produce more clean and consistent holes than machining. However these tend to have $\sim$ mm outer diameter and it was found to be difficult to sufficiently insulate to prevent discharge around the outside of the tubing.

The bulk machined capillaries were carefully insulated with additional bulk plastic and silicone for full enclosure over a radius of several inches. Initial alignment was performed by maximizing the laser light transmitted through the empty capillary at low laser power (300 μJ per pulse at 10 Hz). The capillary could be controlled remotely in three orthogonal axes as well as two rotational axes. Brass electrodes were placed at the ends of the capillary and a capacitor (~ 1 nF) was connected to the electrodes and charged to ~ 20 kV. The discharge was triggered by ablating the inner walls of the capillary with a focused Nd:YAG laser pulse ($30 - 100$ $mJ, 10$ ns, $\sim$ 5x$10^{10} \frac{W}{cm^2}$). This "igniter pulse" controls the timing of the discharge to within

about 5 ns accuracy. A delay generator was used to control the timing between a clock pulse from the Ti:Sapphire system and the Nd:YAG q-switch. The arrival of the two pulses at the experimental chamber was monitored using photodiodes and an oscilloscope. The experimental setup is shown in Fig. 5.1.

At the end of its lifetime, a capillary can be replaced in the same mount and only brief realignment is necessary. The operational lifetime of a typical capillary was found to be several hundred shots. The bore diameter increases by as much as 50% over this period ($\sim 1\mu m$ per shot), indicating that optimum conditions for guiding will shift throughout this time. This lifetime limitation is caused mainly by material ablation from the walls during the discharge and not from the high intensity laser interaction. Consequently the high laser power used during the experiment typically did not affect the operation of the discharge.

An uncoated glass wedge was used to reflect some of the transmitted light, which was then collected by a lens (2" diam x 20"f) and imaged by a second lens (3" diam x 1 mf) and 10x microscope objective onto a Coolsnap 12-bit CCD to monitor the transmitted laser mode. A beamsplitter was also used to send some of this light to a manual imaging optical spectrometer to monitor changes in the transmitted laser spectrum. The spectral window was 426 nm.

5.3 Waveguide Creation

Stark broadening of the hydrogen α line was measured across the capillary output by Michael Levin [149] to confirm that these ablative capillaries show a parabolic density structure (Fig. 5.3a). Typical densities of $1 - 3\text{x}10^{18}$ cm^{-3} on axis were achieved, with the density increasing with the applied voltage and decreasing at later time. Note that such densities are considerably lower than the densities attainable using gas-filled capillaries. However, this measurement was taken without a high intensity interaction pulse. To model its propagation through the plasma channel,

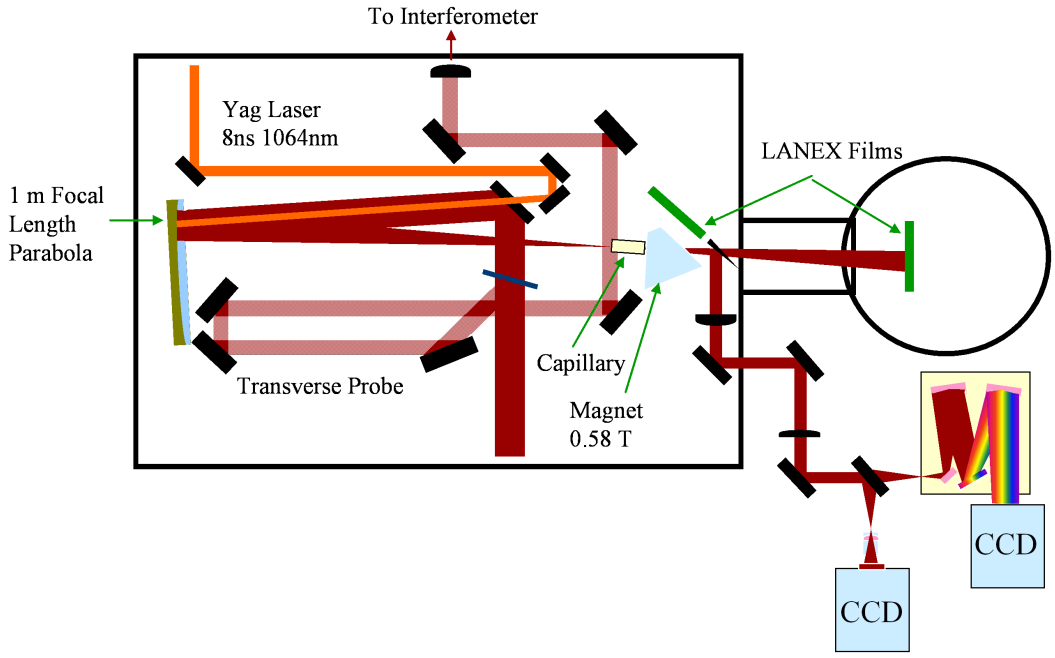

Figure 5.1: Diagram of the experimental chamber as arranged for ablative capillary experiments. The Nd:YAG ignitor (orange, from top) and the HERCULES pulse (red, from bottom) are both focused to the entrance of the capillary using the same parabolic mirror. The high intensity pulse is guided and collected with a 2" wedge. The collected light is split with a broadband 50% beamsplitter to observe the mode image as well as the spectrum.

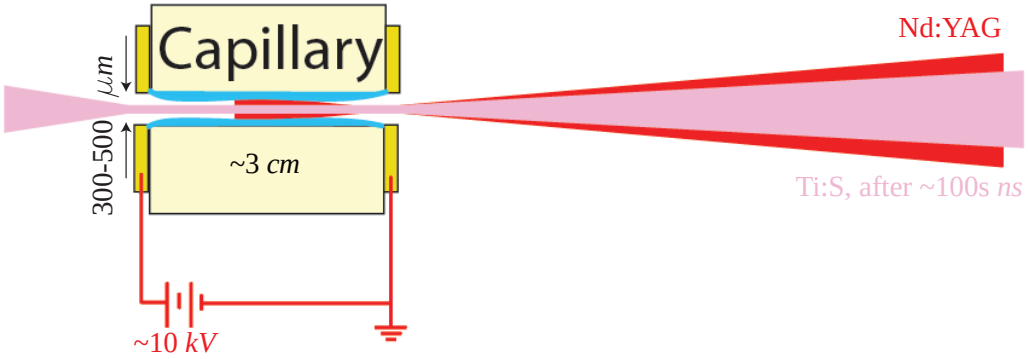

Figure 5.2: Diagram showing the processes within an ablative capillary. An ignitor pulse arrives from the right, causing ablation and breakdown within the capillary. After a certain delay, a suitable guiding channel exists at which time the high intensity pulse (pink) is guided from right to left.

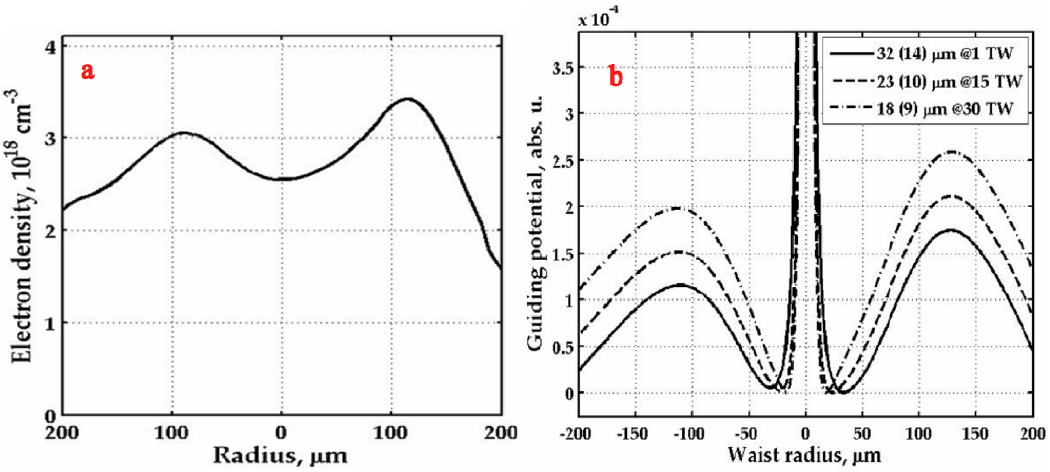

Figure 5.3: (a) Measured electron density within a discharged capillary waveguide before the arrival of the high intensity pulse. (b) Guiding potentials derived from the profile shown in (a) for three values of the guided beam power. Matched (minimum value) beam radii are specified for each potential. Image courtesy of Michael Levin

the plasma refraction index $\eta(r)$, derived from the experimentally measured radial density profile and modified via relativistic electron mass increase, was substituted into the envelope equation [61]

$$\frac{\partial^2 r_s}{\partial z^2} = \frac{\lambda^2}{\pi^2}\frac{1}{r_s^3} + \frac{e}{r_s}\left\langle r\frac{\partial}{\partial r}\eta(r)\right\rangle_r \tag{5.2}$$

where the angular brackets denote the intensity-weighted radial average of the enclosed quantity. Eq. 5.2 describes the longitudinal evolution of the guided spot radius r_s , and can be made analogous to the equation of motion of a particle subjected to a one-dimensional potential field V_s, so that $\partial^2 r_s/\partial z^2 = -\partial V_s/\partial r_s$ [161]. The function V_s is obtained by integrating the right-hand side of Eq. 5.2 with respect to r_s, and can be called the "guiding potential". The condition $\partial V_s/\partial r_s = 0$ corresponds to a constant ("matched") spot radius. It can be shown that for a Gaussian beam profile

the guiding potential is given by

$$V_s = -\left[\frac{\lambda^2}{2\pi^2}\frac{1}{r_s^2} + 8\int_{r_s}\frac{dr_s}{r_s^3}\int_0^\infty r^2\exp(-2r^2/r_s^2)\frac{\partial\eta}{\partial r}dr\right] \tag{5.3}$$

The result of application of Eq. 5.3 to the radial density profile shown in Fig. 5.3a is presented in Fig. 5.3b for three values of the guided beam power. It can be seen that the matched beam radius decreases as the laser power increases due to relativistic self-focusing. In fact, the guiding potential is much more informative than the density profile from which it was derived. The whole range of possibly guided beam radii for a given power can be inferred at a glance including the matched spotsize and the amplitude of oscillation in size can be seen for a given unmatched spot.

The timing window appropriate for guiding is determined by the hydrodynamic evolution of the plasma within the capillary. As shown in Fig. 5.5, the timing window is approximately 150 ns wide. The optimum delay (arrival time of the high intensity pulse relative to the igniter, or discharge triggering pulse) was found to depend on discharge parameters, laser power, as well as an observed slow variation in the alignment and timing as the accumulated number of discharges of the capillary slowly increased the bore diameter.

5.4 Experimental Results

5.4.1 Guiding Results

Guiding over 3 cm was achieved, first with the regenerative amplifier level of HERCULES (300 μJ) and also at powers up to 35 TW. Guiding over this length already offers a significant increase over the self-guided interaction lengths achieved in gas jet targets. As laser power was increased the parameter space which could repeatably accomplish good guiding (determined by the integrated signal within a 55 μm radius

of the peak) was found to shrink. As will be shown in this chapter, this result may be explained by field ionization of ablated capillary material by the HERCULES pulse and subsequent ionization-induced laser defocusing as well as propagation instabilities such as laser filamentation which is discussed in Sec. 6.3.

The images of Fig. 5.4 demonstrate the observed guiding behavior in these ablated capillary waveguides. A reference shot of the laser at focus is shown (top-left). Typical vacuum spot parameters without correction by deformable optics were 20 μm spot diameter with 40% of energy within the FWHM spot. All other images shown in Fig. 5.4 have the same spatial scale, however, they are imaged 3 cm after the laser focus (at the exit of the capillary). Guided spots contained as much as 20% energy within a 35 μm FWHM spot. The total transmitted light is typically 15-25% of the input. As seen in Fig. 5.4, many guided spots had fluence within about one order of magnitude of the focused vacuum shot.

During the experiment it became clear that guiding was impossible at very early delay but also at very late delay and full power, as shown in Fig. 5.5. Poor guiding at early delay is explained by transit time of the ablated material. For late delay, the ablation material will eventually stagnate on axis, filling in the guiding channel. This behavior however should be independent of laser power. It was further observed that for fixed power, the quality of guiding was inversely correlated with the amount of blueshift observed (Fig. 5.6). Blueshift, as discussed in the next section, is indicative of ionization during the main pulse.

5.4.2 Laser Spectral Results

The optical spectrum showed a large amount of blueshifted light on most shots when the capillary was discharged. The blueshifted signal as a function of delay (Fig. 5.7) and lineouts (Fig. 5.8) at the exit of the capillary show very little blueshifted light for the first ~ 75 ns while the plasma was expanding from the walls. When hydrogen

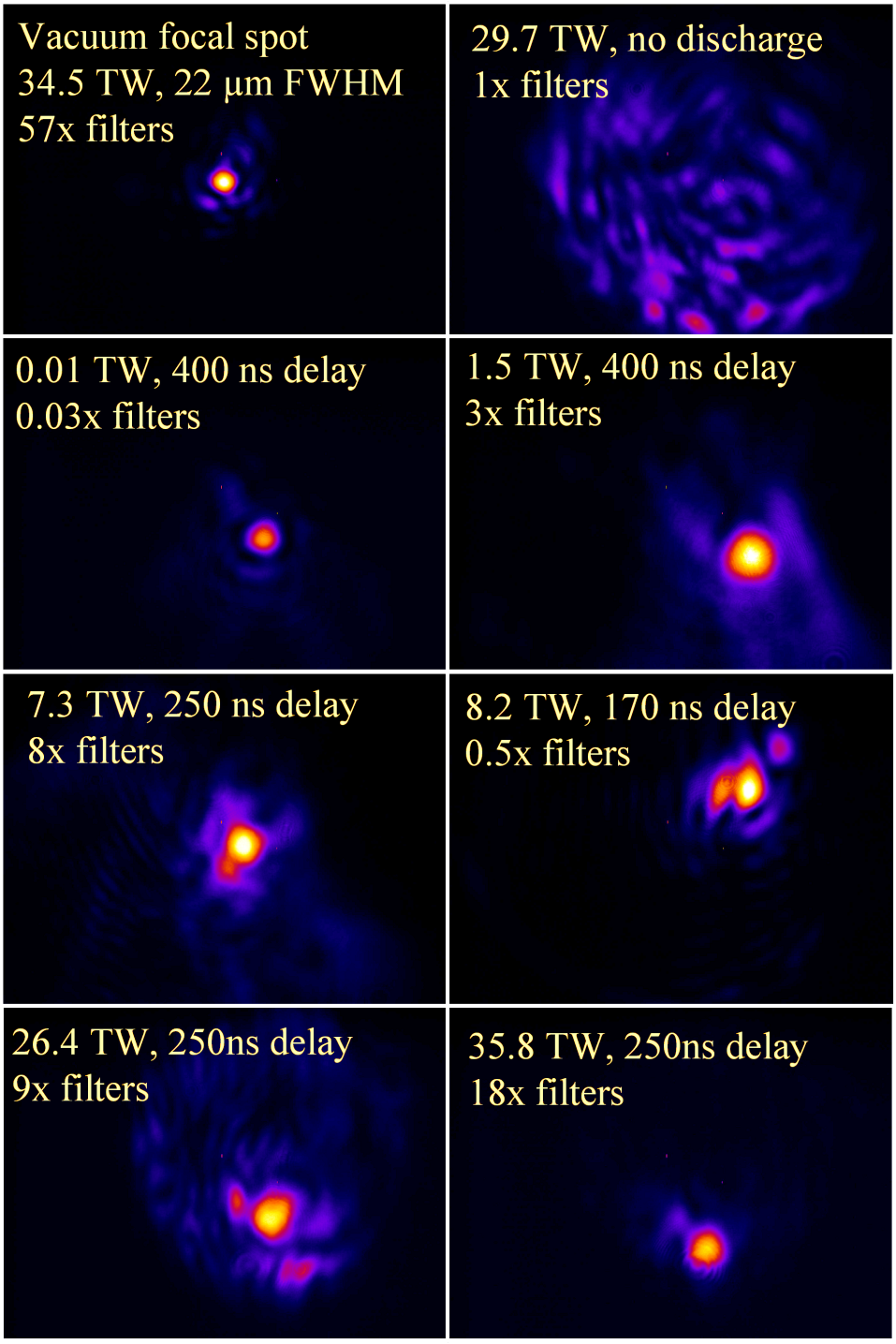

Figure 5.4: Top images are references at focus and capillary rear exit without discharge. Rows two, three, and four show guided laser modes at the capillary exit for various powers. Pointing fluctuation is real.

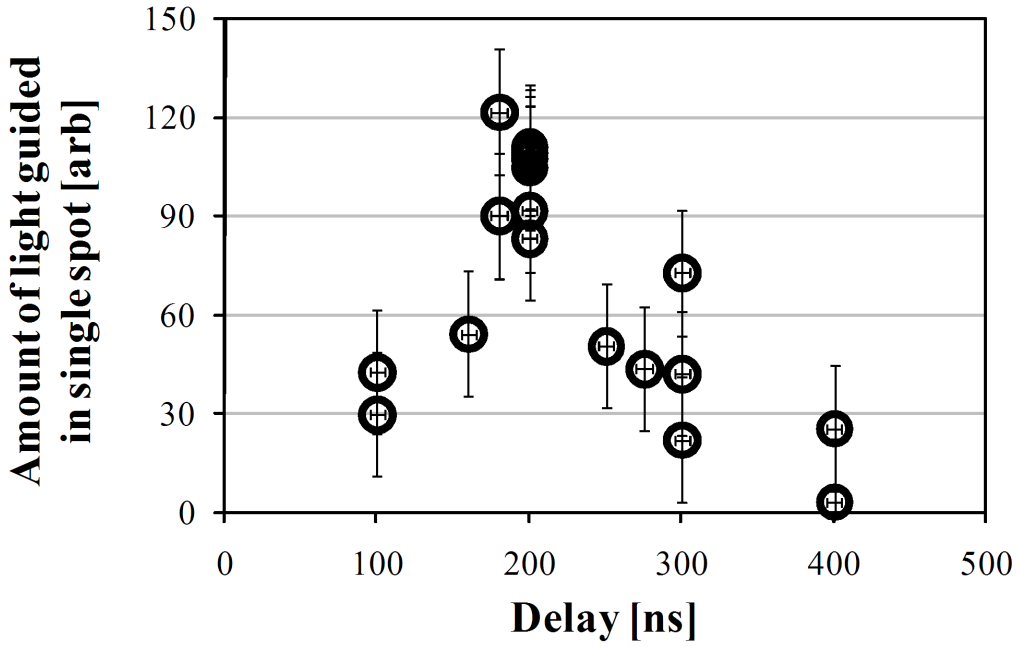

Figure 5.5: Laser guiding is achieved only within a timing window $100 - 300\ ns$ after the ignitor pulse has arrived at the capillary entrance, triggering the discharge. Each data point represents a single shot, normalized to input laser power from a single experiment at $8\ TW$. Included shots were known to be at optimal alignment and discharge parameters. Timing jitter was $5\ ns$. Vertical error bars enclose one standard deviation of all shots with identical parameters taken over many experimental runs.

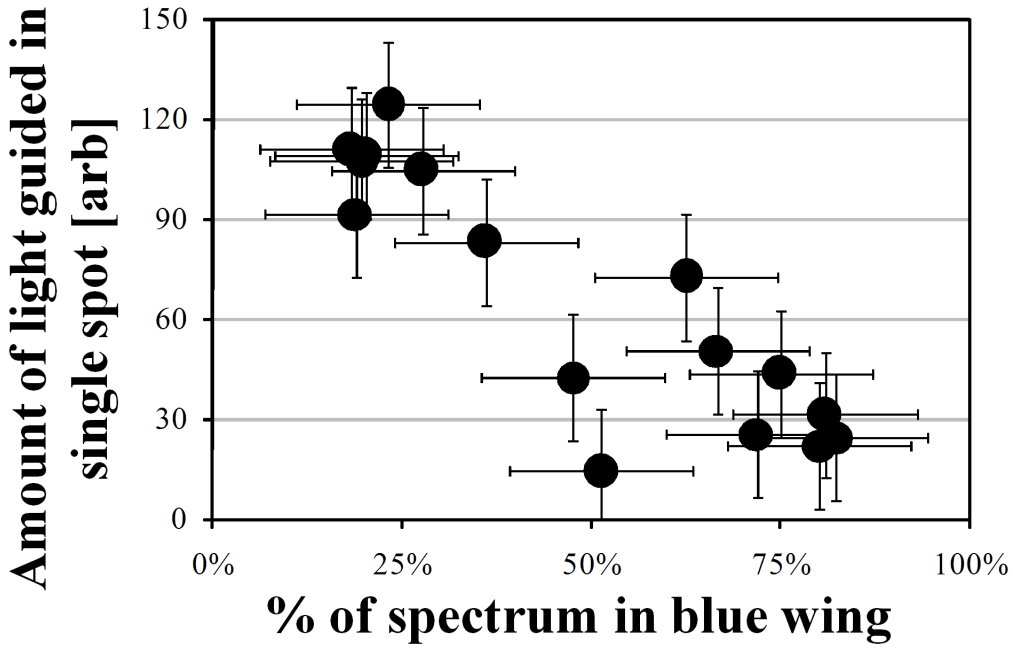

Figure 5.6: Quality of guiding is diminished when strong blueshifting is observed. Axes and error bars are the same as described in previous figures. All shots are from a single experiment at 8 TW.

ions and atoms reach the laser axis, weak blueshift of $20 - 25\ nm$ is observed. This blueshift is nearly constant over the time period $100 - 200\ ns$ delay. After $\sim 225\ ns$ delay, heavier carbon atoms and ions begin arriving at the laser axis, indicated by a sudden increase in the magnitude of the blueshift, which increases with delay as more carbon ions reach the laser axis. By 400 ns delay, nearly all the light has been blueshifted beyond the blue edge of the initial laser spectrum, followed by a slow decay as recombination takes place at the capillary walls (which we estimate should occur over nanosecond timescales). At low power, $\leq 2\ TW$, strong blueshift was not observed, and the guiding window was much wider- out to 400 ns delay. At high power, $\geq 30\ TW$, strong blueshift was observed at earlier delay, as well as significant spectral broadening and modulation. The guiding window shrank to only include delay $\leq 250\ ns$.

5.5 Conclusions

The spectral dependence upon laser power suggests that the blueshift is most likely a result of rapid ionization of the gas during the main laser pulse [55], where field ionization causes a change in refractive index which advances at nearly the laser group velocity. The blueshift was much stronger than redshift, as would be expected for a density which is rapidly increasing in time. This increase is due to field ionization of the low-charge state carbon ions in the polyethylene capillary plasma. The intensity of the triggering Nd:YAG pulse is $10^{10} \frac{W}{cm^2}$ which is too low to ionize hydrogen or carbon atoms, but the flux ($\sim 500 \frac{J}{cm^2}$) damages the capillary material. The electrical discharge ensues and any initial ionization is due to this discharge. The discharge has similar parameters to pulsed arc discharge plasmas, which typically have plasmas temperatures up to several eV. In the case of our discharge, radiative heat transfer is halted at the walls of the capillary. Consequently plasma at this temperature will have very few ions with charge states above the first ionization stage. In contrast, the

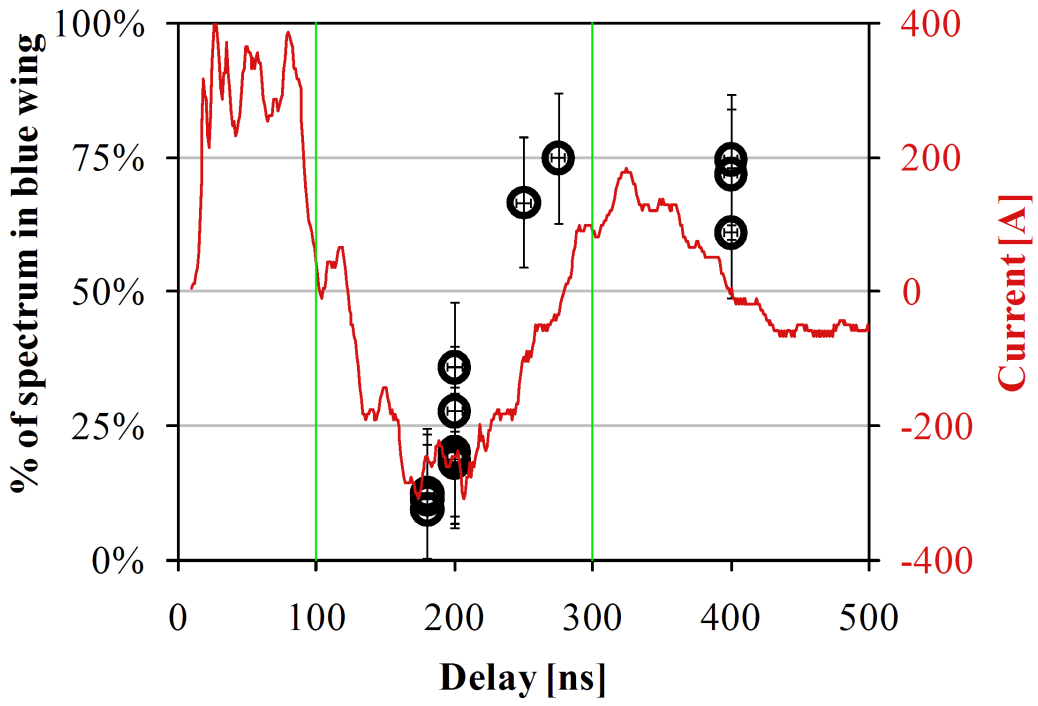

Figure 5.7: The laser is unaffected until plasma has expanded to fill capillary. The vertical axis is integrated count of laser light in the spectral window higher in frequency than the blue edge of the laser spectrum in vacuum, normalized to the total integrated counts over the entire spectrum. The timing window for guiding is approximately between the green bars. All single shots are from a single experiment at 8 TW. Vertical error bars enclose one standard deviation of all shots with identical parameters taken over many experimental runs. A trace of the discharge current is overlaid.

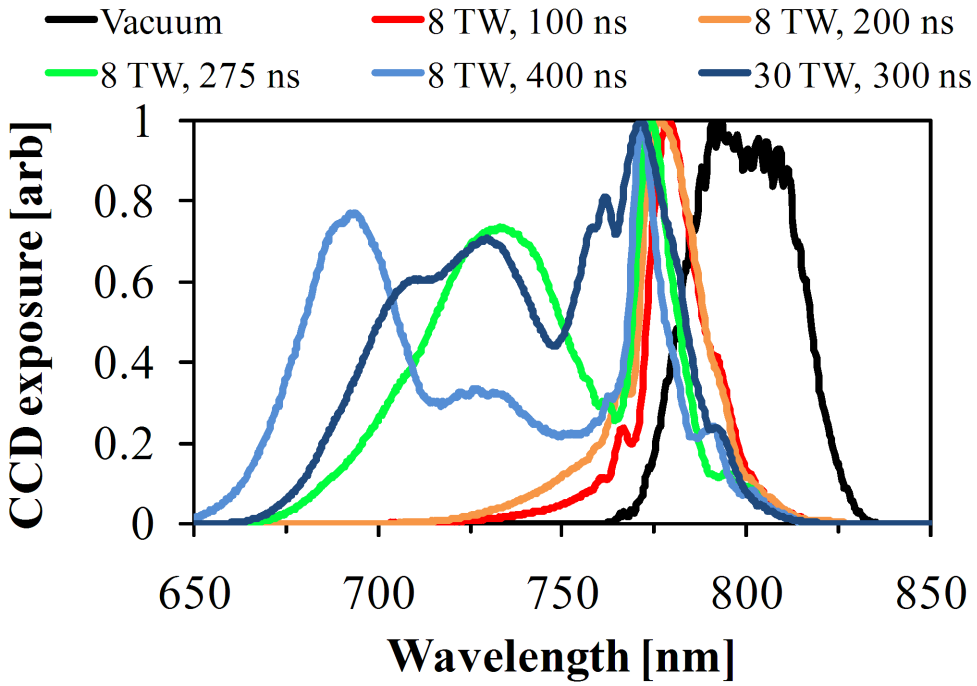

Figure 5.8: Optical spectra (individually normalized) of transmitted laser light in vacuum and with discharge at various delays and laser powers. At short delay, blueshift is weak and insensitive to delay. At larger delay, carbon ions from the wall have reached the laser axis, leading to strong ionization blueshift with shift proportional to delay. For higher power, blueshift is more prevalent.

arrival of the 35 TW pulse with intensity $\sim$ 5x10$^{18}\frac{W}{cm^2}$ is able to ionize carbon fully and oxygen six times (if there is any water contamination absorbed in the capillary wall), (estimated using the barrier-suppression ionization approximation), causing large amounts of blueshift:

$$\frac{\Delta\lambda}{\lambda^3} = -\frac{L}{2c}\frac{\partial}{\partial t}\frac{n_e(t)}{n_c} \tag{5.4}$$

where $\Delta\lambda$ is the shift in wavelength, L is the interaction length, n_e is the electron density and n_c is the critical density. Thus, blueshift is an indication of rapid field ionization, which will be most prevalent on the laser axis where intensity is highest. The overall blueshift will increase linearly with the number of electrons freed by ionization so that full ionization of carbon will result in a 6x shift compared to ionization of hydrogen at the same atomic density. In reality, the situation is more complicated than a uniform shift, where considerations must include broadening due to self phase modulation over the long guided region, spatial extent of the pulse, and interaction of the pulse with the wakefield [59, 162, 163]. Modulation of the spectrum occurs due to interaction of the pulse with wakefield density perturbations and can be substantial for pulses which are much longer than the plasma wavelength. For our short pulse case, however, the multiple spectral peaks may be due to different ionization states being reached at different spatial regions around the pulse. Indeed, by inspection of the spectra, the blueshifted peak has greatest shift on axis and lesser shift in the spatial wings (curves in Fig. 5.8 are integrated in the spatial axis). A redshift shoulder is also observed in some shots, but with two orders of magnitude lower fluence. The dominance of blueshift over redshift suggests our shift is due to ionization rather than photon acceleration via pulse/wakefield interaction. Because refractive guiding requires a minimum density on axis, strong field ionization on axis can degrade or even prevent guiding (known as "ionization-induced defocusing").

The parabolic densities measured by laser-induced spectroscopy do not take this into account, as no high intensity pulse was present. This may account for the in-

creased difficulty of achieving guiding at higher powers. As shown in Fig. 5.6, shots that were best guided were those that had the least amount of blueshifted light. This indicates that in addition to proper alignment of the capillary and appropriate timing of the discharge, field ionization plays an important role in the quality of guiding. There exists a limit on the intensity which can be guided through the discharge at hand. In other words, a pulse of certain energy should not be focused below a waist radius at which the intensity is enough for the ionization to be significant throughout the capillary length.

In these experiments no accelerated electrons were observed from the interaction of the laser pulse with the waveguide plasma at 35 TW, though electrons were observed in Ref. [154]. This is likely due to the density being below that required for wave-breaking and self-injection at this power (Ref. [154] used 3.8 J whereas we define 35 TW as 1.67 J total on target in 30 fs). Alternatively, electrons may be produced but with charge less than our detection level. Ref. [154] reports charge $\sim$ 10s of fC per shot, whereas our detection limit is estimated at 300 fC.

The quality of guiding at 35 TW was observed to be good. Parameters of the guided spot suggest that after 3 cm of propagation, the laser intensity drops only by an order of magnitude (although the transmitted pulse duration is unknown). If carbon is fully ionized by the 35 TW pulse as predicted by barrier suppression ionization, the effects of field ionization may be no worse at several hundred TW. Additionally, self-focusing may contribute to self-propagation more at higher powers. While it is clear that field ionization is correlated to degradation of the observed guiding, the presence or absence of blueshift can be unpredictable. Strong blueshift is occasionally observed at earlier delay than anticipated, especially at high power, and reproducibility of guiding is $\sim$ 50% even when all discharge parameters are optimized. This is most likely due to laser pointing fluctuations of up to 30 μrad and/or laser energy shot-to-shot fluctuations of up to $\pm$10%. Laser energy fluctuations will affect

the strength of ionization blueshift. A 30 μm radial shift in the laser focal position is a significant fraction of the size of the guiding channel, as seen in Fig. 5.3, which could explain the low reproducibility of guiding. Guiding was observed to be sensitive to alignment of the capillary within 20 μm. Pointing fluctuation will also affect the delay at which the laser focus comes into contact with carbon ions, causing ionization blueshift.

While using this low-charge-state ablative plasma adds an additional complication compared to hydrogen-filled capillaries, it may also allow for a simple down-ramp accelerator [164]. At the front of the capillary, field ionization will create a high electron density plasma, allowing electron injection and as the laser is depleted fewer charge states will be field ionized. This is not the case for hydrogen-filled capillaries, which are nearly fully ionized upon arrival of the laser pulse. Both capillary designs allow control of the density within the capillary, but control is typically more straightforward using hydrogen-filled capillaries by merely changing the neutral gas pressure. Hydrogen-filled capillaries also offer longer lifetime however "revolver" style ablative capillaries with many bores in a single bulk cylinder may increase the time between capillary replacements. Such capillaries have been manufactured. Lifetime may also increase significantly if every shot is well guided. The effects of ionization blueshift are believed to have been observed in gas-filled capillaries as well with similar dependence on delay [153]. In this case the amount of ablated wall material is presumably much smaller than in ablative capillaries and ionization blueshift does not seem to be detrimental to guiding. Field ionization of wall contaminant materials may even be beneficial in gas-filled capilaries (Ch. VII so long as ionization defocusing does not dominate. On shots up to 35 TW, electrons were not observed - i.e., there was no wave-breaking or self-trapping. For the density estimate of $1 - 3\text{x}10^{18}\ cm^{-3}$ this is to be expected. In typical gas jet runs on HERCULES with 35 TW, the required threshold density for self-trapping of detectable electrons is $\sim 9\text{x}10^{18} cm^{-3}$ (peak density-

no axial averaging). Increasing laser power to 300 TW will decrease this threshold to $\sim$ 2x10^{18} based on past scaling on HERCULES. To surpass this density within the capillary, the energy of the Nd:YAG laser used to trigger the discharge may be increased (at the cost of decreasing the lifetime of the capillary). Increasing the discharge current may also increase the charge state of the plasma, thus increasing density, but may also decrease the lifetime of the capillary. Using a smaller bore capillary will also increase density. Smaller bore capillaries ($\leq$ 250 μm), in conjunction with control of the spot size using adaptive optics, will allow use of the appropriate density for injection while remaining close to the matched spot size.

CHAPTER VI

Self-guiding in Gas Cells

6.1 Introduction

A gas cell is an enclosed reservoir filled with gas at relatively low pressure compared to the backing pressures required for the supersonic gas jets described in Ch. IV. The high pressures required for sufficiently high density from large-diameter gas jets eventually become a limiting factor and so gas cells become interesting for studies of LWFA with lengths $> 1\ cm$. This advantage comes at the expense of the sharp gas/vacuum interface introduce by supersonic jets. The gas within the cell must be contained at the entrance by a pinhole.

Gas cells have already demonstrated LWFA of electrons up to $\sim 200\ MeV$ [165]. It is worth noting that this paper also demonstrated exceptional stability in electron spectrum, max energy, and beam pointing. Stability of these parameters has been one of the major concerns with the use of gas cells instead of gas-filled capillaries. Self-guiding has also been observed in long gas jets and cells extending up to 14 mm [66].

6.2 Experimental Setup

The experimental setup for this experiment is similar to the setup for gas jet experiments. As shown in Fig. 6.1, the HERCULES beam is focused into the front of the gas cell entrance. With minor adjustments, the setup can be switched between $f/10$ and $f/20$ focusing using a 1 m or 2 m parabolic mirror, respectively. A partially reflected beam (shown blue) probes the plasma transversely for interferometry or shadowgraphy by blocking one arm of the interferometer.

The specially designed cell, shown in Fig. 6.2, allows exceptional control of the density, and its multiple inputs allow tailored density profiles. The cell also has windows on two opposing sides as well as the top, allowing for transverse probing and top-scatter imaging. Because of the extra length available in gas cells, the most interesting aspect of this experiment was studying the laser propagation over lengths ≥ 1 cm.

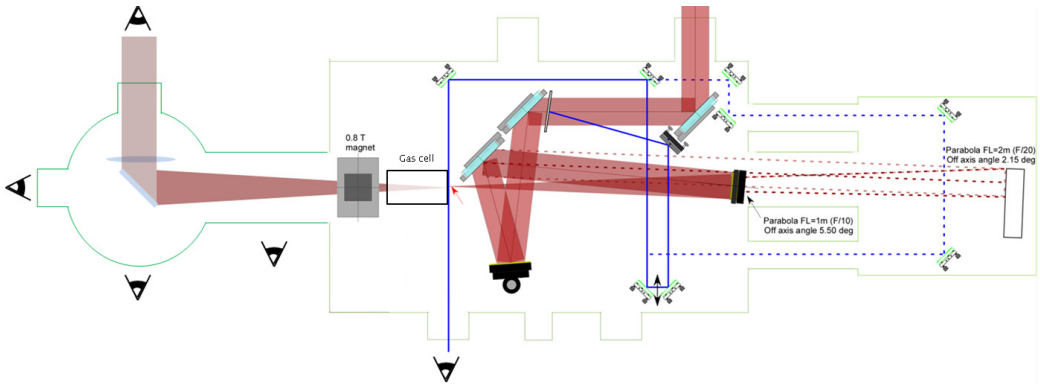

Figure 6.1: Diagram of the experimental chamber as arranged for gas cell experiments. The HERCULES beam is focused approximately one Rayleigh range (100s of μm for all setups in this dissertation) into the front of the gas cell entrance. With minor adjustments, the setup can be switched between $f/10$ and $f/20$ focusing using a 1 m or 2 m parabolic mirror, respectively. A partially reflected beam (blue) probes the plasma transversely. Common diagnostics include an electron spectrometer, electron profile monitor, transmitted light imaging and spectrometer, scattered light imaging, and an x-ray CCD.

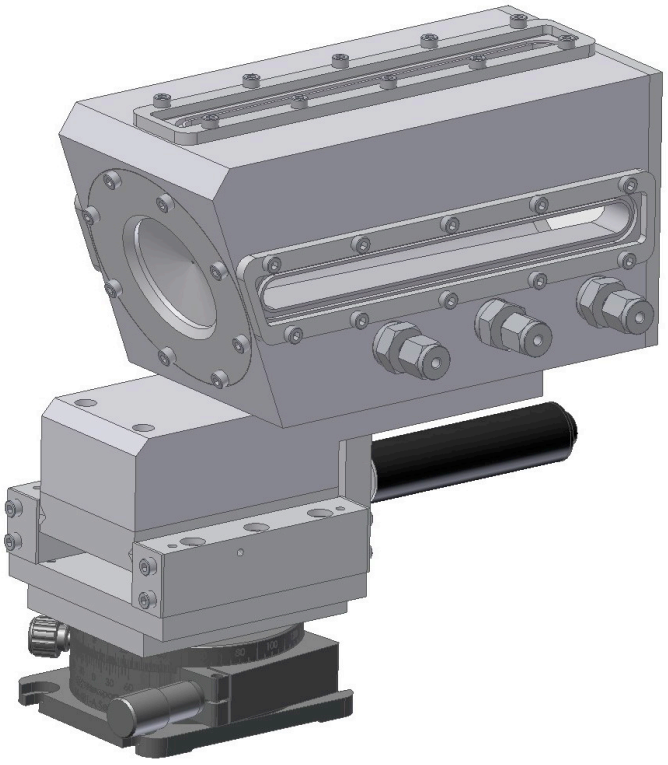

Figure 6.2: Diagram of the gas cell used in these experiments. The length of the cell is adjusted manually by selecting one of various rear inserts while the entrance position remains fixed. A 100 μm pinhole at the entrance confined the gas. Drawing courtesy of Pete Brummit (Rutherford Appleton Laboratory) and Stuart Mangles (Imperial College).

To study laser propagation throughout the cell, a laser mode diagnostic was fielded on this experiment. The exit of the capillary was capped with a 1" diameter, 100μm thick transparent mylar window. The transmitted light propagated 87 cm where a few percent of the light was reflected by an uncoated glass wedge at 45° incidence and was then recollimated using a 1 m focal length lens. The light was filtered by one order of magnitude before exiting the chamber through a fused silica window. The light was reimaged using another 1 m focal length lens and a 10x microscope objective and captured by a 12-bit CCD. The objective and CCD could be moved together on a single translation stage, covering image planes between the laser focus and up to 32.9 mm behind focus. The stage position was correlated to image plane positions by placing a 90-line per inch mesh at various depths into the gas cell and moving the CCD translation stage until the sharpness of the mesh image was optimized. The correlation was nearly 1:1 as the imaging system was made as close to 1:1 as possible.

6.3 Experimental Results

The primary data discussed in this section is the analysis of laser propagation as a function of density for two different focusing geometries. Shown in Fig. 6.3 are inset 12-bit CCD images (a and b) of the laser focal spot in vacuum imaged at focus and 6.6 mm behind focus, respectively. The focusing geometry was $f/20$. A lineout through the peak is plotted in red. This lineout has a 22 ± 1 μm FWHM. A Gaussian beam with a 21 μm FWHM is shown in solid black. Another Gaussian is plotted with FWHM= $2w_{6.6}$ where $w_{6.6}$ is the expected waist radius 6.6 mm away from focus for a beam obeying Gaussian beam diffraction, $w(z) = w_0\sqrt{1+(z/z_R)^2}$ with w_0 chosen to be 10.5 μm. Another lineout, shown in green, is taken in the vertical direction from the laser mode (inset b) 6.6 mm behind focus in vacuum. Each curve is normalized to its own peak and centered manually. This makes the data readily visible. Transmission as a function of cell length will be discussed later in the text.

Figs. 6.4, 6.5, & 6.7 are presented in this same manner, but with at least one lineout taken with plasma rather than vacuum.

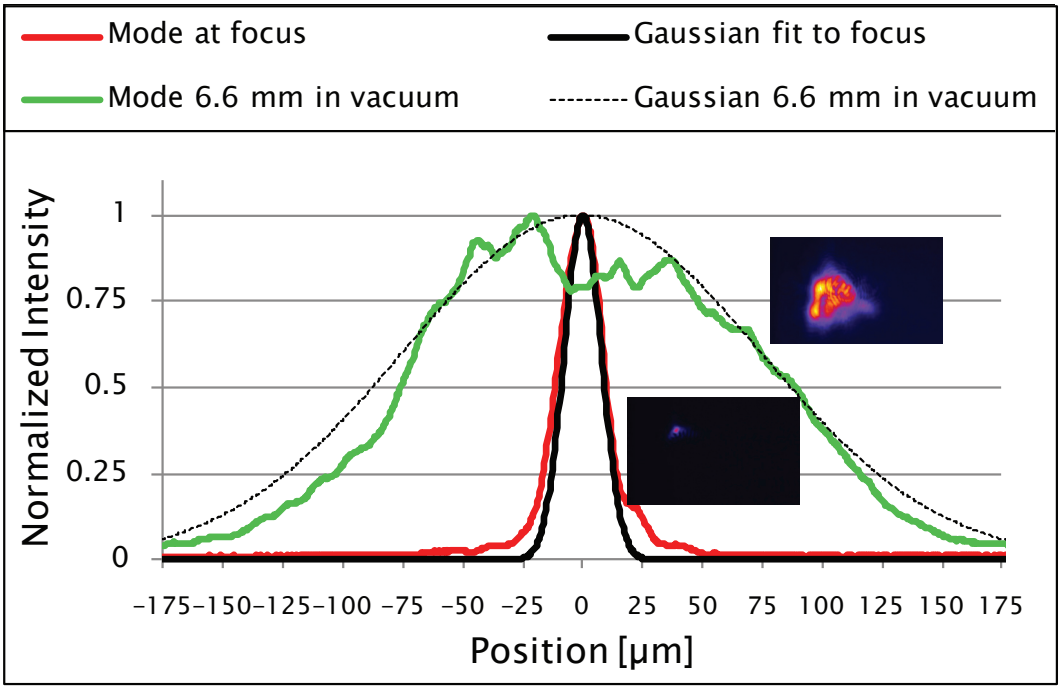

Figure 6.3: Image from the vacuum laser focal spot from $f/20$ focusing geometry (lower) and lineout (red), a Gaussian with the same FWHM (black solid), the expected Gaussian 6.6 mm behind focus (black dashed), and the vacuum laser spot imaged 6.6 mm behind focus (green and upper image). Each curve is individually normalized and centered.

6.3.1 Beam Filamentation

As discussed in Sec. 2.2.3, self-focusing can result in beam filamentation as multiple regions across the face of the laser profile self-focus to multiple spots. Filamentation was observed over a large portion of the experimental parameter space investigated (30-100 TW, $10^{18} < n_e < 1.5\text{x}10^{19}$). The maximum peak intensity in these experiments was 2×10^{19} W/cm^2 at a peak power of 83 TW. Particularly, filamentation became more severe as density was increased and was worse for $f/20$ focusing than for $f/10$. Note that for this setup, the plasma acts as a thick lens in

the imaging system. Therefore, mode images taken through plasma, where in vacuum object plane is in front of the cell exit, have uncertainty in the true object position. When the object plane is set to 6.6 mm behind the focus in vacuum, a shot with gas shows evidence of filamentation in the laser mode. With the vacuum object plane located 32.9 mm behind focus (Fig. 6.5)(still within the plasma), filamentation has fully developed, with filaments approximately the same size as the vacuum focal spot. Images of the mode with vacuum object plane at 32.9 mm are shown in the top row of Fig. 6.6. As P/P_{crit} is increased (density was increased intentionally and laser power fluctuated $\pm$ 5%), filaments developed with tighter dimension and increasing number.

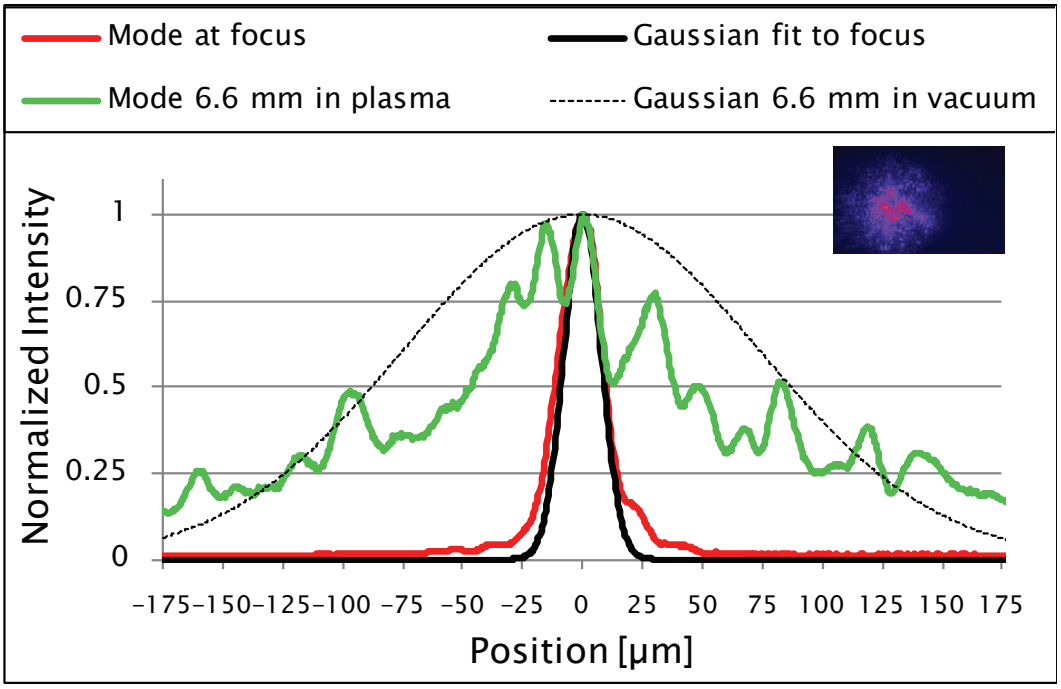

Figure 6.4: Transmitted laser spot ($f/20$) lineout with image plane initially set (in vacuum) 6.6 mm behind focus (green) as well as the reference curves described previously. Each curve is individually normalized and centered. Note the shape has flattened out and begins to show signs of filamentation.

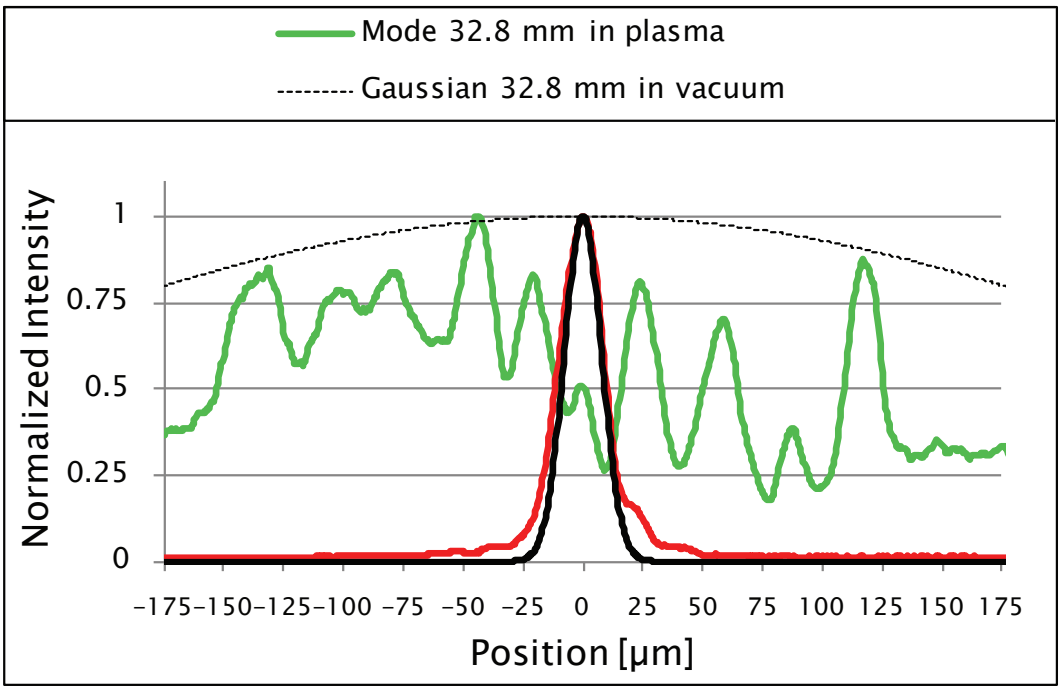

Figure 6.5: Transmitted laser spot ($f/20$) lineout with image plane initially set (in vacuum) 32.8 mm behind focus (green) as well as the reference curves described previously. Each curve is individually normalized and centered. Note the severe filamentation with spatial period approximately equal to the vacuum focal spot size.

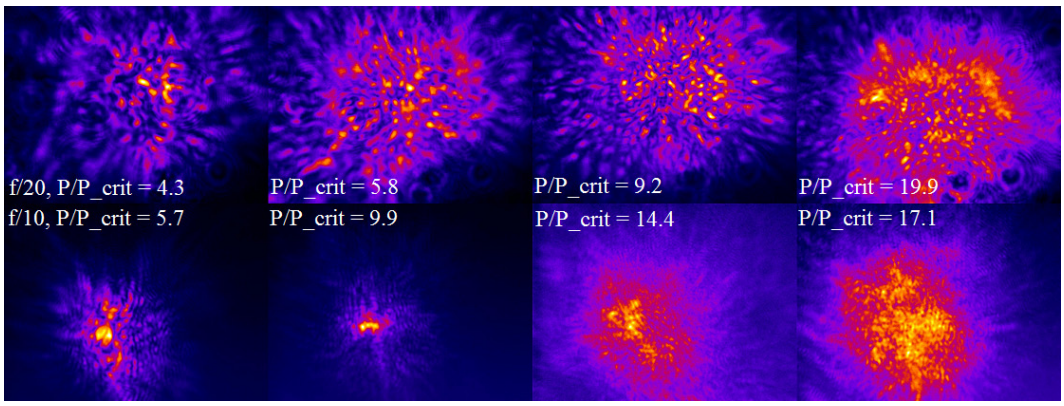

Figure 6.6: Laser profiles imaged within the plasma. Top row $f/20$ focusing with initial image plane 32.8 mm behind focus. Bottom row $f/10$ focusing with initial image plane 10.5 mm behind focus.

6.3.2 Channeling

While few laser modes were well guided using the $f/20$ focusing geometry, several modes using $f/10$ geometry were guided over at least 6.6 mm, especially in the density range $4.0 \times 10^{18} cm^{-2} \leq n \leq 6.0 \times 10^{18} cm^{-2}$ ($8 \leq P/P_{crit} \leq 12$). The vacuum focal spot in this geometry was 12 μm as shown in Fig. 6.7. The maximum peak intensity in these experiments was 9×10^{19} W/cm^2 at a peak power of 88 TW. Guiding is demonstrated all the way to the end of the 19 mm cell. For this shot, the exit guided mode includes two spots, each with $\sim$ 2% of the total energy within 9 μm of its peak, and each with peak fluence 0.5% of the vacuum peak fluence at focus, in spite of the estimated 12% transmission, which will be discussed later in this section. By comparison, a Gaussian beam would be expected to diffract in vacuum to 5.6×10^{-5} times the vacuum peak fluence at focus.

The transverse probe was used to produce shadowgrams of the interaction. Evidence of the filamentation and guiding observed in laser mode imaging can be seen in the shadowgrams. At high density, multiple filament streaks can be seen and these streaks disappear after just a few mm of propagation. At lower density, however, the streaks become a single channel feature which extends over the entire length of the field of view.

When the transverse probe was used for interferometry, the plasma can be seen. The plasma showed similar behavior to the filament features- the plasma existed over the entire length of the field of view at low density but existed over a short length at high density.

Transmitted laser spectra were taken using the same imaging system as the laser mode imaging diagnostic, though the image plane position was fixed. Spectra are integrated in the spatial axis over the inital width of the vacuum spot. The slit FWHM size corresponds to 5 pixels, or 1 nm. Fig. 6.10 displays transmitted spectra for several densities, starting with n_e =3.5x10^{18} cm^{-3} which was below the threshold for

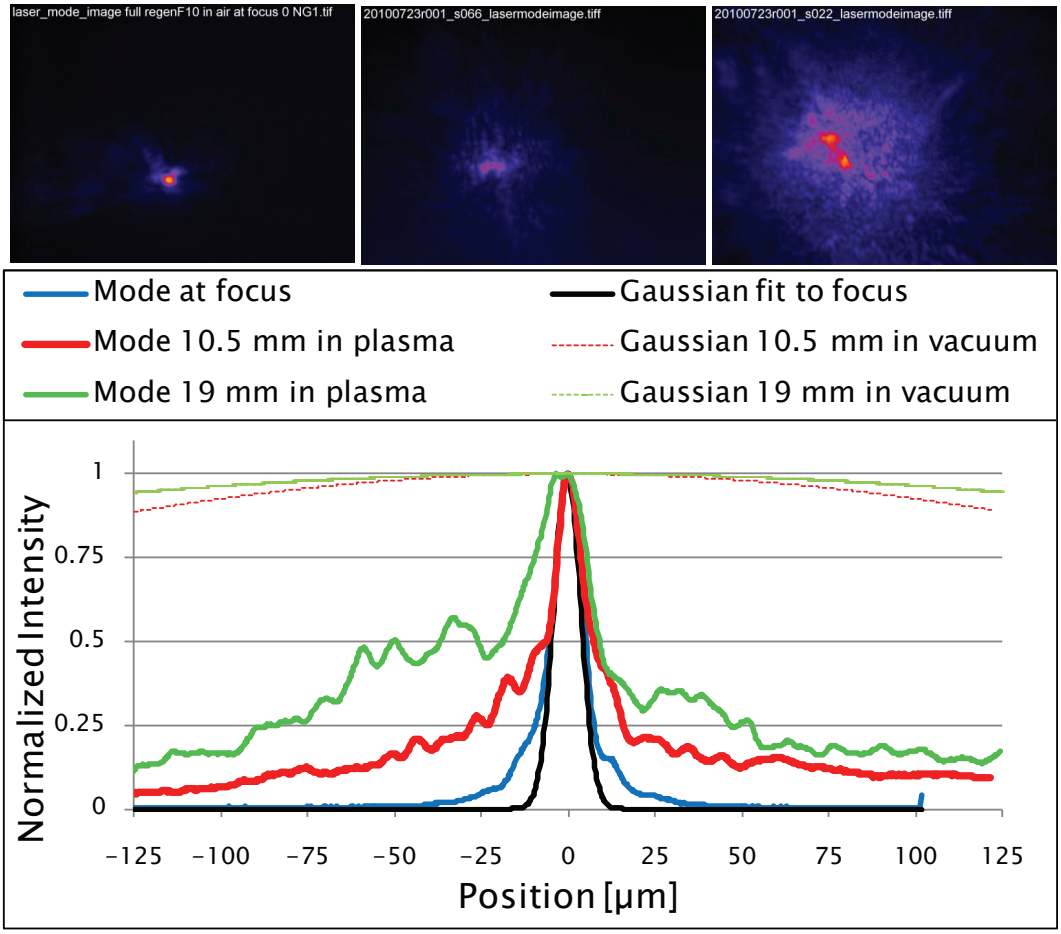

Figure 6.7: Images and lineouts of transmitted laser spots in $f/10$ focusing geometry at focus (left image, blue curve), 10.5 mm behind focus (middle image, red curve), and at the exit plane, 19.0 mm behind focus (right image, green curve), as well as the reference curves described previously. Each curve is individually normalized and centered.

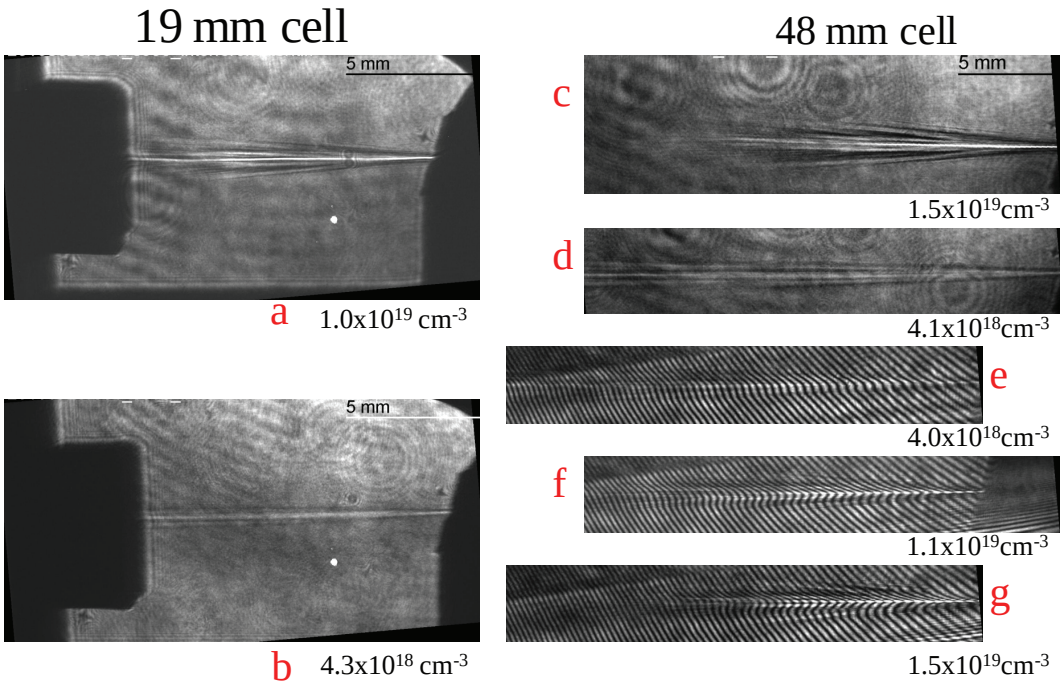

Figure 6.8: Transverse shadowgrams can indicate filamentation and rapid laser depletion (a, c, f, g) at high density or a single (presumably well-guiding) channel (b, d, e) at low density.

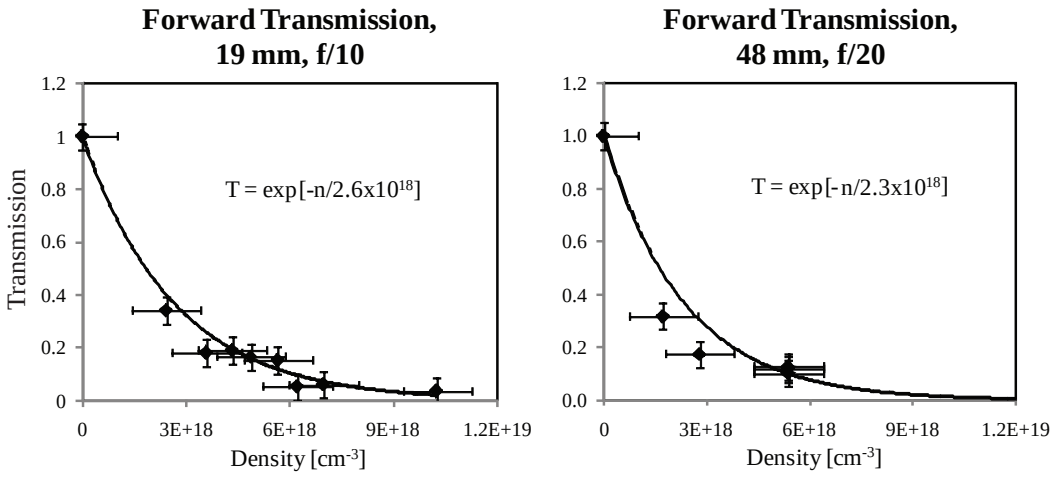

Figure 6.9: Laser transmission as a function of plasma density. Laser mode image is integrated and normalized to incident laser power.

injection ($n_e = 4\text{x}10^{18}\ cm^{-3}$), up to $n_e = 5.4\text{x}10^{18}\ cm^{-3}$. Each curve was normalized to its own peak avoiding obfuscation from the transmission as a function of density. This highlights changes in the shape of the spectra with density. The vacuum spectrum is shown in black, as are spectra taken at increasing densities from red to blue. Much of the laser energy remains within the original bandwidth, however an additional blue-shifted peak develops as well as bluer wings which diminish with increasing density. Strong red wings also develop and grow with increasing density.

Fig. 6.11 presents data in the same manner but taken with a gas mixture containing 2.5% (by pressure) nitrogen in helium. Note that in this case, both the blue peak and blue wings grow with increasing density which is the opposite of the case in Fig. 6.10. The red wings however display a similar relation to density as the pure helium case. This is the same behavior as in Fig. 5.8 from the ablative capillary experiment in which case the enhanced blue shift resulted from an increasing presence of ionizeable ablated wall material reaching the laser axis at later time. The enhancement in blue is due to a greater rate of ionization as discussed in Sec. 2.2.3.

Due to spatial constraints, the laser transmission diagnostics and electron spectrometer diagnostics could not be fielded on the same shot. All electron spectra obtained during the experiment demonstrated high energy spread. The reason this occurs can be understood by considering the dephasing length. For $n_e = 4\text{x}10^{18}\ cm^{-3}$, the dephasing length is 12 mm and the depletion length is 24 mm. Thus, acceleration in the 19 mm cell was affected by dephasing and the 48 mm cell acceleration was limited by laser energy depletion and also affected by dephasing. The result of interaction length $\gg L_{dephas}$ is electron energy broadening as electrons begin being decelerated in the front half of the bubble potential. The maximum energy observed with gas cells was $E = 436 \pm 24\ MeV$ with energy spread $\Delta E = 95\ MeV$. This shot was taken with 113 TW at a density $4.4\text{x}10^{18}\ cm^{-3}$.

The effect of gas mixtures used in the gas cell on the electron beam properties

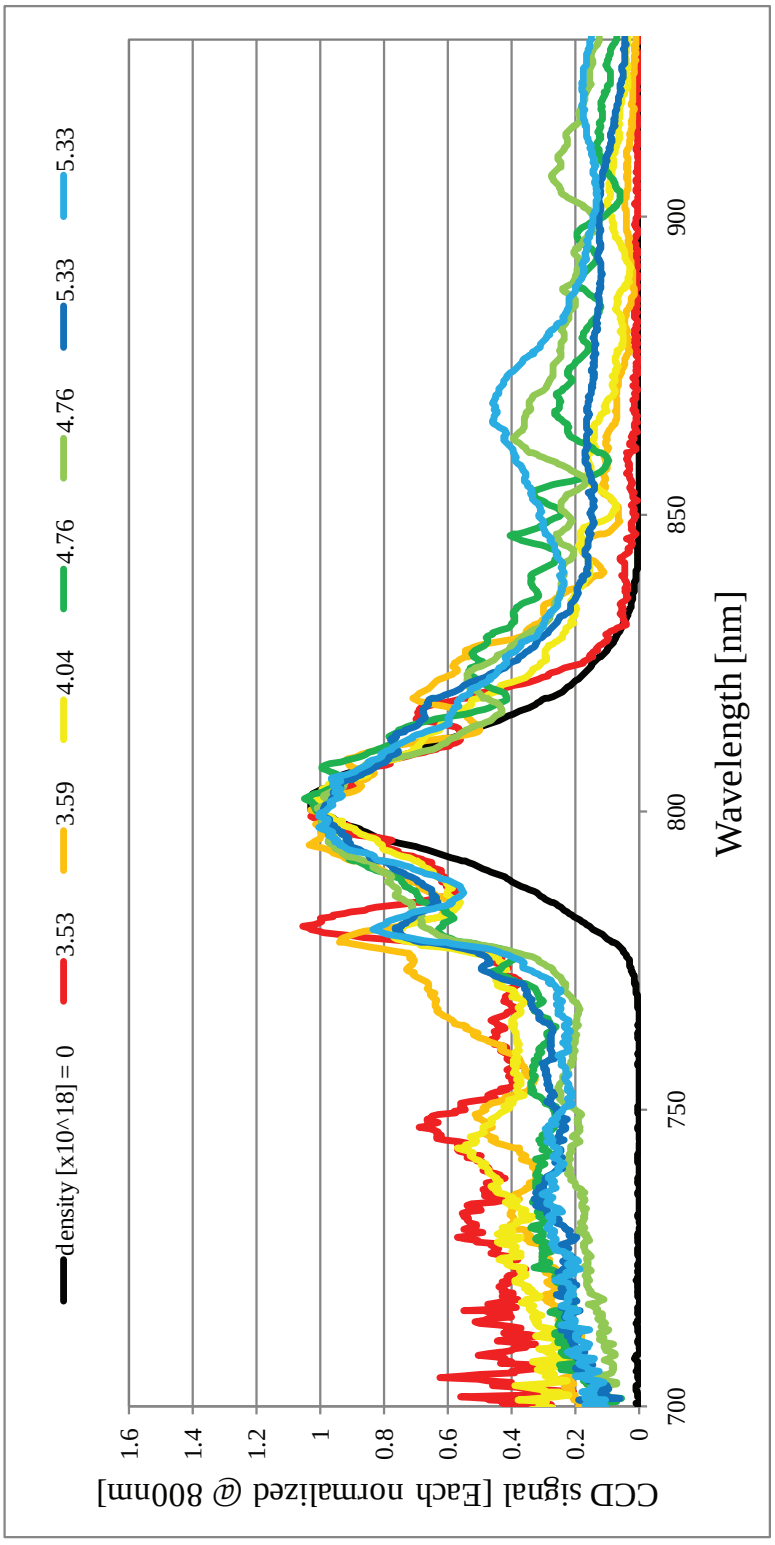

Figure 6.10: Transmitted laser spectra for shots taken at various pressures of pure helium.

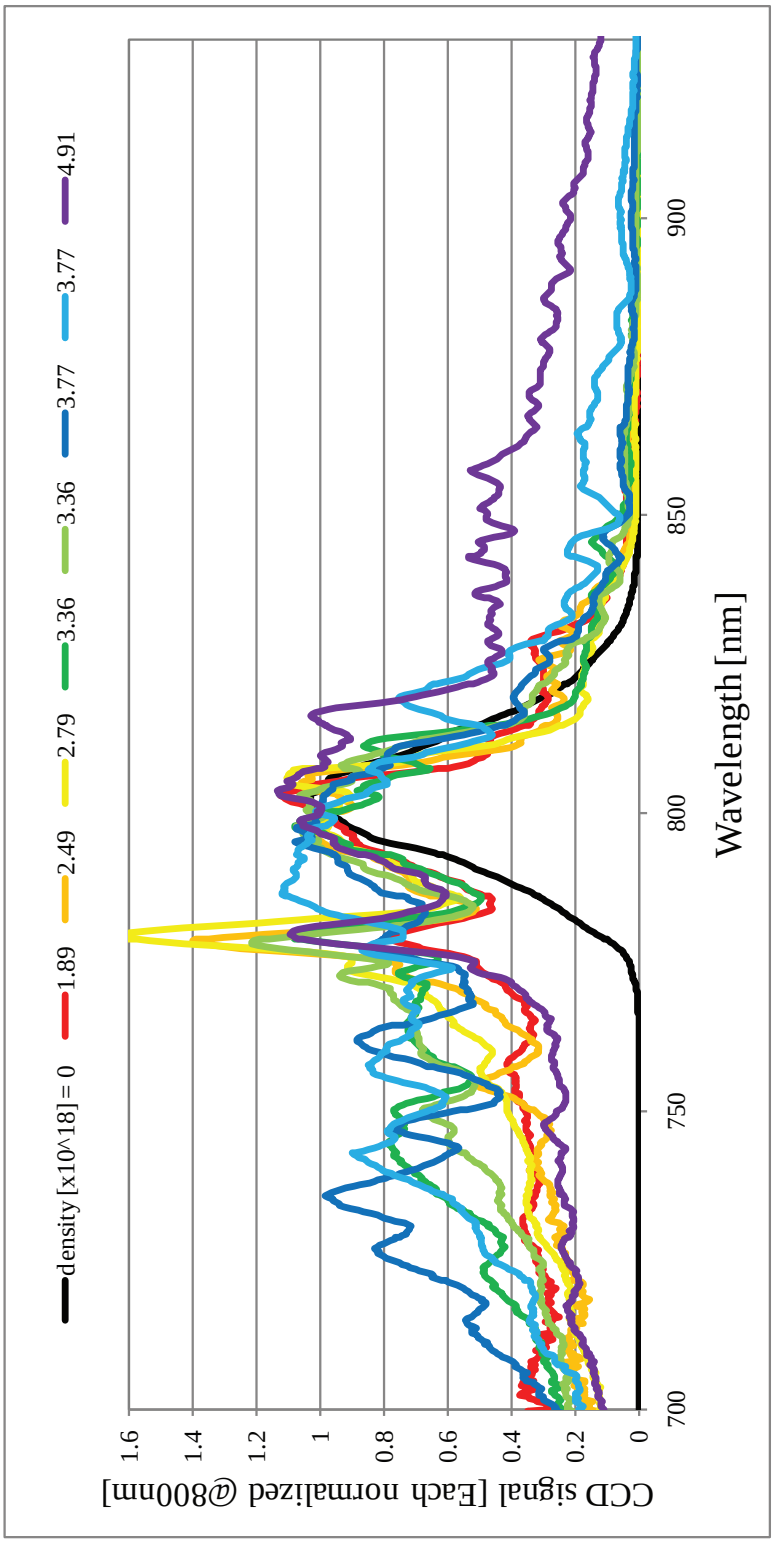

Figure 6.11: Transmitted laser spectra for shots taken at various pressures of nitrogen/helium (2.5%) mixture.

(higher charge, smooth beams) will be discussed in Sec. 7.4.

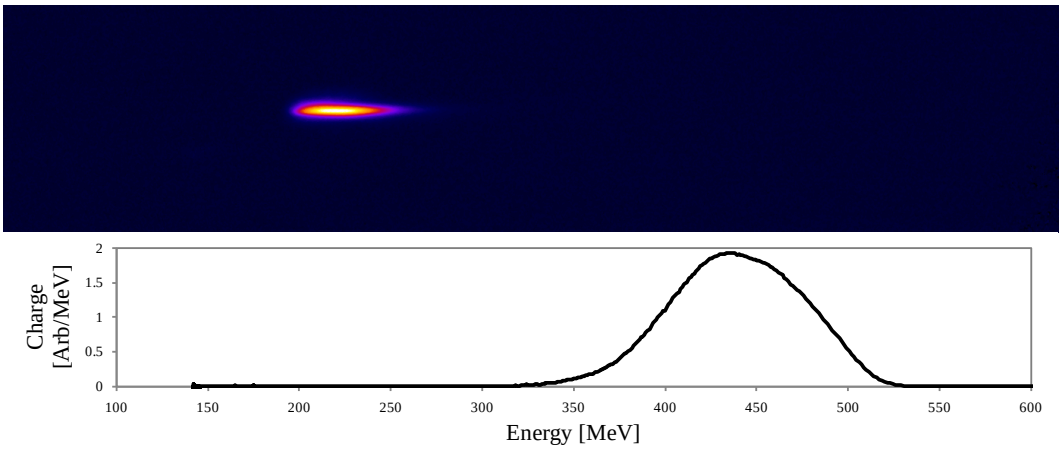

Figure 6.12: An electron spectrum taken with the 48 mm gas cell and $P = 113\ TW$ at a density 4.4x10^{18} cm^{-3}.

6.4 Conclusions

Self-guiding in these cells could not match the quality of guiding achieved in the ablative capillaries. The failure to consistently guide in $f/20$ focusing geometry may be understood by considering guiding to be a balance between diffraction and self-focusing. In the $f/20$ case, diffraction is weaker than in the $f/10$ case, allowing self-focusing and filamentation to dominate for nearly all cases where $P/P_{crit} > 1$. Furthermore, self-guiding required the additional constraint that $8 \leq P/P_{crit} \leq 12$ as guiding was inconsistent below this range and multiple filaments formed above this range. The inconsistency at low range is most likely due to the requirement that $P > P_{crit}$ throughout the entire length of the cell and the laser pulse loses energy through depletion. However, the degree of self-guiding observed is remarkable and unexpected for such a short pulse. This range of acceptable P/P_{crit} fortunately mandates a density which coincides with the density threshold for injection for the parameters of this experiment. This density range is optimum for producing high

energy monoenergetic beams. This means that if the density threshold falls at least as quickly as $1/P$, LWFAs will be able to operate with the same P/P_{crit} range which was self-guided in this study.

This study also highlights the importance of matching the accelerator length to the anticipated limiting length. The 19 mm cell was dephasing limited as anticipated and demonstrated in the electron spectra. The length over which the power falls below P_{crit} may have been the true limiting length in this experiment (similar, but not the same as the depletion length). The electron energy scaling in Ref. [81] predicts an energy of 658 MeV for the conditions at which we observed the highest energy, 436 MeV. The scaling assumes infinite guiding length, which suggests the imperfect guiding allowed the wakefield strength to diminish before L_{dephas} had been reached. An increase in power and decrease in density as discussed in the previous paragraph would drastically increase this scale length, due to higher pulse energy and higher transmission. These effects would predict that higher power lasers, such as the Texas Petawatt [166] may expect electron energy to scale with laser power. This laser will deliver 10× the power of HERCULES. If the focal spot can be chosen appropriately and produced with high enough quality the Texas Petawatt should be able to operate with nearly matched wakefield conditions and P/P_{crit} within the optimal range for self-guiding presented here.

CHAPTER VII

Ionization-induced Injection

7.1 Introduction

It has been shown experimentally that electrons born by field ionization by a high intensity laser can gain energy in excess of the ionization potential [48, 167]. In Ref. [168], Laser Wakefield Acceleration was proposed as a scheme using a second high intensity "injector" laser to field ionize electrons within the wake to initiate trapping. The electrons born by ionization receive a great deal of energy from the ponderomotive force, allowing easier trapping. This mechanism was investigated experimentally as described in this chapter. Recently, the method was expanded upon considering the additional imparted energy from above threshold ionization from a circularly polarized injector pulse [169]. A related ionization trapping mechanism was demonstrated in electron beam driven plasma wave accelerator experiments at the Stanford Linear Accelerator Center (SLAC) [170]. Ionization induced trapping was also inferred in experiments on laser wakefield acceleration in a capillary due to relatively high Z ions from the walls migrating to the laser axis [153]. Creation of free electrons by ionization, initially at rest within the electron cavity, can initiate trapping because these electrons experience additional energy gain due to the net potential difference between the edge of the bubble and its interior. Additionally, electrons may be born within a higher laser field than could be reached by preionized

electrons, causing additional momentum transfer from the ponderomotive force and the laser fields themselves. This translates to a lowered trapping threshold, and is maximized if the electrons are initiated at the minimum of the potential.

This chapter presents the findings in [171] which were conducted with up to 30 TW in the spring of 2009 as well as subsequent findings at 100 TW in the spring of 2010. The initial publication was concurrent with similar findings in Ref. [172]. Figs. 7.2, 7.3, 7.4, and 7.9 reprinted with permission from [171].

7.2 Experimental Setup

Presented here is the first experimental demonstration of electron trapping initiated by ionization in a laser wakefield accelerator. We show that this mechanism increases the trapped charge by up to an order of magnitude and decreases the emittance of the electron beam generated. A range of noble gases, and nitrogen, is systematically added as a small percentage to helium gas. It is determined that optical field ionization of inner shell electrons of the higher Z gas plays an important role in moderating the trapped charge. Although there is a small increase in electron number density due to the higher Z gas additive, it is shown to be insufficient to account for the increase in charge in the trapped bunch. In addition, the behavior of the trapping is consistent with the field-ionization thresholds for the various gas species added to the helium. Improvements in beam charge and emittance are important for applications such as x-ray generation through inverse Compton scattering, or free electron lasers, as well as x-ray generation by oscillation in a plasma based wiggler. By using a gas mixture, lower power laser systems can be used to generate higher charge, higher energy, and decreased emittance monoenergetic electron beams than can be produced using a fully pre-ionized plasma.

In these experiments, pulses from the Hercules laser system [121] at the Uni-

versity of Michigan (30 $fs, 800$ nm Ti:sapphire) were focused using an $f/10$ off-axis parabolic mirror onto the edge of gas flow from a 3 mm diameter conical supersonic nozzle. The laser wavefront was corrected with a deformable mirror, yielding a focused spot of 10 μm full-width-half-maximum (FWHM). The experiments were conducted using a laser peak power ranging from $24-120$ TW on target. The focused peak intensity was $I = 3.5 \times 10^{19}$ Wcm^{-2} at 30 TW and $I = 1.5 \times 10^{20}$ Wcm^{-2} at 120 TW. Diagnostics in the forward direction included an electron spectrometer (0.8 T permanent magnet, Lanex phosphor screen, and CCD camera) with electron energy detection range of $47 - 800$ MeV, transmitted laser mode imaging, and transmitted laser spectrum. A transverse probe beam was used for transverse interferometry. Sidescattered light from the plasma was split with a wedge and sent to an imaging CCD as well as a spectrometer with 260 nm spectral window centered around the laser wavelength. Gas was pulsed from a solenoid valve (5 ms opening time) through the gas nozzle. Gases added to the helium target included air, nitrogen, neon, argon, krypton, and xenon.

To ensure a homogeneous mixture, the gases were agitated in a 2.5 l steel vessel. The vessel and all gas lines were evacuated before introducing any gases. Care was taken to eliminate leaks in the lines. In order to accurately produce low additive to helium ratio mixtures, the gas additive was introduced using a low pressure regulator (typically < 4 atm) first, and subsequently helium was added at high pressure (67 atm) from an isolated supply. A third regulator was installed on the output of the mixing vessel, maintaining constant pressure for many tens of shots with the same gas mixture. Before a typical experimental run, air contaminant can be introduced into the gas as a result of changing regulators or gas bottles. However for these experiments many gases were installed on a manifold so that air would not be introduced when changing gases. A density scan was conducted with each gas mixture ratio for a number of different ratios of additive to helium, between 0:1 and 5:95 by partial

pressure. The gas mixture ratios are defined by the absolute pressure of the gas additive relative to the absolute pressure of helium. Electron plasma densities in the range $5 \times 10^{18} - 3 \times 10^{19}$ cm^{-3} were investigated.

7.3 Experimental Results at 30 TW

7.3.1 Plasma Density Measurement

Electron number density was monitored via both transverse interferometry and Raman-shifted side-scattered light. For each 1% increase in additive mixture of a gas with n electrons which can be ionized the electron density will increase by $(n-2)\%$ relative to helium gas at the same pressure. Electron densities quoted in this paper are calculated according to the above discussion, as some interferometry images were blinded by sidescattered light particularly when laser power was > 100 TW. In these instances Raman-shifted scattered light provided a secondary measurement of electron density. Both measurements were shown to agree with the calculated electron density within the uncertainties of the gas pressures as shown in Fig. 7.1.

7.3.2 Beam Charge

Certain gas mixtures significantly improved the probability of injecting electrons and also increased the amount of charge in the electron beam relative to pure helium. However, it is important to accurately diagnose the exact electron number density in the interaction with the higher Z additive. Strong sidescatter was always emitted only throughout the first $400 - 500$ μm (approximately one Rayleigh range) of the plasma. With higher power shots (> 100 TW) sidescatter was emitted further into the plasma. The wavelength of the scattered light was observed to be shifted to the red of the initial laser wavelength, λ_0, according to $(\Delta\lambda/\lambda_s)^2 \propto n_e$, where n_e is electron number density, λ_s is the redshifted wavelength and $\Delta\lambda$ is $\lambda_s - \lambda_0$.

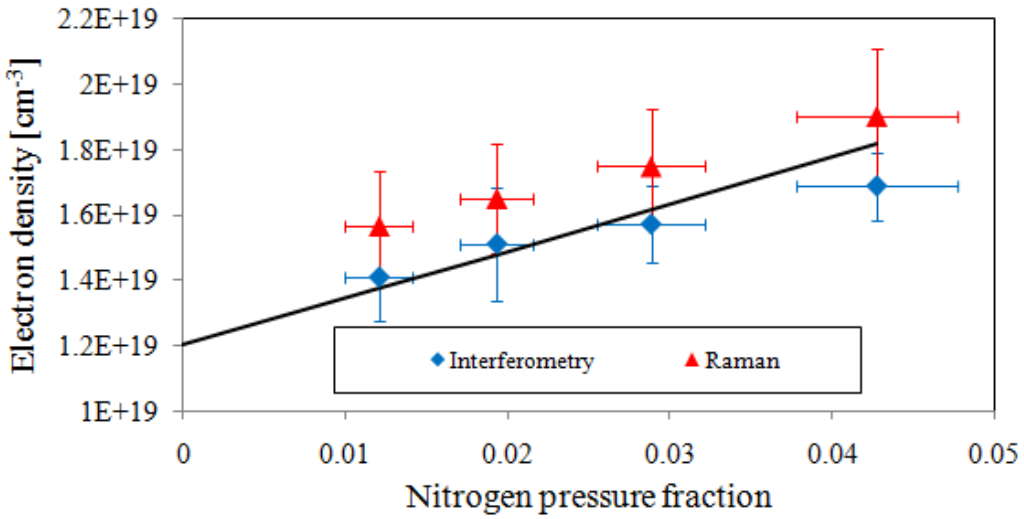

Figure 7.1: Comparison of electron densities as measured by interferometry and Raman side-scatter to a calculation of the expected density. Gas pressure is held fixed but the ratio of nitrogen in the gas mixture is varied.

The effect of gas additives on beam charge is shown in Fig. 7.2. In shots using 30 TW laser power, a nitrogen additive consistently led to an increase in the total integrated charge of almost an order of magnitude compared to a pure He target with equal electron density, Fig. 7.2a. For example, the first data point on the series labeled He + N_2 in Fig. 7.2a includes data from shots at 30 TW containing 1.2% N_2 and 98.8% He by pressure at a total pressure of 150 $PSIg$. For these parameters, a beam with 30 pC was produced, whereas shots on pure He at 175 $PSIg$ produced only beams with charge at or below detection level. Using a slightly lower power of 24 TW, argon also showed a substantial charge increase, Fig. 7.2b. Neon and other higher Z gas additives consistently decreased the beam charge in all cases at 30 TW, Fig. 7.2c. At 120 TW, using neon, an improvement in the mean trapped charge compared with helium was recorded, Fig. 7.2d. More interestingly, this behavior was significantly different from the 30 TW case, Fig. 7.2c.

Adding too much higher Z gas, of any species, was also found to be detrimental to electron injection, also due to ionization defocusing (for example, Fig. 7.2b, far right).

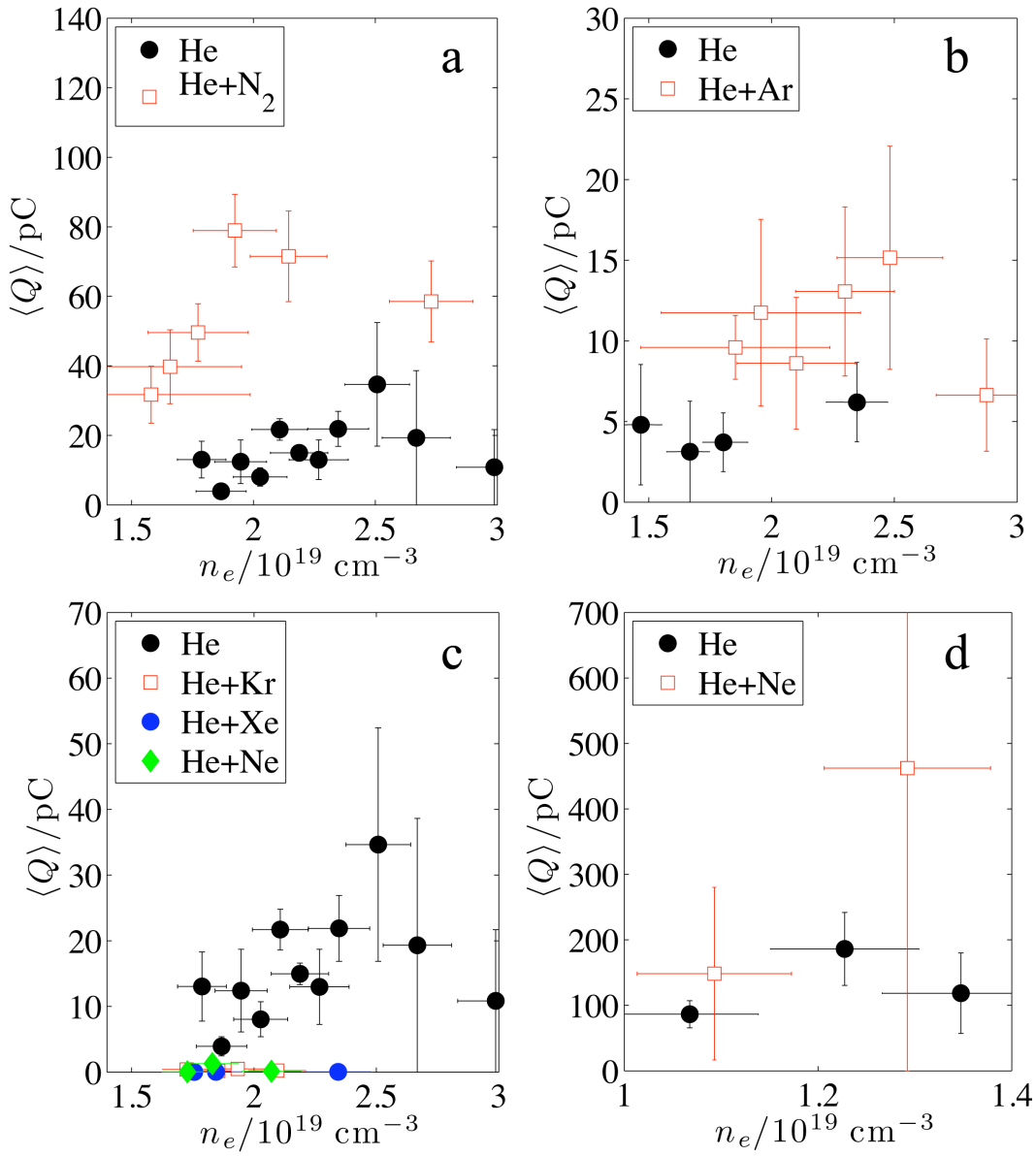

Figure 7.2: Integrated charge above 30 MeV measured by the electron spectrometer as a function of electron number density. The values represent an average of 5-20 shots for which electron signal is clearly above background. For gas mixtures the electron density increase is due to a change in the proportion of additive to helium while the total gas jet backing pressure is held fixed; for pure helium the electron density increase is due to an increase in backing pressure of pure helium gas. The experiments were performed with a laser power of (a) 30 TW, (b) 24 TW, (c) 30 TW and (d) 120 TW

Xenon has four states which are ionized at lower intensity than neutral helium. The balance of ionization seeded injection and ionization defocusing creates a window of gas additive mixture ratios over which electron injection is enhanced. The mixing chamber apparatus allowed for systematic control necessary for this study. However, by merely exposing the gas lines to a small quantity of air before filling with helium, results similar to the nitrogen additive run were achieved.

7.3.3 Electron Spectra and Profiles

Typical electron spectra obtained on the experiment are shown in Fig. 7.3. Panel (a) shows typical He and He+N_2 spectra superimposed, to demonstrate that the increase in charge is not at the expense of mean energy, for otherwise identical conditions. Figs. 7.3b and c show electron spectra obtained with argon and neon additive respectively, which are clearly quasimonoenergetic. The mean energy of the electron beams produced by ionization trapping was measured to be the same, within statistical error, as from those produced by self-trapping in helium only. This is to be expected, as ionization should not significantly modify the bubble structure due to the bulk of electrons being pre-ionized in all cases studied.

The beam divergence was measured by imaging a Lanex screen placed 1 m behind the target with the magnet removed. Typical profiles are shown in Fig. 7.4. The mean divergence in the vertical direction was 5.1 ± 1.0 mrad, averaged over 5 shots for the case of pure helium and 2.9 ± 0.8 mrad averaged over 8 shots for He + 1% Ar. The integrated charge from the shots with Ar additive was, on average, twice that of shots with pure He. There is also a clear qualitative difference between the profiles in the two cases. Although not a measure of the transverse emittance of the beam, it can be inferred that the increased collimation of the beam corresponds to an improved emittance, if a comparable source size is assumed.

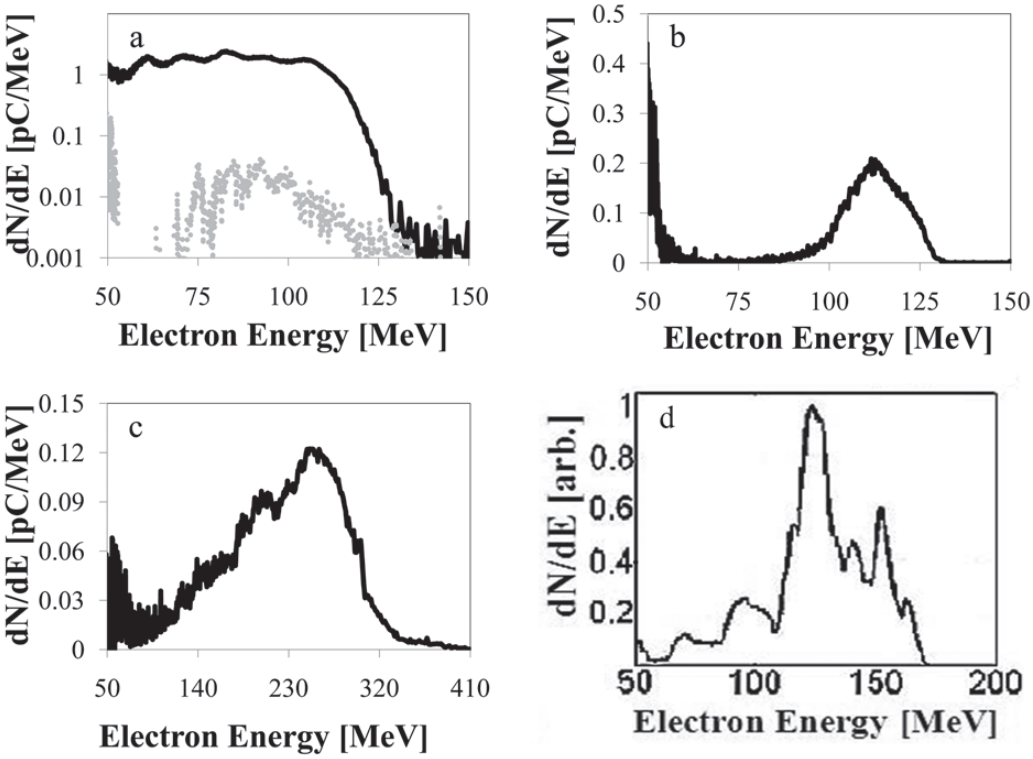

Figure 7.3: a) Electron spectrum from a 30 *TW* shot with a target of pure helium (grey) is enhanced greatly by a mere 1% N_2 additive (solid black), while the charge-weighted average energy remains the same. *Note in this particular graph the scale is logarithmic.* The beam can be reasonably monoenergetic at an appropriate density for both the pure He and N_2 cases. b) Monoenergetic spectrum from a 24 *TW* shot with 1% Ar additive. c) Spectrum from a 120 *TW* shot with 1% Ne additive. d) Spectrum from particle-in-cell simulation of 30 *TW* shot with a target of He + 5% N_2.

7.4 Experimental Results at 100 TW

7.4.1 Electron Spectra

In 10 mm gas jet experiments at 100 TW, the effect of ionization on electron beam generation was observed. The gas mixture used in all shots during this experiment was $P_{nitrogen}/P_{helium+nitrogen} = 2.5\%$, which was the optimal mixture found from the 30 TW experiments. As in the 30 TW case, nitrogen additive increased the average electron beam charge as compared to pure helium at the same electron density. Additional trends in the data can be observed in Fig. 7.5 which shows data from six characteristic shots:

- The injection threshold density is lower for gas mixtures by as much as 50%.
- Beam divergence is density dependent, with high divergence sprays of electrons seen with high density gas mixing targets and low divergence beams seen at low density. The high divergence observed at high density with gas mixing causes smearing (uncertainty) in the energy dimension.
- Fine structures observed from pure helium shots are absent when gas mixing targets are used. Instead the beams from a gas mixture targets typically appear smooth. This smoothing occurs even for shots with electron density above the threshold for injection in pure helium targets, suggesting that electrons born from ionization of high charge states become trapped, taking the place of electrons that would have been trapped by conventional self-injection.
- Electron spectra from gas mixing targets are typically broad, though monoenergetic spectra have been observed on shots taken near the injection threshold. Recall that the characteristic high divergence spray at high density obfuscates the detection of monoenergetic beams.

In 4.8 mm gas cell experiments at 100 TW, the average beam charge from gas mixture targets was greater than that for pure helium targets at the same electron density by as much as a factor of 4. Fig. 7.6 shows the gamma ray signal detected by a scintillator for 428 shots at various experimental parameters including both pure helium and gas mixing targets. The gamma ray signal is an indirect indicator of high energy electrons, where the signal is presumed to increase with increasing charge of electrons with enough energy to generate penetrating bremsstrahlung radiation. This plot recapitulates the decreased injection threshold density from ionization induced injection found in the electron spectrometer data.

7.4.2 Effect on Betatron Radiation

Betatron radiation was measured using the Andor CCD [141]. The betatron total energy flux was generally higher when gas mixing was used as compared with pure helium targets at the same density taken with a 10 mm gas jet (Fig. 7.7). No clear conclusion about the betatron flux can be drawn from the smaller dataset taken with a 19 mm gas cell (Fig. 7.8). Select shots were also recorded in single hit regime allowing the spectrum to be measured. Spectra, including shots taken with gas mixing, were presented in Fig. 4.11. However, no clear distinctions can be made between the betatron spectra taken with and without gas mixing due to the limited dataset which can be considered to be in the single-hit regime.

7.5 Computational Modeling

To analyze the effect of the ionization dynamics on trapping mechanisms and acceleration of trapped electrons, the two dimensional particle-in-cell code PICNIC was used. The computations were performed and analyzed by V. Yu. Bychenkov, I. V. Glazyrin and A. V. Karpeev. In the code, field ionization is accounted for using the Ammosov-Delone-Krainov model [47]. The energy loss to ionization of atoms

from the fields is accounted for in Maxwell's equations through an energy balance expression. All electrons are tagged based on the ionization state from which they originate. In a typical run, the spatial grid has 16 cells per laser wavelength, and 20-30 macroparticles per cell.

Numerical calculations were performed for conditions similar to those of the 30 TW experiment, in a gas density of 10^{19} cm^{-3}. Computational runs were performed for: i) a fully ionized helium plasma; ii) helium gas including field ionization; iii) a mixture of 95% helium and 5% nitrogen, including field ionization. There are no significant differences between cases 1 and 2, since helium is expected to be fully ionized at approximately 10^{16} Wcm^{-2}. For case iii) it was found that the spectrum includes a high-energy electron bunch which has a peak around 120 MeV after 500 μm propagation, Fig. 7.3d. This bunch originates from field ionization of N^{5+} and N^{6+} ions. Fig. 7.9 shows the spatial distribution of electrons near the bubble at $t = 1.0\ ps$. In this simulation, these electrons appear through ionization of N^{5+} and N^{6+}, which are ionized primarily in the proximity of the peak of the laser pulse. However, of the electrons from these ionization states, the ones which eventually become trapped all originate slightly off-axis. They then flow into the acceleration region off-axis, as shown by arrows in Fig. 7.9. Acceleration terminates at 1.5 ps. The total electron beam charge in the case of pure He is 0.57 nC, and 0.83 nC in the case of He+N_2, in which the electron charge due to He is 0.47 nC. From the He plasma the number of high-energy electrons (with energy $>$ 100 MeV) was two orders of magnitude less than from He+N_2 plasma.

At 1.0 ps, the bubble is elongated, as seen in Fig. 7.9. Electrons from helium move along the bubble periphery and reach the region of accelerating field located near axis, at a distance of (50-55) λ_0 from the laser pulse,with typical trajectories shown by arrows (i) in Fig. 7.9. Electrons produced via field ionization of nitrogen from neutral gas up to N^{4+} move in a similar manner as these states are ionized early

in the pulse. However, electrons from ionization of N^{5+} and N^{6+} behave differently, with typical trajectory indicated by arrow (ii) in Fig. 7.9. They are born in the region of strong focusing magnetic field and result in a jet with large current density (more than 10 times the current density of electrons from helium). It was also found in the simulation that the addition of nitrogen improved the collimation of the electron beam by approximately a factor of 2 which agrees with the experimental results.

7.6 Conclusions

These results can be understood by consideration of the optical field ionization thresholds for the different species [54]. Both nitrogen and argon have a number of L-shell or M-shell electrons with a field ionization intensity threshold of $I_{BS} < 10^{17}$ Wcm^{-2}, and can be considered pre-ionized before the formation of the bubble.

However, the K-shell electrons for nitrogen have a threshold intensity for ionization of $I_{BS} \approx 10^{19}$ Wcm^{-2}, and so the majority of these electrons will be freed near the peak of the pulse. Likewise, the L-shell of argon has eight electrons with ionization threshold intensities ranging from $10^{18} \lesssim I_{BS} \lesssim 10^{19}$ Wcm^{-2}, and so a proportion of the electrons are expected to be freed near the peak of the pulse. Xenon and krypton have large numbers of outer shell electrons at low ionization thresholds that presumably cause ionization defocusing of the pulse and prevent stable wakefield formation, which could be observed in interferometry images. Krypton has almost double the number of electrons as argon below an ionization threshold of $I_{BS} < 10^{18}$ Wcm^{-2}. Neon has an L-shell which is fully ionized below an ionization threshold of $I_{BS} < 10^{17}$ Wcm^{-2}, but its K-shell is ionized at close to $I_{BS} \approx 10^{20}$ Wcm^{-2}, which is significantly higher than the peak intensity of the laser at 30 TW. This explains the different behavior of neon additive at 120 TW vs. 30 TW. For the case $a < 1$ where a is the normalized vector potential the bubble electric field is very small and for $a > 1$ the peak bubble field scales like $(\lambda_0/\lambda_p) * E_L$ where λ_p is

the plasma wavelength and E_L is the peak laser field, and so is likely 20 or 30 times less than E_L in our experiments. The intensity and species dependent increase in charge is a strong indication of an ionization trapping mechanism with ionization by the laser field.

In conclusion, ionization induced trapping in a laser driven wakefield accelerator has been systematically investigated by exploring the parameter space of atomic number and impurity concentration. The addition of a higher Z additive has been shown to increase the trapped charge and lower the transverse emittance of the generated electron beam as compared to pure helium at the same electron density. This should be a useful trapping mechanism for efficiently producing electron beams where stringent constraints on the beam emittance and charge are required such as x-ray production in a plasma or conventional wiggler, as well as to control the injection mechanism. Ionization injection has also recently been used in LWFA experiments with up to 200 TW laser power resulting in the highest electron energy to date [98], and further computational analysis has been conducted [66].

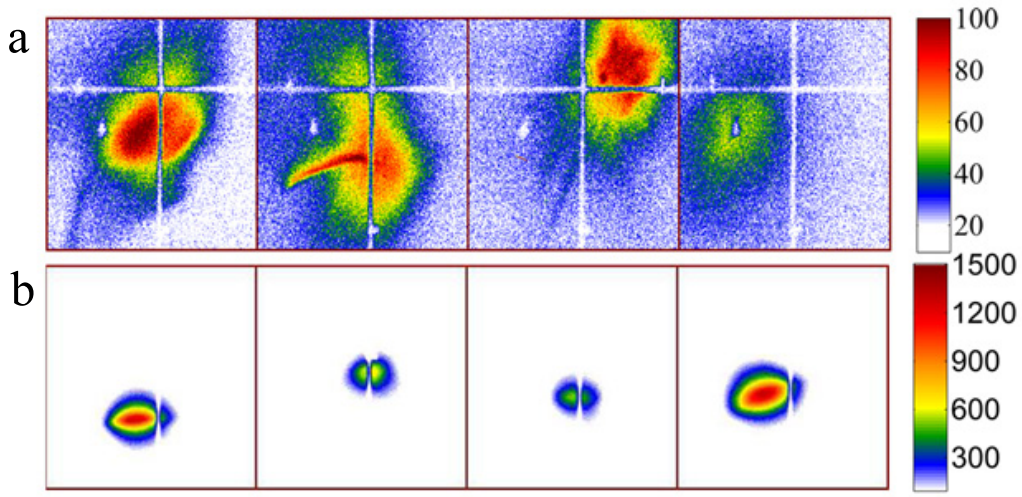

Figure 7.4: Electron beam profiles measured on a Lanex screen 1 m from the target. The top four images, (a), are from shots with pure helium and the bottom four, (b), are from shots with a 1% argon additive, both at equal electron number density $n_e = 2 \times 10^{19}$ cm^{-3}. *Note the difference in color scale, which represents electron signal [arb] per pixel.*

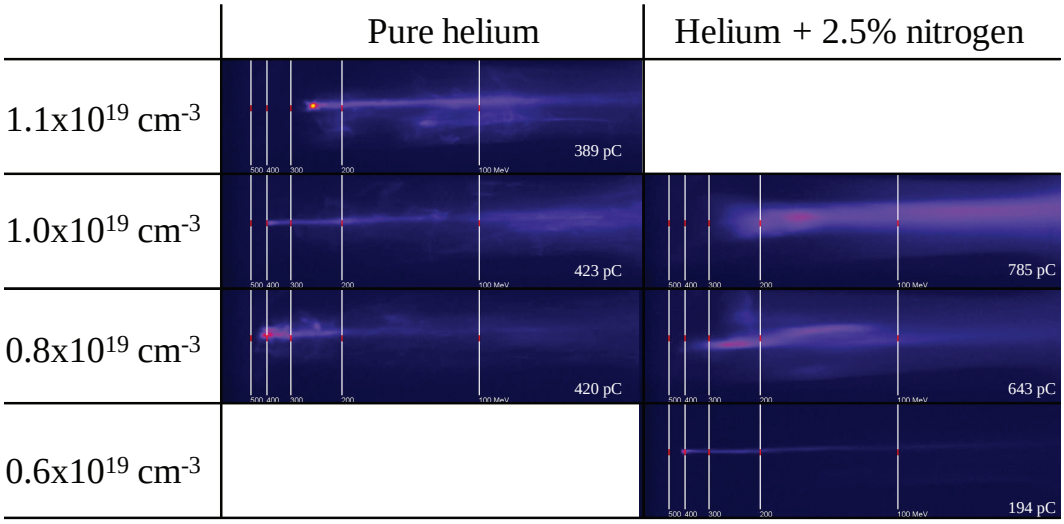

Figure 7.5: Example electron spectra demonstrating key effects of ionization injection including increased charge, decreased injection density threshold, beam smoothing, and density-dependent divergence. The horizontal dimension indicates energy with white vertical bars marking 100, 200, 300, 400, and 500 MeV from right to left. The vertical dimension indicates transverse divergence, where the red bar shows 10 $mrad$.

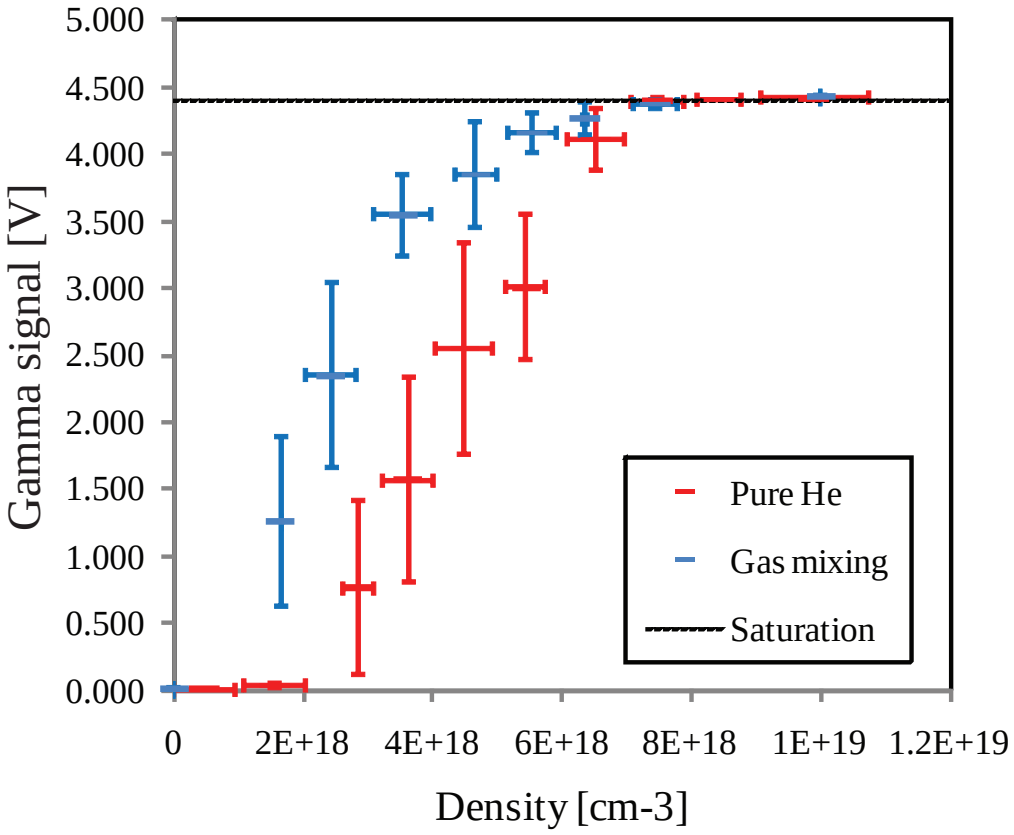

Figure 7.6: Gamma emission with and without gas mixing as a function of density as detected by a scintilator 2.5 m from the interaction with 8″ of lead shielding. Data were arranged into bins based on density, where the range of each bin is indicated by horizontal error bars. The data points show the average gamma signal for shots in each bin with vertical error bars spanning one standard deviation of the shots in each bin. The detector saturates at 4.4 V. Electrons were detected on 104 out of 110 shots for which the gamma signal was above 4.000 V.

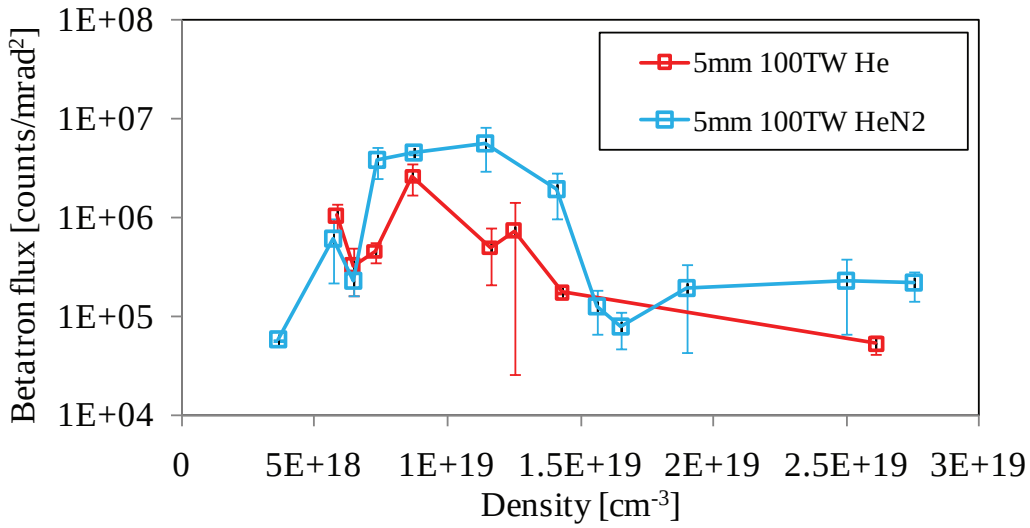

Figure 7.7: X-ray emission integrated flux with and without gas mixing as a function of density as detected by an Andor CCD 2.79 m from the entrance of a 10 mm gas jet. Data points show the flux averaged over 2-12 shots at the same density. Vertical error bars enclose one standard deviation of those shots.

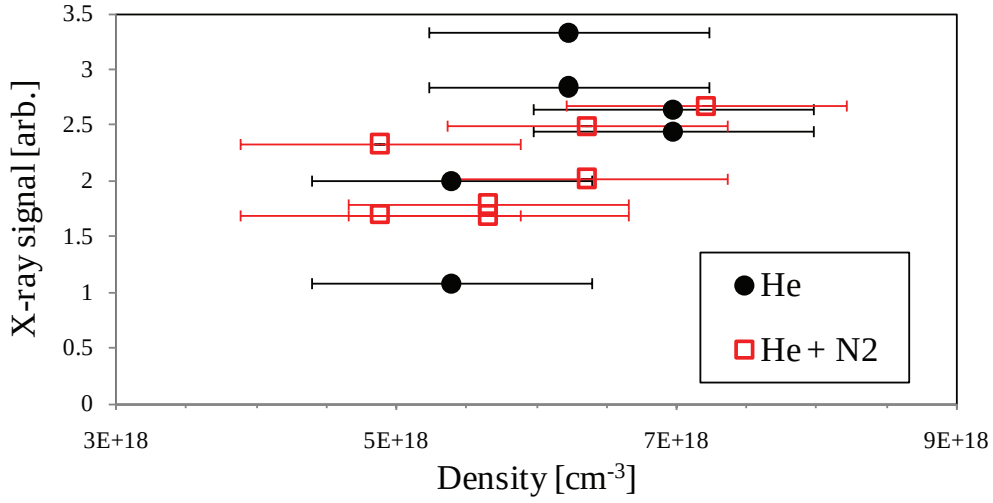

Figure 7.8: X-ray emission integrated flux with and without gas mixing (single shots) as a function of density as detected by an Andor CCD 1.5 m behind the entrance of a 19 mm gas cell

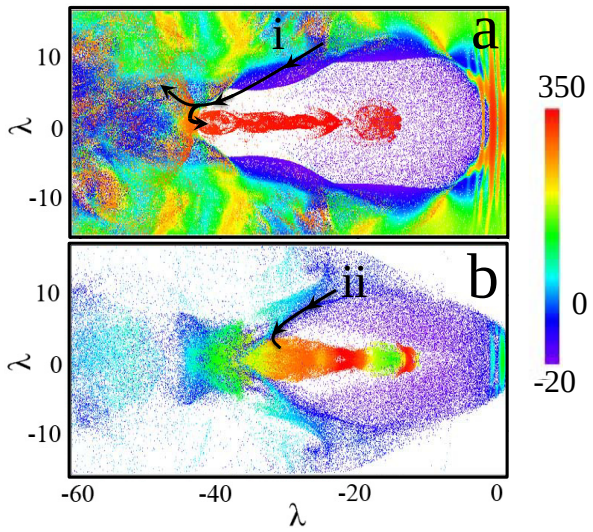

Figure 7.9: Electrons from ionization of (a) He and N through N^{4+}, (b) N^{5+} and N^{6+}. Color represents the longitudinal normalized momentum of the electrons. The spatial coordinates are in units of λ_0. The arrows are a schematic representation of electron trajectories taken from the time series data, (i) He and N through N^{4+}, (ii) N^{5+} and N^{6+}.

CHAPTER VIII

Summary of Sources and Conclusions

8.1 Discussion

The experimental conditions and electron beam parameters found during the experiments within this thesis are summarized in Table 8.1.

At lower density, laser depletion and dephasing limitations can be extended. Alternative injection methods such as ionization injection, colliding pulses, and plasma density manipulation can lower the density threshold for injection by perhaps 50%. If laser power is increased and the resulting lowering of the injection density scales at

	10 mm jet	19 mm cell	30 mm capill.
Laser power $[TW]$	128	113	35
Guided length $[mm]$	unknown	19	30
Injection threshold n_e $[10^{18}\ cm^{-3}]$	5.1*	4.0*	N/A
Electron E_{max} $[MeV]$	$> 550 \pm 50$	436 ± 28	N/A
Monoenergetic electron E_{max} $[MeV]$	410	275	N/A
Minimum $\Delta E/E$ [%]	5.1	6.6	N/A
Maximum Charge $[pC]$	966*	unknown*	N/A
Divergence $[mrad]$	3.5	1.7	N/A

Table 8.1: Summary of parameters achieved during campaigns described in this thesis. *Achieved with ionization injection

least as $1/P$, these limitations can be partially mitigated. Additionally, the parameter P/P_{crit} can be held the same as in the case of the self guiding presented here. In order to remain consistent with requirements for the bubble regime, these lasers will need to be longer in duration. In fact, it may be preferred to use bandwidth limited pulses with duration $> 300\ fs$ rather than stretching shorter laser pulses because the stretched pulses can self-compress and steepen more, making self-guiding more difficult.

These experiments were setup mostly in $f/10$ focusing geometry, which allows for a higher intensity than $f/20$ but slightly mismatched conditions for acceleration in the bubble regime. At 200 TW, operation in $f/20$ geometry should allow injection at the density required for exactly matched conditions resulting in less laser loss and higher electron energy gain. The anticipated energy gain of these experimental parameters is 1.1 GeV according to the "bubble" scaling [81]

$$\Delta E \cong \frac{2}{3}mc^2\left(\frac{n_c}{n_e}\right)a_0 \cong 1.7[GeV]\left(\frac{P[TW]}{100}\right)^{1/3}\left(\frac{10^{18}}{n_p[cm^{-3}]}\right)^{2/3}\left(\frac{0.8}{\lambda_0[\mu m]}\right)^{4/3} \quad (8.1)$$

8.2 Efficiency and Comparison to Existing Technologies

Compared to electron beams from RF accelerators, LWFA beams described in this thesis have the same maximum charge per pulse (nC), at least an order of magnitude greater energy spread, and higher divergence, smaller source size, resulting in a comparable emittance. The LWFA can accelerate electrons by 200 MeV in just 3 mm which would require a 2 m high quality linac. The major parameter which lags behind conventional accelerator technology is the repetition rate. Supersonic expansion used in gas jets requires a larger mass of gas than a gas cell achieving the same plasma density, thus requiring pumping time between shots. The backing pressure required for a circular oriface nozzle increases approximately as the square of

the diameter. This suggests that the relatively simple gas jet may be appropriate for LWFA to MeV-range beams at $kHz+$ repetition rate, but higher power laser systems with lower repetition rate attempting to achieve high energy gain LWFA may not be able to take full advantage of the repetition rate if a gas jet is chosen. Subsonic nozzles could alleviate the vacuum load, but at the expense of a flat density profile. Gas-filled capillaries and cells can already be operated with continuous gas flow.

The betatron radiation described in Sec. 4.3.4 has peak spectral brightness and spectrum similar to 3rd generation undulator facilities as shown in Fig. 8.1. The betatron compares favorably to conventional sources in terms of peak spectral brightness, pulse duration, and source size. The betatron's average spectral brightness, however, is much lower due to the low repetition rate. Table 8.2 summarizes the betatron source parameters and compares to existing and planned light sources.

Energy efficiency is a drawback for LWFA in comparison to conventional accelerators. The wall energy efficiency of flashlamp-pumped lasers similar to the HERCULES pump lasers is typically $< 10\%$. Frequency conversion, compression losses, and beam transport losses account for another order of magnitude decrease in efficiency. The energy in the laser pulse delivered to the target is transfered to the wakefield and then to the beam particles. One of the energy loss mechanisms is ionization of plasma particles, the majority of which never become trapped. These untrapped particles experience plasma oscillations but do not steal a large amount of energy from the laser. The amount of energy lost to ionization is relatively unimportant as well. For example, full ionization of a cylindrical volume 100 μm *diameter* $\times$ 1 cm of helium at a density 5×10^{18} cm^{-3} requires only 5 mJ. In reality, more energy than just the ionization potential is transferred from the laser to plasma particles. In most examples from this research, the most important loss mechanism is mismatch from ideal accelerating conditions ($L_{deph} = L_{depl} = L_{accelerator}$ and direct laser losses from imperfect guiding. Beams produced from a ~ 3 J laser pulse in this research have had total

beam energy as high as 140 mJ in a broad spectrum up to 500 $MeV+$ and 106 mJ in a quasimonoenergetic beam with peak centered at 415 MeV. These examples indicate an efficiency for transferring laser energy to electron beam energy of $< 5\%$. Ref. [79] estimates that the efficiency for this step is independent of laser parameters for ideal operation in the bubble regime with a value of $\sim 20\%$. Ref. [81], however, indicates weak dependence of efficiency upon laser power, and predicts electron beam total energy of 230 mJ for matched parameters and laser power 100 TW and density 5×10^{18} cm^{-3}. The electron beam pulse duration can be estimated (conservatively) to be r_b/c. For operation in the bubble regime with $a_0 = 4.4$ and $n_e = 5 \times 10^{18}$ cm^{-3}, this corresponds to 33 fs. A beam with 1 nC charge and produced with a repetition rate of 0.1 Hz then corresponds to a peak beam current of 30 kA and an average current of 0.1 nA. The peak beam current estimate is conservative for the case of monoenergetic beams, in which case all the beam electrons bunch up at the center of the bubble. Petawatt lasers with 10 Hz repetition rate will be available in the near-term, improving the average beam current and betatron average brightness. Additionally, diode-pumped lasers with much higher wall efficiency are likely to be used in the next generation high power lasers.

8.3 Future Applications

8.3.1 Compact X-ray Probes

The bremsstrahlung or betatron radiation produced can be used for inelastic scattering of nuclear processes (e.g. active interrogation), metallurgy, crystal diffraction, protein crystallography, and high time-resolution pump-probe experiments. Images produced with the betatron source take advantage of spatial coherence, resulting in phase contrast enhanced imaging of sharp edges. Some recent LWFA results suggest

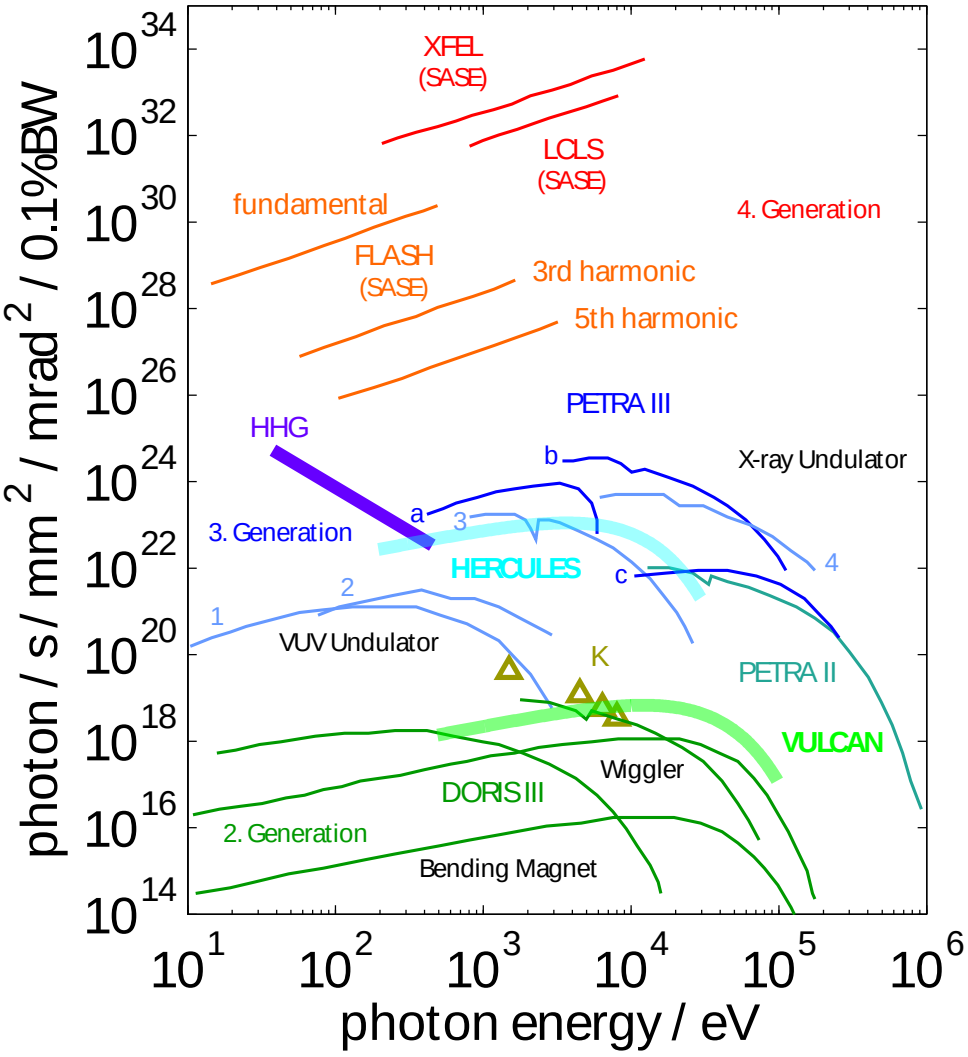

Figure 8.1: Comparison between the LWFA betatron source from a 10 mm gas jet and existing and future light sources. Image courtesy of Stefan Kneip.

	ALS [173]	This research Fig. 4.6, [117]	XFEL [5]	LCLS [1]
Electron E_{peak} $[GeV]$	1.9	0.5	17.5	15
Maximum Charge $[pC]$	1200	1000	1000	1000
Pulse length $[fs]$	70,000	$\leq$30	<100	≤ 10
X-ray Spectrum $[keV]$	sync ≤ 5	sync ≤ 10	line ≤ 12	line ≤ 8
Divergence $[\mu rad]$	<170	11,000	1	0.4
Source size $[\mu m]$	10(rms)	2(FWHM)	70(FWHM)	11(rms)
X-ray Peak Brightness $[ph/s/mm^2/mrad^2/0.1\%BW]$	10^{19}	10^{22}	10^{34}	10^{33}
X-ray Average Brightness $[ph/s/mm^2/mrad^2/0.1\%BW]$	10^{16}	10^{7}	10^{25}	10^{21}
Repetition rate $[Hz]$	10^8	0.1	10	120
Facility scale $[m]$	200	50	3000	3000
Beamlines	39	1	1	1

Table 8.2: Summary of parameters for current and prospective accelerator and synchrotron sources.

that the electron bunches could be as short as a few fs [174]. If this is true, the betatron pulse would be just as short, which is much shorter than the pulses produced at third generation accelerator facilities.

8.3.2 Electron Beam Applications

Synchrotron losses ($\propto 1/r^2$) have led circular particle accelerators to extremely large size. For this reason, the next generation high energy accelerator is likely to be linear (perhaps the ILC). In the case of the LWFA in the bubble regime, it is unlikely that the synchrotron radiation can be decoupled from the accelerator stage. This suggests that the bubble LWFA will be less beneficial as a TeV-scale accelerator but well suited for moderate-high energy acceleration for industrial and medical purposes or explicitly for radiation generation. LWFA in the linear regime, where transverse focusing fields are much weaker than in the bubble, may be useful for high energy acceleration with less concern about synchrotron losses.

Moderate energy LWFA electron beams could be used like a radioisotopic beta

source with an on/off switch. For example, the beam could be used for food irradiation [175], medical sterilization, disinfection, polymerization, or treatment of industrial waste [176]. Dose can be supplied either by the electrons themselves or by bremsstrahlung generation. Lasers capable of producing 100s of MeV electron beams with 10 Hz repetition rate are truly tabletop devices today. Many of these application demands could even be achieved using existing compact kHz repetition rate devices which produce ~ 1 MeV beams well-suited for treatment of industrial waste. These moderate energy applications, however, do not benefit from the unique features of LWFA beams- ultrashort pulse duration and compact acceleration length. Therefore, conventional accelerators are likely to continue to fill these roles.

8.3.3 Staging

Designs for LWFA intended for cutting edge high energy physics will most likely include multiple stages. At the very least, it is a good idea to include two stages- one optimized for injection and another optimized for very low density acceleration. This option was demonstrated in the SMLWFA regime using two gas jets in Ref. [177] and is currently under investigation in the bubble regime [178]. LWFA beams are ideal for injection into a second wakefield because of their subpicosecond synchronization and ultrashort pulse duration. The difficult task of injecting a laser for each stage while retaining the advantages of short stages is under investigation in Ref. [179] in which a thin water jet is used as a plasma mirror.

APPENDIX

APPENDIX A

Plasma Frequency

This derivation relies on linearization and it includes ion motion in three dimensions. The following fluid equations express charge conservation and momentum conservation for electrons in an unmagnetized plasma:

$$\frac{\partial n_e}{\partial t} + \nabla \cdot (n_e \mathbf{u_e}) = 0 \tag{A.1a}$$

$$n_e m_e \left(\frac{\partial \mathbf{u_e}}{\partial t} + \mathbf{u_e} \cdot \nabla \mathbf{u_e} \right) = -n_e e \mathcal{E} \tag{A.1b}$$

and two more equivalent equations exist for the ions. If we linearize these four equations (assume quantities are composed of a steady-state value and a time-varying perturbation quantity such that $n_e = n_{e0} + n_{e1}, \mathbf{u_e} = \mathbf{u_{e0}} + \mathbf{u_{e1}}, \mathcal{E} = \mathcal{E}_\mathbf{0} + \mathcal{E}_\mathbf{1}$, etc. and assume the perturbation quantities are very small compared to the steady-state quantities), and that the steady-state fluid velocity and electric field are 0, the behavior will be predominantly described by terms with a single perturbation quantity. Keeping only these terms leaves:

$$\frac{\partial n_{e1}}{\partial t} + n_{e0} \nabla \cdot \mathbf{u_{e1}} = 0 \tag{A.2a}$$

$$m_e \frac{\partial \mathbf{u_{e1}}}{\partial t} = -e \mathcal{E}_\mathbf{1} \tag{A.2b}$$

and two equivalent equations for the ions. Differentiating A.2a with respect to time and inserting A.2b gives:

$$\frac{\partial^2 n_{e1}}{\partial^2 t} - \frac{e n_{e0}}{m_e} \nabla \cdot \boldsymbol{\mathcal{E}_1} = 0. \tag{A.3}$$

Poisson's equation can be written:

$$\nabla \cdot \boldsymbol{\mathcal{E}_1} = 4\pi e(n_{i1} - n_{e1}). \tag{A.4}$$

Combining the electron and ion equations and assuming a singly-ionized plasma with $n_{e0} = n_{i0} = n_0$,

$$\frac{\partial^2 e\rho}{\partial^2 t} + \omega_p^2 e\rho = 0 \tag{A.5}$$

where ω_p^2 is $\omega_e^2 + \omega_{pi}^2$ and $\omega_{pi} = \sqrt{\frac{m_e}{m_i}}\omega_e$. This equation describes harmonic motion at the plasma frequency. For any plasmas relevant to this thesis, $\sqrt{\frac{m_e}{m_i}} \ll 1$ and the plasma frequency is often defined to be the electron plasma frequency,

$$\omega_p \equiv \omega_e = \sqrt{\frac{4\pi e^2 n_e}{m_e}}. \tag{A.6}$$

Constants			
	mks units	cgs units	other
c	$2.998 \times 10^{8}\ m/s$	$2.998 \times 10^{10}\ cm/s$	$299.8 \mu m/ps$
e	$1.602 \times 10^{-19}\ C$	$4.803 \times 10^{-10}\ esu$	
m_e	$9.109 \times 10^{-31}\ kg$	$9.109 \times 10^{-28}\ g$	$0.5110\ MeV$
m_e/m_p	1837	1837	
k	$1.381 \times 10^{-23}\ J/K$	$1.381 \times 10^{-16}\ erg/K$	$8.617 \times 10^{-5}\ eV/K$
h	$6.626 \times 10^{-34}\ Js$	$6.626 \times 10^{-27}\ ergs$	$4.136 \times 10^{-15}\ eVs$

Formulas				
ω_p		$= \left(\frac{4\pi e^2 n}{m_e}\right)^{1/2}$		$[rad/s] = 5.641 \times 10^4 \sqrt{n_e[cm^{-3}]}$
ω_0		$= \frac{2\pi c}{\lambda_0}$		$[rad/s] = 2.355 \times 10^{15} \frac{800}{\lambda[nm]}$
λ_p		$= \frac{2\pi c}{\omega_p}$		$[\mu m] = 3.34 \times 10^{10} / \sqrt{n_e[cm^{-3}]}$
n_c		$= \frac{m_e \omega_0^2}{4\pi e^2}$		$[cm^{-3}] = 1.74 \times 10^{21} \frac{800^2}{\lambda_0^2[nm]}$
$c\tau$				$[\mu m] = 8.994 \frac{\tau[fs]}{30}$
τ_{HW/e^2}				$= \frac{\tau_{FWHM}}{\sqrt{2 \ln 2}}$
a_0		$= \frac{e\mathcal{E}}{m_e \omega_0 c}$		$= 6.88 \times 10^{-10} \frac{\lambda[nm]}{800} \sqrt{I[W/cm^2]}$
$v_g \simeq v_{pw}$		$= c\sqrt{1 - n_e/n_c}$		
γ_p		$= 1/\sqrt{(1 - v_{pw}^2/c^2)}$		$[bubble] \simeq \frac{\omega_0}{\sqrt{3}\omega_p}$
L_{depl}		$\simeq c\tau_{FWHM} \frac{n_c}{n_e}$		
L_{deph}		$\simeq \frac{c}{c - v_g} \frac{\lambda_p}{2}$		
r_{Larmor}		$= \frac{m_e c^2}{eB} \sqrt{\gamma^2 - 1}$		$[cm] = 1.7 \times 10^3 \frac{\sqrt{\gamma^2 - 1}}{B[gauss]}$
$B - integral$		$= \frac{2\pi}{\lambda_0} \int_0^T \eta_2 I(z) dz$		

BIBLIOGRAPHY

BIBLIOGRAPHY

[1] LCLS website: http://lcls.slac.stanford.edu/, 2011. 3, 123

[2] Soleil website: http://www.synchrotron-soleil.fr/, 2011. 3, 28

[3] Swiss Light Source website: http://sls.web.psi.ch/, 2011. 3

[4] FLASH website: http://flash.desy.de/, 2011. 3

[5] XFEL website: http://www.xfel.eu/, 2011. 4, 123

[6] International Linear Collider website: http://www.linearcollider.org/, 2011. 4

[7] C. Vieu, F. Carcenac, A. Pépin, Y. Chen, M. Mejias, A. Lebib, L. Manin-Ferlazzo, L. Couraud, and H. Launois. Electron beam lithography: resolution limits and applications. *Applied Surface Science*, 164(1-4):111 – 117, 2000. 5

[8] C. Chiu, M. Fomytskyi, F. Grigsby, F. Raischel, M. Downer, and T. Tajima. Laser electron accelerators for radiation medicine: a feasibility study. Technical report, University of Texas at Austin, 2003. 5

[9] William Bertozzi and Robert J. Ledoux. Nuclear resonance fluorescence imaging in non-intrusive cargo inspection. *Nuclear Instruments and Methods in Physics Research Section B: Beam Interactions with Materials and Atoms*, 241(1-4):820 – 825, 2005. The Application of Accelerators in Research and Industry - Proceedings of the Eighteenth International Conference on the Application of Accelerators in Research and Industry (CAARI 2004). 5

[10] T. E. Cowan, A. W. Hunt, T. W. Phillips, S. C. Wilks, M. D. Perry, C. Brown, W. Fountain, S. Hatchett, J. Johnson, M. H. Key, T. Parnell, D. M. Pennington, R. A. Snavely, and Y. Takahashi. Photonuclear fission from high energy electrons from ultraintense laser-solid interactions. *Phys. Rev. Lett.*, 84(5):903–906, Jan 2000. 5

[11] J. Magill, H. Schwoerer, F. Ewald, J. Galy, R. Schenkel, and R. Sauerbrey. Laser transmutation of iodine-129. *Applied Physics B: Lasers and Optics*, 77:387–390, 2003. 10.1007/s00340-003-1306-4.

[12] S. A. Reed, V. Chvykov, G. Kalintchenko, T. Matsuoka, P. Rousseau, V. Yanovsky, C. R. Vane, J. R. Beene, D. Stracener, D. R. Schultz, and A. Maksimchuk. Photonuclear fission with quasimonoenergetic electron beams from laser wakefields. *Applied Physics Letters*, 89(23):231107, 2006. 5

[13] D. A. G. Deacon, L. R. Elias, J. M. J. Madey, G. J. Ramian, H. A. Schwettman, and T. I. Smith. First operation of a free-electron laser. *Phys. Rev. Lett.*, 38(16):892–894, Apr 1977. 5

[14] M. Seto, Y. Yoda, S. Kikuta, X. W. Zhang, and M. Ando. Observation of nuclear resonant scattering accompanied by phonon excitation using synchrotron radiation. *Phys. Rev. Lett.*, 74(19):3828–3831, May 1995. 5

[15] V. G. Kohn, A. I. Chumakov, and R. Rueffer. Nuclear resonant inelastic absorption of synchrotron radiation in an anisotropic single crystal. *Phys. Rev. B*, 58(13):8437–8444, Oct 1998. 5

[16] R. Abela and B.D. Patterson. Time-resolved scattering from chemical systems at the proposed swissfel x-ray laser project. *TrAC Trends in Analytical Chemistry*, 29(6):538 – 543, 2010. Analytical applications of synchrotron radiation. 5

[17] Walter Walter Reimers, Anke Rita Pyzalla, Andreas K. Schreyer, and Helmut Clemens. *Neutrons and Synchrotron Radiation in Engineering Materials Science*. Wiley-VCH, Berlin, 1 edition, 2008. 5

[18] Roger Fourme, Eric Girard, Richard Kahn, Anne-Claire Dhaussy, and Isabella Ascone. Advances in high-pressure biophysics: Status and prospects of macromolecular crystallography. *Annual Review of Biophysics*, 38(1):153–171, 2009. PMID: 19416064. 5

[19] Stephen K. Burley and Jeffrey B. Bonanno. Structuring the universe of proteins. *Annual Review of Genomics and Human Genetics*, 3(1):243–262, 2002. 5

[20] Andy Ka-Leung Ng, Hongmin Zhang, Kemin Tan, Zongli Li, Jin-huan Liu, Paul Kay-Sheung Chan, Sui-Mui Li, Wood-Yee Chan, Shannon Wing-Ngor Au, Andrzej Joachimiak, Thomas Walz, Jia-Huai Wang, and Pang-Chui Shaw. Structure of the influenza virus A H5N1 nucleoprotein: implications for RNA binding, oligomerization, and vaccine design. *The FASEB Journal*, 22(10):3638–3647, 2008. 5

[21] Rui Xu, Ryan McBride, James C. Paulson, Christopher F. Basler, and Ian A. Wilson. Structure, receptor binding, and antigenicity of influenza virus hemagglutinins from the 1957 H2N2 pandemic. *J. Virol.*, 84(4):1715–1721, 2010. 5

[22] I. Wilson. The compact linear collider CLIC. *Physics Reports*, 403-404:365 – 378, 2004. CERN - the second 25 years. 6

[23] C. Gahn, G. D. Tsakiris, A. Pukhov, J. Meyer-ter Vehn, G. Pretzler, P. Thirolf, D. Habs, and K. J. Witte. Multi-MeV electron beam generation by direct laser acceleration in high-density plasma channels. *Phys. Rev. Lett.*, 83(23):4772–4775, Dec 1999. 6

[24] John M. Dawson. Nonlinear electron oscillations in a cold plasma. *Phys. Rev.*, 113(2):383–387, Jan 1959. 6

[25] T. Tajima and J. Dawson. Laser electron accelerator. *Phys. Rev. Lett.*, 43:267, 1979. 7

[26] C. E. Clayton, C. Joshi, C. Darrow, et al. Relativistic plasma-wave excitation by collinear optical mixing. *Phys. Rev. Lett.*, 54:2343–2346, 1985. 7

[27] A. E. Dangor, A. K. L. Dymokebradshaw, and A. E. Dyson. Observation of relativistic plasma-waves generated by the beat- wave with 1 mu-m lasers. *Physica Scripta*, T30:107–109, 1990. 7

[28] C. E. Clayton, M. J. Everett, A. Lal, D. Gordon, K. A. Marsh, and C. Joshi. Acceleration and scattering of injected electrons in plasma beat-wave accelerator experiments. *Physics of Plasmas*, 1(5):1753–1760, 1994. 7

[29] K. Nakajima, D. Fisher, T. Kawakubo, H. Nakanishi, A. Ogata, Y. Kato, Y. Kitagawa, R. Kodama, K. Mima, H. Shiraga, K. Suzuki, K. Yamakawa, T. Zhang, Y. Sakawa, T. Shoji, Y. Nishida, N. Yugami, M. Downer, and T. Tajima. Observation of ultrahigh gradient electron acceleration by a self-modulated intense short laser-pulse. *Phys. Rev. Lett.*, 74(22):4428–4431, 1995. 7

[30] A. Ting, C. I. Moore, K. Krushelnick, C. Manka, E. Esarey, P. Sprangle, R. Hubbard, H. R. Burris, R. Fischer, and M. Baine. Plasma wakefield generation and electron acceleration in a self-modulated laser wakefield accelerator experiment. *Physics of Plasmas*, 4(5):1889–1899, 1997.

[31] D. Umstadter, S.-Y. Chen, A. Maksimchuk, G. Mourou, and R. Wagner. Nonlinear optics in relativistic plasmas and laser wake field acceleration of electrons. *Science*, 273(5274):472–475, 1996.

[32] E. Miura, K. Koyama, S. Kato, et al. Demonstration of quasi-monoenergetic electron-beam generation in laser-driven plasma acceleration. *Appl. Phys. Lett.*, 86:251501, 2005.

[33] B. Hidding, K. U. Amthor, B. Liesfeld, et al. Generation of quasimonoenergetic electron bunches with 80-fs laser pulses. *Phys. Rev. Lett.*, 96:105004, 2006.

[34] B. Hidding, M. Geissler, G. Pretzler, K.-U. Amthor, H. Schwoerer, S. Karsch, L. Veisz, K. Schmid, and R. Sauerbrey. Quasimonoenergetic electron acceleration in the self-modulated laser wakefield regime. *Physics of Plasmas*, 16(4):043105, 2009. 7

[35] S. V. Bulanov, F. Pegoraro, A. M. Pukhov, and A. S. Sakharov. Transverse-wake wave breaking. *Phys. Rev. Lett.*, 78(22):4205–4208, Jun 1997. 7

[36] A. Modena, Z. Najmudin, A. E. Dangor, C. E. Clayton, K. A. Marsh, C. Joshi, V. Malka, C. B. Darrow, C. Danson, D. Neely, and F. N. Walsh. Electron acceleration from the breaking of relativistic plasma-waves. *Nature*, 377(6550):606–608, 1995. 7, 24

[37] Z. Najmudin, K. Krushelnick, E. L. Clark, S. P. D. Mangles, B. Walton, A. E. Dangor, V. Malka, S. Fritzler, E. Lefebvre, F. Tsung, and C. Joshi. Self-modulated wakefield and forced laser wakefield acceleration of electrons. *Physics of Plasmas*, 10(5):2071–2077, 2003. 7

[38] S. P. D. Mangles, C. D. Murphy, Z. Najmudin, A. G. R. Thomas, J. L. Collier, A. E. Dangor, E. J. Divall, P. S. Foster, J. G. Gallacher, C. J. Hooker, D. A. Jaroszynski, A. J. Langley, W. B. Mori, P. A. Norreys, F. S. Tsung, R. Viskup, B. R. Walton, and K. Krushelnick. Monoenergetic beams of relativistic electrons from intense laserplasma interactions. *Nature*, 431(7008):535–538, September 2004. 7

[39] C. G. R. Geddes, Cs Toth, J. van Tilborg, E. Esarey, C. B. Schroeder, D. Bruhwiler, C. Nieter, J. Cary, and W. P. Leemans. High-quality electron beams from a laser wakefield accelerator using plasma-channel guiding. *Nature*, 431(7008):538–541, September 2004.

[40] J. Faure, Y. Glinec, A. Pukhov, S. Kiselev, S. Gordienko, E. Lefebvre, J.-P. Rousseau, F. Burgy, and V. Malka. A laser-plasma accelerator producing monoenergetic electron beams. *Nature*, 431(7008):541–544, September 2004. 7

[41] W. P. Leemans, B. Nagler, A. J. Gonsalves, et al. GeV electron beams from a centimetre-scale accelerator. *Nature Phys.*, 2:696–699, 2006. 7, 27, 69

[42] K. Krushelnick, Z. Najmudin, and A. E. Dangor. Particle acceleration using intense laser produced plasmas. *Laser Phys. Lett.*, 4:847–862, 2007. 8

[43] V. Malka, J. Faure, Y. Gauduel, E. Lefebvre, A. Rousse, and K. Ta Phuoc. Principles and applications of compact laserplasma accelerators. *Nature Physics*, 4:447–453, 2008.

[44] E. Esarey, C. B. Schroeder, and W. P. Leemans. Physics of laser-driven plasma-based electron accelerators. *Rev. Mod. Phys.*, 81(3):1229–1285, Aug 2009. 8, 18

[45] C. B. Schroeder, E. Esarey, C. G. R. Geddes, Cs. Tóth, and W. P. Leemans. Design considerations for a laser-plasma linear collider. *AIP Conference Proceedings*, 1086(1):208–214, 2009. 8

[46] S. Bulanov and V. Khoroshkov. Feasibility of using laser ion accelerators in proton therapy. *Plasma Physics Reports*, 28:453–456, 2002. 10.1134/1.1478534. 8

[47] M. V. Ammosov, N. B. Delone, and V. P. Krainov. Tunnel ionization of complex atoms and atomic ions in a varying electromagnetic-field. *Zhurnal Eksperimentalnoi I Teoreticheskoi Fiziki*, 91(6):2008–2013, DEC 1986. 11, 12, 110

[48] P. B. Corkum, N. H. Burnett, and F. Brunel. Above-threshold ionization in the long-wavelength limit. *Phys. Rev. Lett.*, 62(11):1259–1262, Mar 1989. 12, 101

[49] P. B. Corkum. Plasma perspective on strong field multiphoton ionization. *Phys. Rev. Lett.*, 71(13):1994–1997, Sep 1993. 12

[50] L. V. Keldysh. Ionisation in the field of a strong electromagnetic wave. *Soviet Physics JETP-USSR*, 20:1307, 1965. 12

[51] A. M. Perelomov, V. S. Popov, and M. V. Terent'ev. Ionisation of atoms in an alternating electric field. *Sov. Phys. JETP*, 23:924, 1966. 12

[52] X. M. Tong, Z. X. Zhao, and C. D. Lin. Theory of molecular tunneling ionization. *Phys. Rev. A*, 66(3):033402, Sep 2002. 12

[53] M. V. Ammosov, P. A. Golovinsky, I. Yu. Kiyan, V. P. Krainov, and V. M. Ristic. Tunneling ionization of atoms and atomic ions in an intense laser field with a nonhomogeneous space–time distribution. *J. Opt. Soc. Am. B*, 9(8):1225–1230, Aug 1992. 13

[54] S. Augst, D. Strickland, D. D. Meyerhofer, S. L. Chin, and J. H. Eberly. Tunneling ionization of noble gases in a high-intensity laser field. *Phys. Rev. Lett.*, 63(20):2212–2215, Nov 1989. 13, 14, 112

[55] William M. Wood, Glenn Focht, and M. C. Downer. Tight focusing and blue shifting of millijoule femtosecond pulses from a conical axicon amplifier. *Opt. Lett.*, 13(11):984–986, Nov 1988. 15, 79

[56] Wm. M. Wood, C. W. Siders, and M. C. Downer. Measurement of femtosecond ionization dynamics of atmospheric density gases by spectral blueshifting. *Phys. Rev. Lett.*, 67(25):3523–3526, Dec 1991.

[57] E. Esarey, G. Joyce, and P. Sprangle. Frequency up-shifting of laser pulses by copropagating ionization fronts. *Phys. Rev. A*, 44(6):3908–3911, Sep 1991. 15

[58] Bahaa E. A. Saleh and Malvin Carl Teich. *Fundamentals of photonics*. John Wiley and Sons Inc., New York, 1 edition, 1991. 16

[59] S. C. Wilks, J. M. Dawson, W. B. Mori, T. Katsouleas, and M. E. Jones. Photon accelerator. *Phys. Rev. Lett.*, 62(22):2600–2603, May 1989. 16, 82

[60] S.C. Rae. Ionization-induced defocusing of intense laser pulses in high-pressure gases. *Optics Communications*, 97(1-2):25 – 28, 1993. 17

[61] E. Esarey, P. Sprangle, J. Krall, and A. Ting. Self-focusing and guiding of short laser pulses in ionizing gases and plasmas. *Quantum Electronics, IEEE Journal of*, 33(11):1879 –1914, Nov 1997. 17, 73

[62] J. Faure, V. Malka, J.R. Marquès, P.G. David, F. Amiranoff, K. Ta Phuoc, and A. Rousse. Effects of pulse duration on self-focusing of ultra-short lasers in underdense plasmas. *Physics of Plasmas*, 9(3):756–759, 2002. 17

[63] A. G. R. Thomas, Z. Najmudin, S. P. D. Mangles, C. D. Murphy, A. E. Dangor, C Kamperidis, K. L. Lancaster, W. B. Mori, P. A. Norreys, W. Rozmus, and K. Krushelnick. The effect of laser focusing conditions on propagation and monoenergetic electron production in laser wakefield accelerators. *Phys. Rev. Lett.*, 98(1):095004, 2007. 17

[64] S. Kneip, S. R. Nagel, S. F. Martins, S. P. D. Mangles, C. Bellei, O. Chekhlov, R. J. Clarke, N. Delerue, E. J. Divall, G. Doucas, K. Ertel, F. Fiuza, R. Fonseca, P. Foster, S. J. Hawkes, C. J. Hooker, K. Krushelnick, W. B. Mori, C. A. J. Palmer, K. Ta Phuoc, P. P. Rajeev, J. Schreiber, M. J. V. Streeter, D. Urner, J. Vieira, L. O. Silva, and Z. Najmudin. Near-GeV acceleration of electrons by a nonlinear plasma wave driven by a self-guided laser pulse. *Phys. Rev. Lett.*, 103(3):035002, Jul 2009.

[65] J. E. Ralph, K. A. Marsh, A. E. Pak, W. Lu, C. E. Clayton, F. Fang, W. B. Mori, and C. Joshi. Self-guiding of ultrashort, relativistically intense laser pulses through underdense plasmas in the blowout regime. *Phys. Rev. Lett.*, 102(17):175003, Apr 2009.

[66] J. E. Ralph, C. E. Clayton, F. Albert, B. B. Pollock, S. F. Martins, A. E. Pak, K. A. Marsh, J. L. Shaw, A. Till, J. P. Palastro, W. Lu, S. H. Glenzer, L. O. Silva, W. B. Mori, C. Joshi, and D. H. Froula. Laser wakefield acceleration at reduced density in the self-guided regime. *Physics of Plasmas*, 17(5):056709, 2010. 17, 86, 113

[67] F. Cattani, A. Kim, D. Anderson, and M. Lisak. Multifilament structures in relativistic self-focusing. *Phys. Rev. E*, 6401(1):016412, 2001. 17

[68] C. W. Siders, S. P. Le Blanc, D. Fisher, T. Tajima, M. C. Downer, A. Babine, A. Stepanov, and A. Sergeev. Laser wakefield excitation and measurement by femtosecond longitudinal interferometry. *Phys. Rev. Lett.*, 76(19):3570–3573, May 1996. 21

[69] N. H. Matlis, S. Reed, S. S. Bulanov, et al. Snapshots of laser wakefields. *Nature Phys.*, 2:749–753, 2006. 21

[70] G. Z. Sun, E. Ott, Y. C. Lee, and P. Guzdar. Self-focusing of short intense pulses in plasmas. *Physics of Fluids*, 30(2):526–532, 1987. 21

[71] A. Pukhov and J. Meyer-ter Vehn. Laser wake field acceleration: the highly non-linear broken- wave regime. *Appl. Phys. B*, 74:355–361, 2002. 21

[72] I. Kostyukov, A. Pukhov, and S. Kiselev. Phenomenological theory of laser-plasma interaction in "bubble" regime. *Physics of Plasmas*, 11(11):5256–5264, 2004. 21

[73] A. Pukhov, S. Gordienko, S. Kiselev, and I. Kostyukov. The bubble regime of laser-plasma acceleration: monoenergetic electrons and the scalability. *Plasma Physics and Controlled Fusion*, 46:B179–B186, 2004. 21

[74] M. Geissler, J. Schreiber, and J. Meyer-Ter-Vehn. Bubble acceleration of electrons with few-cycle laser pulses. *New J. Phys.*, 8:186, 2006. 21

[75] K. Schmid, L. Veisz, F. Tavella, S. Benavides, R. Tautz, D. Herrmann, A. Buck, B. Hidding, A. Marcinkevicius, U. Schramm, M. Geissler, J. Meyer-ter Vehn, D. Habs, and F. Krausz. Few-cycle laser-driven electron acceleration. *Phys. Rev. Lett.*, 102(12):124801, Mar 2009. 21

[76] P. Dong, S. A. Reed, S. A. Yi, S. Kalmykov, G. Shvets, M. C. Downer, N. H. Matlis, W. P. Leemans, C. McGuffey, S. S. Bulanov, V. Chvykov, G. Kalintchenko, K. Krushelnick, A. Maksimchuk, T. Matsuoka, A. G. R. Thomas, and V. Yanovsky. Formation of optical bullets in laser-driven plasma bubble accelerators. *Physical Review Letters*, 104(13):134801–+, April 2010. 21

[77] P Dong, S A Reed, S A Yi, S Kalmykov, Z Y Li, G Shvets, N H Matlis, C McGuffey, S S Bulanov, V Chvykov, G Kalintchenko, K Krushelnick, A Maksimchuk, T Matsuoka, A G R Thomas, V Yanovsky, and M C Downer. Holographic visualization of laser wakefields. *New Journal of Physics*, 12(4):045016, 2010. 21

[78] W. Lu, C. Huang, M. Zhou, M. Tzoufras, F. S. Tsung, W. B. Mori, and T. Katsouleas. A nonlinear theory for multidimensional relativistic plasma wave wakefields. *Physics of Plasmas*, 13(5):056709–056709–13, 2006. 22

[79] S. Gordienko and A. Pukhov. Scalings for ultrarelativistic laser plasmas and quasimonoenergetic electrons. *Phys. Plasmas*, 12:043109, 2005. 22, 121

[80] W. Lu, C. Huang, M. Zhou, W. B. Mori, and T. Katsouleas. Nonlinear theory for relativistic plasma wakefields in the blowout regime. *Phys. Rev. Lett.*, 96(16):165002, 2006.

[81] W. Lu, M. Tzoufras, C. Joshi, F. S. Tsung, W. B. Mori, J. Vieira, R. A. Fonseca, and L. O. Silva. Generating multi-GeV electron bunches using single stage laser wakefield acceleration in a 3d nonlinear regime. *Phys. Rev. ST Accel. Beams*, 10(6):061301, Jun 2007. 22, 24, 50, 100, 119, 121

[82] J. F. Drake, P. K. Kaw, Y. C. Lee, G. Schmid, C. S. Liu, and Marshall N. Rosenbluth. Parametric instabilities of electromagnetic waves in plasmas. *Physics of Fluids*, 17(4):778–785, 1974. 23

[83] William L. Kruer. *The Physics of Laser Plasma Interactions*. Westview Press, Boulder, CO, 2003. 23

[84] S. Bulanov, N. Naumova, F. Pegoraro, and J. Sakai. Particle injection into the wave acceleration phase due to nonlinear wake wave breaking. *Phys. Rev. E*, 58(5):R5257–R5260, Nov 1998. 24

[85] S. Kalmykov, S. A. Yi, V. Khudik, and G. Shvets. Electron self-injection and trapping into an evolving plasma bubble. *Phys. Rev. Lett.*, 103(13):135004, Sep 2009. 24, 25

[86] I. Kostyukov, E. Nerush, A. Pukhov, and V. Seredov. Electron self-injection in multidimensional relativistic-plasma wake fields. *Phys. Rev. Lett.*, 103(17):175003, Oct 2009. 24, 25

[87] D. H. Froula, C. E. Clayton, T. Döppner, K. A. Marsh, C. P. J. Barty, L. Divol, R. A. Fonseca, S. H. Glenzer, C. Joshi, W. Lu, S. F. Martins, P. Michel, W. B. Mori, J. P. Palastro, B. B. Pollock, A. Pak, J. E. Ralph, J. S. Ross, C. W. Siders, L. O. Silva, and T. Wang. Measurements of the critical power for self-injection of electrons in a laser wakefield accelerator. *Phys. Rev. Lett.*, 103(21):215006, Nov 2009. 24

[88] A. G. R. Thomas. Scalings for radiation from plasma bubbles. *Physics of Plasmas*, 17(5):056708, 2010. 25

[89] C. B. Schroeder, P. B. Lee, J. S. Wurtele, E. Esarey, and W. P. Leemans. Generation of ultrashort electron bunches by colliding laser pulses. *Phys. Rev. E*, 59(5):6037–6047, May 1999. 25

[90] E. Esarey, R. F. Hubbard, W. P. Leemans, A. Ting, and P. Sprangle. Electron injection into plasma wakefields by colliding laser pulses. *Phys. Rev. Lett.*, 79(14):2682–2685, Oct 1997.

[91] H. Kotaki, S. Masuda, M. Kando, J. K. Koga, and K. Nakajima. Head-on injection of a high quality electron beam by the interaction of two laser pulses. *Physics of Plasmas*, 11(6):3296–3302, 2004.

[92] J. Faure, C. Rechatin, A. Norlin, et al. Controlled injection and acceleration of electrons in plasma wakefields by colliding laser pulses. *Nature*, 444:737–739, 2006.

[93] C. Rechatin, J. Faure, A. Ben-Ismail, J. Lim, R. Fitour, A. Specka, H. Videau, A. Tafzi, F. Burgy, and V. Malka. Controlling the phase-space volume of injected electrons in a laser-plasma accelerator. *Phys. Rev. Lett.*, 102(16):164801, Apr 2009. 25

[94] J. Faure, C. Rechatin, O. Lundh, L. Ammoura, and V. Malka. Injection and acceleration of quasimonoenergetic relativistic electron beams using density gradients at the edges of a plasma channel. *Physics of Plasmas*, 17(8):083107, 2010. 25

[95] M. Tzoufras, W. Lu, F. S. Tsung, C. Huang, W. B. Mori, T. Katsouleas, J. Vieira, R. A. Fonseca, and L. O. Silva. Beam loading in the nonlinear regime of plasma-based acceleration. *Phys. Rev. Lett.*, 101(14):145002, Sep 2008. 25

[96] C. Rechatin, X. Davoine, A. Lifschitz, A. Ben Ismail, J. Lim, E. Lefebvre, J. Faure, and V. Malka. Observation of Beam Loading in a Laser-Plasma Accelerator. *Physical Review Letters*, 103(19):194804+, November 2009. 25

[97] C. D. Decker, W. B. Mori, K. C. Tzeng, and T. Katsouleas. Evolution of ultra-intense, short-pulse lasers in underdense plasmas. *Physics of Plasmas*, 3(5):2047–2056, 1996. 26

[98] C. E. Clayton, J. E. Ralph, F. Albert, R. A. Fonseca, S. H. Glenzer, C. Joshi, W. Lu, K. A. Marsh, S. F. Martins, W. B. Mori, A. Pak, F. S. Tsung, B. B. Pollock, J. S. Ross, L. O. Silva, and D. H. Froula. Self-Guided Laser Wakefield Acceleration beyond 1 GeV Using Ionization-Induced Injection. *Physical Review Letters*, 105(10):105003+, Sep 2010. 27, 113

[99] C. T. Hsieh, C. M. Huang, C. L. Chang, et al. Tomography of injection and acceleration of monoenergetic electrons in a laser-wakefield accelerator. *Phys. Rev. Lett.*, 96:095001, 2006. 27

[100] Soleil website: http://www.synchrotron-soleil.fr/portal/page/portal/Source-Accelerateur/HU80, 2011. 28

[101] David Attwood. *Soft X-rays and Extreme Ultraviolet Radiation*. Cambridge University Press, Cambridge, UK, 1 edition, 1999. 29

[102] H.-P. Schlenvoigt, K. Haupt, A. Debus, et al. A compact synchrotron radiation source driven by a laser-plasma wakefield. *Nature Phys.*, 4:130–133, 2007. 30

[103] Matthias Fuchs, Raphael Weingartner, Antonia Popp, Zsuzsanna Major, Stefan Becker, Jens Osterhoff, Isabella Cortrie, Benno Zeitler, Rainer Horlein, George D. Tsakiris, Ulrich Schramm, Tom P. Rowlands-Rees, Simon M. Hooker, Dietrich Habs, Ferenc Krausz, Stefan Karsch, and Florian Gruner. Laser-driven soft-X-ray undulator source. *Nature Physics*, 5(11):826–829, September 2009. 30

[104] E. Esarey, B. A. Shadwick, P. Catravas, and W. P. Leemans. Synchrotron radiation from electron beams in plasma-focusing channels. *Phys. Rev. E*, 65(5):056505, May 2002. 30

[105] I. Kostyukov, S. Kiselev, and A. Pukhov. X-ray generation in an ion channel. *Physics of Plasmas*, 10(12):4818–4828, 2003.

[106] A. Rousse, K. Ta Phuoc, R. Shah, R. Fitour, and F. Albert. Scaling of betatron x-ray radiation. *The European Physical Journal D - Atomic, Molecular, Optical and Plasma Physics*, 45:391–398, 2007. 10.1140/epjd/e2007-00249-7.

[107] K. Ta Phuoc, E. Esarey, V. Leurent, E. Cormier-Michel, C. G. R. Geddes, C. B. Schroeder, A. Rousse, and W. P. Leemans. Betatron radiation from density tailored plasmas. *Physics of Plasmas*, 15(6):063102, 2008.

[108] Kim Ta Phuoc, Sebastien Corde, Romuald Fitour, Rahul Shah, Felicie Albert, Jean-Philippe Rousseau, Fréderic Burgy, Antoine Rousse, Vasily Seredov, and Alexander Pukhov. Analysis of wakefield electron orbits in plasma wiggler. *Physics of Plasmas*, 15(7):073106, 2008.

[109] Félicie Albert, Rahul Shah, Kim Ta Phuoc, Romuald Fitour, Fréderic Burgy, Jean-Philippe Rousseau, Amar Tafzi, Denis Douillet, Thierry Lefrou, and Antoine Rousse. Betatron oscillations of electrons accelerated in laser wakefields characterized by spectral x-ray analysis. *Phys. Rev. E*, 77(5):056402, May 2008.

[110] A. G. R. Thomas and K. Krushelnick. Betatron x-ray generation from electrons accelerated in a plasma cavity in the presence of laser fields. *Physics of Plasmas*, 16(10):103103, 2009. 30

[111] Kim Ta Phuoc, Sebastien Corde, Rahul Shah, Felicie Albert, Romuald Fitour, Jean-Philippe Rousseau, Fréderic Burgy, Brigitte Mercier, and Antoine Rousse. Imaging electron trajectories in a laser-wakefield cavity using betatron x-ray radiation. *Phys. Rev. Lett.*, 97(22):225002, Nov 2006. 30

[112] Y. Glinec, J. Faure, A. Lifschitz, J. M. Vieira, R A. Fonseca, L. O. Silva, and V. Malka. Direct observation of betatron oscillations in a laser-plasma electron accelerator. *EPL (Europhysics Letters)*, 81(6):64001, 2008.

[113] T. Matsuoka, S. Kneip, C. McGuffey, C. Palmer, J. Schreiber, C. Huntington, Y. Horovitz, F. Dollar, V. Chvykov, G. Kalintchenko, A. G. R. Thomas, V. Yanovsky, K. T. Phuoc, S. P. D. Mangles, Z. Najmudin, A. Maksimchuk, and K. Krushelnick. Synchrotron x-ray radiation from laser wakefield accelerated electron beams in a plasma channel. *Journal of Physics Conference Series*, 244(4):042026, August 2010. 30

[114] A. Rousse, K. T. Phuoc, R. Shah, et al. Production of a keV x-ray beam from synchrotron radiation in relativistic laser-plasma interaction. *Phys. Rev. Lett.*, 93:135005, 2004. 30

[115] Kim Ta Phuoc, Fréderic Burgy, Jean-Philippe Rousseau, Victor Malka, Antoine Rousse, Rahul Shah, Donald Umstadter, Alexander Pukhov, and Sergei Kiselev. Laser based synchrotron radiation. *Physics of Plasmas*, 12(2):023101, 2005.

[116] S. Kneip, S. R. Nagel, C. Bellei, N. Bourgeois, A. E. Dangor, A. Gopal, R. Heathcote, S. P. D. Mangles, J. R. Marquès, A. Maksimchuk, P. M. Nilson,

K. Ta Phuoc, S. Reed, M. Tzoufras, F. S. Tsung, L. Willingale, W. B. Mori, A. Rousse, K. Krushelnick, and Z. Najmudin. Observation of synchrotron radiation from electrons accelerated in a petawatt-laser-generated plasma cavity. *Phys. Rev. Lett.*, 100(10):105006, Mar 2008.

[117] S. Kneip, C. McGuffey, J. L. Martins, S. F. Martins, C. Bellei, V. Chvykov, F. Dollar, R. Fonseca, C. Huntington, G. Kalintchenko, A. Maksimchuk, S. P. D. Mangles, T. Matsuoka, S. R. Nagel, C. A. J. Palmer, J. Schreiber, K. Ta Phuoc, A. G. R. Thomas, V. Yanovsky, L. O. Silva, K. Krushelnick, and Z. Najmudin. Bright spatially coherent synchrotron x-rays from a table-top source. *Nature Physics*, 6:980983, 2010. 30, 59, 123

[118] CUOS HFS: www.engin.umich.edu/research/cuos/researchgroups/hfs/index.html, 2011. 32

[119] S.-W. Bahk, P. Rousseau, T. A. Planchon, V. Chvykov, G. Kalintchenko, A. Maksimchuk, G. A. Mourou, and V. Yanovsky. Generation and characterization of the highest laser intensities (10^{22} W/cm^2). *Opt. Lett.*, 29(24):2837–2839, Dec 2004. 32

[120] V. Chvykov, P. Rousseau, S. Reed, G. Kalinchenko, and V. Yanovsky. Generation of 10^{11} contrast 50 TW laser pulses. *Opt. Lett.*, 31(10):1456–1458, May 2006.

[121] V. Yanovsky, V. Chvykov, G. Kalinchenko, P. Rousseau, T. Planchon, et al. Ultra-high intensity- 300-TW laser at 0.1 Hz repetition rate. *Optics Express*, 16:2109–2114, 2008. 32, 102

[122] Donna Strickland and Gerard Mourou. Compression of amplified chirped optical pulses. *Optics Communications*, 56(3):219 – 221, 1985. 32

[123] Aurélie Jullien, Olivier Albert, Frédéric Burgy, Guy Hamoniaux, Jean-Philippe Rousseau, Jean-Paul Chambaret, Frédérika Augé-Rochereau, Gilles Chériaux, Jean Etchepare, Nikolay Minkovski, and Solomon M. Saltiel. 10^{-10} temporal contrast for femtosecond ultraintense lasers by cross-polarized wave generation. *Opt. Lett.*, 30(8):920–922, Apr 2005. 33

[124] P.S. Banks, M.D. Perry, V. Yanovsky, S.N. Fochs, B.C. Stuart, and J. Zweiback. Novel all-reflective stretcher for chirped-pulse amplification of ultrashort pulses. *Quantum Electronics, IEEE Journal of*, 36(3):268 –274, March 2000. 33

[125] K. A. Tanaka, T. Yabuuchi, T. Sato, R. Kodama, Y. Kitagawa, T. Takahashi, T. Ikeda, Y. Honda, and S. Okuda. Calibration of imaging plate for high energy electron spectrometer. *Review of Scientific Instruments*, 76(1):013507, 2005. 39, 45

[126] Y. Glinec, J. Faure, A. Guemnie-Tafo, V. Malka, H. Monard, J. P. Larbre, V. De Waele, J. L. Marignier, and M. Mostafavi. Absolute calibration for a

broad range single shot electron spectrometer. *Review of Scientific Instruments*, 77(10):103301, 2006. 39

[127] National Instruments Labview: http://www.ni.com/labview/, 2011. 40

[128] G. S. Settles. *Schlieren and shadowgraph techniques: Visualizing phenomena in transparent media*. Springer-Verlag, Berlin, 2001. 42

[129] T. Matsuoka, C. McGuffey, P. G. Cummings, Y. Horovitz, F. Dollar, V. Chvykov, G. Kalintchenko, P. Rousseau, V. Yanovsky, S. S. Bulanov, A. G. R. Thomas, A. Maksimchuk, and K. Krushelnick. Stimulated raman side scattering in laser wakefield acceleration. *Physical Review Letters*, 105(3):034801–+, July 2010. 44, 51

[130] A. G. R. Thomas, S. P. D. Mangles, Z. Najmudin, M. C. M. C. Kaluza, C. D. Murphy, and K. Krushelnick. Measurements of wave-breaking radiation from a laser-wakefield accelerator. *Phys. Rev. Lett.*, 98(1):054802, 2007. 44

[131] R. Fonseca, L. Silva, F. Tsung, V. Decyk, W. Lu, C. Ren, W. Mori, S. Deng, S. Lee, T. Katsouleas, and J. Adam. Osiris: A three-dimensional, fully relativistic particle in cell code for modeling plasma based accelerators. In Peter Sloot, Alfons Hoekstra, C. Tan, and Jack Dongarra, editors, *Computational Science ICCS 2002*, volume 2331 of *Lecture Notes in Computer Science*, pages 342–351. Springer Berlin / Heidelberg, 2002. 46

[132] F. S. Tsung, R. Narang, W. B. Mori, et al. Near-GeV-energy laser-wakefield acceleration of self-injected electrons in a centimeter-scale plasma channel. *Phys. Rev. Lett.*, 93:185002, 2004. 46

[133] N. Pichoff, J. M. Lagniel, and S. Nath. Simulation results with an alternate 3d space charge routine, picnic. *Proceedings of the XIX International Linac Conference*, 16:141, 1998. 47

[134] S. Semushin and V. Malka. High density gas jet nozzle design for laser target production. *Review of Scientific Instruments*, 72(7):2961–2965, 2001. 48

[135] J. J. Thomson. *Conduction of electricity through gases*. Cambridge University Press, Cambridge, 1906. 51

[136] C. Joshi, T. Tajima, J. M. Dawson, H. A. Baldis, and N. A. Ebrahim. Forward raman instability and electron acceleration. *Phys. Rev. Lett.*, 47:1285–1288, 1981. 51

[137] W. B. Mori, C. D. Decker, D.E. Hinkel, and T. Katsouleas. Raman forward scattering of short-pulse high-intensity lasers. *Phys. Rev. Lett.*, 72(10):1482, 1994.

[138] G. Shvets and X. Li. Raman forward scattering in plasma channels. *Physics of Plasmas*, 8(1):8–11, 2001. 51

[139] Eric Esarey, Sally K. Ride, and Phillip Sprangle. Nonlinear thomson scattering of intense laser pulses from beams and plasmas. *Phys. Rev. E*, 48(4):3003–3021, Oct 1993. 51

[140] K. I. Popov, W. Rozmus, V. Yu. Bychenkov, N. Naseri, C. E. Capjack, and A. V. Brantov. Ion response to relativistic electron bunches in the blowout regime of laser-plasma accelerators. *Phys. Rev. Lett.*, 105(19):195002, Nov 2010. 59

[141] Andor Technology PLC: http://www.andor.com/scientific_cameras/x-ray/. 59, 110

[142] Paul Kirkpatrick. On the theory and use of ross filters. *Review of Scientific Instruments*, 10(6):186–191, 1939. 64

[143] S. Kneip. *Laser Plasma Accelerator and Wiggler*. PhD thesis, Imperial College London, London, UK, 2010. 64

[144] S. P. D. Mangles, A. G. R. Thomas, O. Lundh, F. Lindau, M. C. Kaluza, A. Persson, C.-G. Wahlström, K. Krushelnick, and Z. Najmudin. On the stability of laser wakefield electron accelerators in the monoenergetic regime. *Physics of Plasmas*, 14(5):056702, 2007. 67

[145] F. S. Tsung, W. Lu, M. Tzoufras, et al. Simulation of monoenergetic electron generation via laser wakefield accelerators for 5-25 TW lasers. *Phys. Plasmas*, 13:056708, 2006. 67

[146] Y. Ehrlich, C. Cohen, A. Zigler, J. Krall, P. Sprangle, and E. Esarey. Guiding of high intensity laser pulses in straight and curved plasma channel experiments. *Phys. Rev. Lett.*, 77(20):4186–4189, Nov 1996. 68

[147] B. Greenberg, M. Levin, A. Pukhov, and A. Zigler. Low jitter capillary discharge channels. *Applied Physics Letters*, 83(14):2961–2963, 2003.

[148] M. Levin, A. Pukhov, R. F. Hubbard, D. Kaganovich, D. F. Gordon, P. Sprangle, A. Ting, B. Hafizi, and A. Zigler. Longitudinal profiles of plasma parameters in a laser-ignited capillary discharge and implications for laser wakefield accelerator applications. *Applied Physics Letters*, 87(26):261501, 2005.

[149] M. Levin, A. Pukhov, A. Zigler, K. Sugiyama, K. Nakajima, R. F. Hubbard, A. Ting, D. F. Gordon, P. Sprangle, and D. Kaganovich. Long plasma channels in segmented capillary discharges. *Physics of Plasmas*, 13(8):083108, 2006. 68, 71

[150] D. J. Spence, A. Butler, and S. M. Hooker. First demonstration of guiding of high-intensity laser pulses in a hydrogen-filled capillary discharge waveguide. *Journal of Physics B-Atomic Molecular and Optical Physics*, 34(21):4103–4112, 2001. 69

[151] D. J. Spence, A. Butler, and S. M. Hooker. Gas-filled capillary discharge waveguides. *J. Opt. Soc. Am. B*, 20(1):138–151, Jan 2003. 69

[152] S. Karsch, J. Osterhoff, A. Popp, et al. GeV-scale electron acceleration in a gas-filled capillary discharge waveguide. *New J. Phys.*, 9:415, 2007. 69

[153] T. P. Rowlands-Rees, C. Kamperidis, S. Kneip, A. J. Gonsalves, S. P. D. Mangles, J. G. Gallacher, E. Brunetti, T. Ibbotson, C. D. Murphy, P. S. Foster, M. J. V. Streeter, F. Budde, P. A. Norreys, D. A. Jaroszynski, K. Krushelnick, Z. Najmudin, and S. M. Hooker. Laser-driven acceleration of electrons in a partially ionized plasma channel. *Phys. Rev. Lett.*, 100(10):105005, Mar 14 2008. 69, 84, 101

[154] Takashi Kameshima, Wei Hong, Kiyohiro Sugiyama, Xianlun Wen, Yuchi Wu, Chuanming Tang, Qihua Zhu, Yuqiu Gu, Baohan Zhang, Hansheng Peng, Shin ichi Kurokawa, Liming Chen, Toshiki Tajima, Tetsuro Kumita, and Kazuhisa Nakajima. 0.56 GeV laser electron acceleration in ablative-capillary-discharge plasma channel. *Applied Physics Express*, 1(6):066001, 2008. 69, 83

[155] B. Cros, N. E. Andreev, M. V. Chegotov, P. Mora, and G. Vieux. Diagnostics for guided laser plasma wakefield. *International Journal of Modern Physics B*, 21:548–558, 2007. 69

[156] N. E. Andreev, B. Cros, G. Maynard, P. Mora, and F. Wojda. Coupling efficiency of intense laser pulses to capillary tubes for laser wakefield acceleration. *IEEE Transactions on Plasma Science*, 36:1746–1750, aug 2008. 69

[157] C. G. Durfee and H. M. Milchberg. Light pipe for high intensity laser pulses. *Phys. Rev. Lett.*, 71(15):2409–2412, Oct 1993. 69, 70

[158] K. Krushelnick, A. Ting, C. I. Moore, H. R. Burris, E. Esarey, P. Sprangle, and M. Baine. Plasma channel formation and guiding during high intensity short pulse laser plasma experiments. *Phys. Rev. Lett.*, 78(21):4047–4050, 1997.

[159] A. G. R. Thomas, C. D. Murphy, S. P. D. Mangles, A. E. Dangor, P. Foster, J. J. Gallacher, D. A. Jaroszynski, C Kamperidis, K. L. Lancaster, P. A. Norreys, R. Viskup, K. Krushelnick, and Z. Najmudin. Monoenergetic electronic beam production using dual collinear laser pulses. *Phys. Rev. Lett.*, 100(1):255002, 2008. 69

[160] C. McGuffey, M. Levin, T. Matsuoka, V. Chvykov, G. Kalintchenko, P. Rousseau, V. Yanovsky, A. Zigler, A. Maksimchuk, and K. Krushelnick. Guiding of 35 TW laser pulses in ablative capillary discharge waveguides. *Physics of Plasmas*, 16(11):113105+, 2009. 70

[161] Mingwei Liu, Hong Guo, Bingju Zhou, Liqiang Tang, Xiaojuan Liu, and Yougen Yi. Comparison of ponderomotive self-channeling and higher-order relativistic effects on intense laser beams propagating in plasma channels. *Physics Letters A*, 352(4-5):457 – 461, 2006. 73

[162] A.A. Babin, D.V. Kartashov, A.M. Kiselev, V.V. Lozhkarev, A.N. Stepanov, and A.M. Sergeev. Ionization spectrum broadening and frequency blue-shift of high-intensity femtosecond laser pulses in gas-filled capillary tubes. *Applied Physics B: Lasers and Optics*, 75:509–514, 2002. 10.1007/s00340-002-0903-y. 82

[163] C. D. Murphy, R. Trines, J. Vieira, A. J. W. Reitsma, R. Bingham, J. L. Collier, E. J. Divall, P. S. Foster, C. J. Hooker, A. J. Langley, P. A. Norreys, R. A. Fonseca, F. Fiuza, L. O. Silva, J. T. Mendonca, W. B. Mori, J. G. Gallacher, R. Viskup, D. A. Jaroszynski, S. P. D. Mangles, A. G. R. Thomas, K. Krushelnick, and Z. Najmudin. Evidence of photon acceleration by laser wake fields. *Physics of Plasmas*, 13(3), 2006. 82

[164] C. G. R. Geddes, K. Nakamura, G. R. Plateau, Cs. Toth, E. Cormier-Michel, E. Esarey, C. B. Schroeder, J. R. Cary, and W. P. Leemans. Plasma-density-gradient injection of low absolute-momentum-spread electron bunches. *Phys. Rev. Lett.*, 100(21):215004, May 2008. 84

[165] J. Osterhoff, A. Popp, Zs. Major, B. Marx, T. P. Rowlands-Rees, M. Fuchs, M. Geissler, R. Hörlein, B. Hidding, S. Becker, E. A. Peralta, U. Schramm, F. Grüner, D. Habs, F. Krausz, S. M. Hooker, and S. Karsch. Generation of stable, low-divergence electron beams by laser-wakefield acceleration in a steady-state-flow gas cell. *Phys. Rev. Lett.*, 101(8):085002, Aug 2008. 86

[166] Texas Petawatt Project: http://www.ph.utexas.edu/ utlasers/tpp.php, 2011. 100

[167] C. I. Moore, A. Ting, S.J. McNaught, J. Qiu, H. R. Burris, and P. Sprangle. A laser-accelerator injector based on laser ionization and ponderomotive acceleration of electrons. *Phys. Rev. Lett.*, 82(8):1688–1691, Feb 22 1999. 101

[168] D. Umstadter, J. K. Kim, and E. Dodd. Laser injection of ultrashort electron pulses into wakefield plasma waves. *Phys. Rev. Lett.*, 76(12):2073 – 2076, 1996. 101

[169] M. Chen, Z. M. Sheng, Y. Y. Ma, and J. Zhang. Electron injection and trapping in a laser wakefield by field ionization to high-charge states of gases. *Journal of Applied Physics*, 99(5):056109, 2006. 101

[170] E. Oz, S. Deng, T. Katsouleas, P. Muggli, C. D. Barnes, I. Blumenfeld, F. J. Decker, P. Emma, M. J. Hogan, R. Ischebeck, R. H. Iverson, N. Kirby, P. Krejcik, C. O'Connell, R. H. Siemann, D. Walz, D. Auerbach, C. E. Clayton, C. Huang, D. K. Johnson, C. Joshi, W. Lu, K. A. Marsh, W. B. Mori, and M. Zhou. Ionization-induced electron trapping in ultrarelativistic plasma wakes. *Phys. Rev. Lett.*, 98(8):084801, Feb 23 2007. 101

[171] C. McGuffey, A. G. R. Thomas, W. Schumaker, T. Matsuoka, V. Chvykov, F. J. Dollar, G. Kalintchenko, V. Yanovsky, A. Maksimchuk, K. Krushelnick,

Yu, I. V. Glazyrin, and A. V. Karpeev. Ionization Induced Trapping in a Laser Wakefield Accelerator. *Physical Review Letters*, 104(2):025004, Jan 2010. 102

[172] A. Pak, K. A. Marsh, S. F. Martins, W. Lu, W. B. Mori, and C. Joshi. Injection and Trapping of Tunnel-Ionized Electrons into Laser-Produced Wakes. *Physical Review Letters*, 104(2):025003, Jan 2010. 102

[173] ALS website: http://www-als.lbl.gov/, 2011. 123

[174] O. Lundh, J. Lim, C. Rechatin, L. Ammoura, A. Ben-Ismaïl, X. Davoine, G. Gallot, J-P. Goddet, E. Lefebvre, V. Malka, and J. Faure. Few femtosecond, few kiloampere electron bunch produced by a laserplasma accelerator. *Nature Physics*, 7:219222, 2011. 123

[175] R. M. Morrison. An economic analysis of electron accelerators and cobalt-60 for irradiating food, 1989. Retrieved February 3, 2011, from http://www.ers.usda.gov/publications/TB1762/tb1762.pdf. 124

[176] A.J. Berejka. Application of electron accelerators: Prospects and challenges, 2009. Retrieved February 3, 2011, from http://www-pub.iaea.org/MTCD/publications/PDF/P1433_CD/datasets/summaries /Sum_SM_EB.pdf. 124

[177] D. Kaganovich, A. Ting, D. F. Gordon, R. F. Hubbard, T. G. Jones, A. Zigler, and P. Sprangle. First demonstration of a staged all-optical laser wakefield acceleration. *Physics of Plasmas*, 12(10):100702–100702–4, 2005. 124

[178] B. Pollock, J. Meinecke, J. Shaw, J. Ralph, C. Clayton, K. Marsh, C. Joshi, S. Glenzer, G. Tynan, and D. Froula. Two-stage laser wakefield acceleration experiments in the bubble regime. *APS Meeting Abstracts*, page 7001, November 2010. 124

[179] D. Panasenko, A. J. Shu, C. B. Schroeder, A. J. Gonsalves, K. Nakamura, N. H. Matlis, E. Cormier-Michel, G. Plateau, C. Lin, C. Toth, C. G. R. Geddes, E. Esarey, and W. P. Leemans. Staging laser plasma accelerators for increased beam energy. *AIP Conference Proceedings*, 1086(1):215–220, 2009. 124